

University of Nottingham
UK | CHINA | MALAYSIA

# Soft X-ray core-level spectroscopy studies of molecules on $TiO_2$ surfaces in the context of light harvesting

M H Mesbah Ahmed

**Supervisor: Dr James N. O'Shea**

Thesis submitted to the University of Nottingham
for the degree of Doctor of Philosophy

**October 2022**

*Dedicated to my parents*

# *Abstract*

Studying the interaction between the dye and the surface as well as how the system reacts to light is important for understanding the electrical and chemical characteristics of dye sensitised solar cells (DSSC). In this thesis, several model systems relevant to dye sensitised solar cells have been investigated for further understanding. But, this thesis starts with the investigation on the popular semiconductor for DSSC application, rutile $TiO_2(110)$. At first, the annealing induced migration of defects in single crystals of rutile titanium dioxide have been investigated, and then the next chapter, investigates how defects interact with the molecules of oxygen, water, and air.

Firstly, this thesis present an in-situ study of defect migration in rutile $TiO_2(110)$ conducted using X-ray Photoelectron Spectroscopy (XPS). The ability of titanium dioixide to split water into $OH^-$ and $H^+$ species is heavily dependent on the behaviour of defects in the crystal structure at or near the surface. First, surface and sub-surface defects were created in the crystal by argon ion sputtering. Subsequent in-situ exposure of the defective crystal to liquid water healed the surface defects whilst the sub-surface remained defective. The sample was then annealed whilst XPS was used to monitor the concentration of titanium defects. At low annealing temperatures $Ti^{3+}$ was observed to migrate from the sub-surface to the surface. Further annealing gradually restored the surface and sub-surface to the defect-free $Ti^{4+}$ form, during which the changes in abundance of $Ti^{1+}$, $Ti^{2+}$ and $Ti^{3+}$ defects are discussed.

In the second experimental chapter, water, oxygen, air, and ambient pressure were applied to defective rutile $TiO_2(110)$ surfaces. Before each exposure, defective surfaces were created using $Ar^+$ sputtering to investigate the effect of the corresponding exposed molecules. When exposed to 0.2 mbar water, 1 mbar oxygen, 5 mbar air, ambient pressure at room temperature, 323 , 373 , 423 , 573 , and 723 K respectively, the intensity of the oxygen vacancy gradually decreased. Water exposure heals defects by water dissociation whereas during oxygen exposure oxygen dissociates into an oxygen atom and oxygen adatom, where the oxygen atom fills the vacancy and the oxygen adatom dissociates

further water and produces two identical OH groups. Further depletion of the defect was observed after exposure to ambient pressure. During annealing in ambient pressure, a rapid depletion of Ti intermediate oxidation state was observed as temperature increased. This is more likely due to the bulk assistance (through titanium interstitial and oxygen vacancy diffusion mechanisms) oxidation mechanism's progressive conversion of $Ti^{1+}$ defects to $Ti^{4+}$ via intermediate oxidation states .

In the next experimental chapter, bi-isonicotionic acid has been deposited onto rutile, anatase and mesoporous $TiO_2$. X-ray photoelectron spectroscopy (XPS) and X-ray absorption spectroscopy (XAS) have been used to obtain chemical information and map out the density of states for the system. We find that the LUMO lies entirely within the band gap of the rutile, anatase and mesoporous titania, as a consequence, the electron transfer between LUMO and substrates is electronically forbidden. But the LUMO+1 and LUMO+2 states of the core excited molecules are overlapped with the unoccupied states in the substrate. So, it is possible to transfer charge from molecules to substrate. The core-hole clock is implemented using resonant photoelectron spectroscopy (RPES) data. The charge transfer time of bi-isonicotinic acid on rutile and anatase titania is found to be comparable. While the obtained charge transfer time for bi-isonicotinic acid on mesoporous titania is longer than the rutile and anatase.

Finally, the chemisorbed and physisorbed coverage of N3 dye complex on mesoporous $TiO_2$ has been investigated. X-ray photoemission spectroscopy (XPS) spectra reveal the presence of protonated carboxylic groups, which might be evident of the absorption of N3 on mesoporous substrate bonded through a mixture of bidentate and monodentate bonding geometries. From the density of states for the system we found that the LUMO lies entirely within the band gap of the mesoporous titania, and the electron transfer between LUMO and substrate is electronically forbidden. The intense features and vibronic coupling observed in RIXS and RPES have been discussed thoroughly. The RIXS, RPES and calculated density functional theory (DFT) have been combined to provide an understanding of the electronic structure of complex molecules. The orbital contributions of the bi-isonicotinic acid and thiocyanate

ligands were used to interpret the obtained RIXS and RPES data.

# *Acknowledgements*

First and foremost, I am grateful to Dr. James N. O'shea, my PhD supervisor, for his invaluable advice, consistent support, and cheerful demeanour. During my second beamtime experiment in SOLEIL, France, he took me to the Eiffel Tower and the Palace of Versailles after learning that I had never been there before. This was a welcome diversion from the intense beamtime experiment. A special thanks must go to Robert Temperton for his support and guidance during my PhD journey including beamtime experiments, particularly for the DFT calculations. I'd like to thank my research group colleagues Jack Hart and Chris Ryder for their help and support. I would like to express my sincere gratitude to Professor Peter H Beton for his guidelines and indispensable advice, which gave me a clear direction in my PhD journey. I enjoyed every meeting with him and learned a lot from him. I also want to thank Alexei Preobrajenski, Alexander Generalov at FlexPES beamline, MAX IV lab who helped with the technical side of things. Nicolaou Alessandro provided technical assistance at the SEXTANTS beamline at SOLEIL, for which I am also grateful. Furthermore, the work presented within this thesis would not have been possible without the support of my friends and family, to whom I owe a great deal. Massive thanks and love to my wife Sabrina and daughter Aurora for all the sacrifices they made and for being supportive throughout my PhD journey. Finally, I would like to thank Bangabandhu Science and Technology Fellowship Trust for funding my PhD research.

# *List of Publications*

1. **An in situ exploration of subsurface defect migration to a liquid water-exposed rutile $TiO_2$(110) surface by XPS**. M. H. Mesbah Ahmed, Robert H. Temperton, James N. O'Shea. *Surface and Interface Analysis*. 1-7 (2020)

2. **Effect of atmospheric molecules on defective rutile $TiO_2$(110): reveal by the interaction of water, oxygen and atmospheric air with the surface defects**. M. H. Mesbah Ahmed, Jack Hart, James N. O'Shea. *(In preparation)*

3. **Adsorption and ultra fast charge transfer interactions of bi-isonicotinic acid on rutile, anatase and mesoporous $TiO_2$**. M. H. Mesbah Ahmed, Jack Hart, Robert H. Temperton, James N. O'Shea. *(In preparation)*

# Contents

**Abstract** **i**

**Acknowledgements** **iv**

**List of Publications** **v**

**1 Introduction to dye sensitised solar cell** **1**

1.1 Introduction . . . . . 1

1.2 Dye sensitised solar cells . . . . . 2

1.3 Charge transfer dynamics . . . . . 6

1.4 Bulk assisted reoxidation of defective rutile $TiO_2$ . . . . . 9

1.5 Aim of this thesis . . . . . 10

**2 Experimental Method** **12**

2.1 Sample preparation techniques . . . . . 12

2.1.1 Surface cleaning . . . . . 12

2.1.2 Molecular deposition techniques . . . . . 13

2.2 Photoemission spectroscopy . . . . . 15

2.2.1 Near ambient pressure X-ray photoelectron spectroscopy (NAP-XPS) . . . . . 15

2.2.2 Synchrotron radiation . . . . . 21

2.2.3 X-ray absorption spectroscopy . . . . . 25

2.2.4 Resonant photoelectron spectroscopy (RPES) . . . . . 26

2.2.5 Resonant inelastic X-ray scattering (RIXS) . . . . . 28

2.2.6 Surface sensitivity . . . . . 30

2.2.7 Interpreting XPS spectra . . . . . 31

2.3 Data processing . . . . . 34

2.3.1 XPS data processing . . . . . 34
2.3.2 XAS data processing . . . . . 35
2.4 Summary and Conclusions . . . . . 37

**3 Annealing induced defect migration study on water exposed defective rutile $TiO_2$(110) 38**

3.1 Introduction . . . . . 38
3.2 Method . . . . . 42
3.3 Results and Discussion . . . . . 43
3.4 Summary and Conclusions . . . . . 54

**4 Water, oxygen and ambient pressure exposure on defective rutile $TiO_2$(110) 55**

4.1 Introduction . . . . . 55
4.2 Method . . . . . 57
4.3 Results and Discussion . . . . . 58
4.3.1 $Ar^+$ ion sputtered rutile $TiO_2$(110) surfaces . . . . . 58
4.3.2 Exposure to water, oxygen and ambient pressure . . . . . 61
4.4 Summary and Conclusions . . . . . 70

**5 Ultra fast charge transfer dynamics of bi-isonicotinic acid on rutile, anatase and mesoporous $TiO_2$ 72**

5.1 Introduction . . . . . 72
5.2 Methods . . . . . 74
5.3 Results and Discussion . . . . . 75
5.3.1 Bi-isonicotinic acid / rutile $TiO_2$(110) . . . . . 75
5.3.2 Bi-isonicotinic acid / anatase $TiO_2$(101) . . . . . 86
5.3.3 Bi-isonicotinic acid / mesoporous $TiO_2$ . . . . . 93
5.4 Summary and Conclusions . . . . . 100

**6 N3 on mesoporous $TiO_2$ 101**

6.1 Introduction . . . . . 101
6.2 Methods . . . . . 102
6.3 Results and Discussion . . . . . 104

6.3.1 Density of states . . . . . 106
6.3.2 Resonant inelastic X-ray scattering (RIXS) . . . . . 107
6.3.3 Resonant photoemission (RPES) . . . . . 112
6.3.4 Calculated molecular orbitals . . . . . 115
6.4 Summary and Conclusions . . . . . 117
**7 Conclusions and future work** **118**
**Bibliography** **122**
**Appendices** **134**
**A List of Abbreviations** **134**

# Chapter 1

# Introduction to dye sensitised solar cell

## 1.1 Introduction

The traditional sources of energy such as coal, oil and natural gas have supplied the world with energy that drives society for long decades. But global energy consumption has already increased and is predicted to double by 2050 [1]. There must be a good alternative because global demand is rising and fossil fuel resources are constrained and concentrated in a few locations all over the globe. In addition to these, pollution from fossil fuel facilities significantly affects human health. Furthermore, the emissions of carbon dioxide and greenhouse gases harm our world. For years, researchers have investigated renewable energy sources including wind, biomass, and solar energy intending to replace fossil fuels. Solar energy conversion has been considered one of the most promising methods for addressing the global energy crisis driven by the depletion of fossil fuels [2–5].

Dye sensitised solar cells (DSSC) [6] and photo-electrochemical water splitting (PEC) [7], have drawn a lot of interest due to the direct conversion of solar energy into chemical energy. In principle, both of these solar energy conversion systems require a semiconductor with a bandgap that is in the visible

spectrum range, allowing light to excite an electron from the semiconductor's valence band into the unoccupied conduction band. The intrinsic electric field in the depletion region and the separation of an electron/hole pair across the bandgap allows for the possibility of the charges exiting the device and performing valuable work in a circuit before recombining. These solar energy conversion systems are mostly based on $TiO_2$. The work presented in this thesis starts by investigating defective $TiO_2$ which is in itself interesting for its photocatalytic properties and has therefore been studied in the context of water exposure and water splitting in addition to being a substrate for the charge transfer dye. In this chapter, the basic working principle of DSSC, the charge transfer dynamics between the substrate's surface, the dye molecules, the effect of annealing on defective $TiO_2$ and relevant research works will be discussed.

## 1.2 Dye sensitised solar cells

The dye sensitised solar cells (DSSC) have been recognised as a well established effective solutions for sustainable energy due to low cost and high efficiency compared to conventional semiconductor-based systems. They rely on a semiconductor with a wide band gap, mainly titanium dioxide (titania). Since the wide band gap of titania corresponds to ultra violet part of the electromagnetic radiation spectrum, it does not adsorb visible light. The solution to this problem was achieved by the deposition of a monolayer of a dye molecule onto the surface of a wide band-gap semiconductor. In order to make silver halide emulsions in photographic films sensitive to broader wavelengths of light, Vogel first discovered the phenomenon of utilising dyes to sensitise semiconductors to light in 1883 [8]. Based on this principle, the first DSSC devices were fabricated by Brian O'Regan and Michael Grätzel in 1991 [6] and the device made on this principle is also known as the Grätzel cell. The operating principle of the Grätzel cell is illustrated in Figure 1.1.

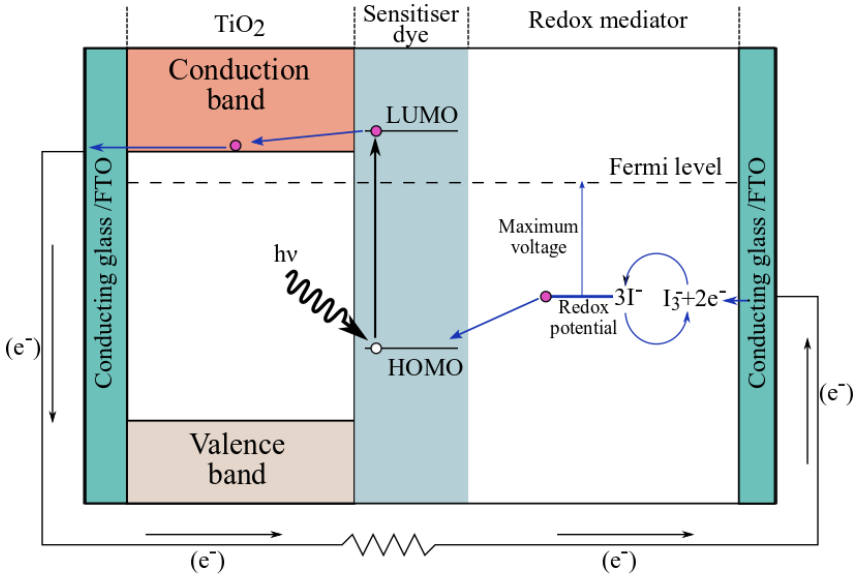



**Figure 1.1:** *Schematic illustration of the working principle of a dye sensitised solar cell (DSSC). The photoexcitation from the molecule's highest occupied molecular orbitals (HOMO) to its lowest unoccupied molecular orbitals (LUMO) of a dye molecule on the surface of titanium dioxide permits the injection of an electron into the titanium dioxide's conduction band. An electrochemical technique is used to fill the core hole, in which a redox mediator undergoes oxidation and reduction cycles, allowing electrons to be transported from the counter electrode to the dye. A voltage (limited by the energy difference between this redox process and the $TiO_2$ conduction band) is generated, allowing work to be done. The electrodes are constructed of a transparent conducting material, such as glass covered with fluorine doped tin oxide (FTO).*

As incoming photons are absorbed by the dye molecule, electrons are promoted from the molecule's highest occupied molecular orbitals (HOMO) to its lowest unoccupied molecular orbitals (LUMO) [6, 9]: i.e. taking the sensitiser dye (s) to excited dye ($S^*$). If the anode and cathode are connected in a circuit, the electron in the LUMO tunnels through the $TiO_2$ substrate and then proceeds towards the anode, producing an electric current, leaving the sensitiser in an oxide state ($S^+$). The hole in the HOMO of the dye molecule is filled via a reduction reaction with the electrolyte (generally consisting of iodide and tri-iodide) which is replaced via the cathode.

$$S^+ + e^- = S \tag{1.1}$$

The electrons required for this reduction process come from the oxidation of

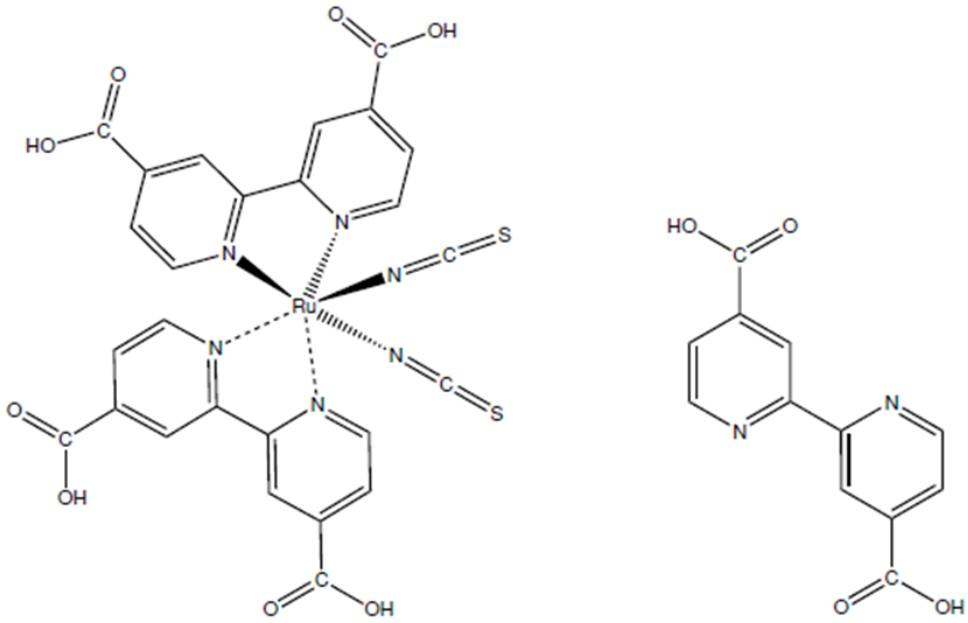



**Figure 1.2:** *The chemical structure of (a) N3 dye and (b) bi-isonicotinic acid. The N3 dye (cis-bis(isothiocyanato)bis(2,2′-bipyridyl-4,4′-dicarboxylato)-ruthenium(II)) molecule is a metalorganic complex with a ruthenium center, two thiocyanate ligands and two bi-isonicotinic acid (shown in (b)) ligands.*

the I species by the dye molecule:

$$3I^- \rightarrow I_3^- + 2e^- \tag{1.2}$$

The tri-iodide is reduced back to iodide at the counter electrode, where the aforementioned reaction is reversed to continue the cyclic process and regenerate new dye molecules:

$$I_3^- + 2e^- \rightarrow 3I^- \tag{1.3}$$

The N3 metalorganic complex (cis-bis(isothiocyanato)bis(2,2′-bipyridyl-4,4′-dicarboxylato)-ruthenium(II)), also known as Ru-535, is the most frequently used sensitiser in the Grätzel cell. This was discovered in 1993 by Nazeeruddin and co-workers [10]. The structure of N3 is illustrated in Figure 1.2(a). It has two bi-isonicotinic acid and two thiocyanate ligands around

a ruthenium centre atom. The chemical structure of bi-isonicotinic acid is also presented in Figure 1.2(b). N3 has been shown to bond to the $TiO_2$ surface via both a carboxylic acid group of the bi-isonicotinic acid ligands and the sulphur atoms that terminate the thiocyanate [11]. Where a carboxylic acid group of the bi-isonicotinic acid ligands bonded to the rutile $TiO_2$ surface by adopting a 2M-bidentate bonding geometry [12]. Whereas, for anatase $TiO_2$ surface, bonded through similar but moderately deformed surface binding ligand with two 2M-bidentate bonding geometry due to the slightly deformed surface structure compared to rutile [13–15]. The bonding geometry of N3 dye on gold, aluminium oxide has also been studied and found that only the thiocyanate bonded with the gold surface [11, 16], and in the case of aluminium oxide, only the carboxylic group is involved in the bonding [17]. To achieve highly efficient DSSC, a vast amount of research has been carried out from a range of dyes on $TiO_2$, such as bi-isonicotinic acid [13–15, 18–25, 25–30], triphenylamine [31], and WSC & CISC [32].

There are a wide variety of dyes that may be used as sensitizers in DSSCs, however the great majority of the most effective dye sensitisers that are now commercially supplied by companies like DyeSol and Solaronix are based on the N3 molecule. The 'industry standard dye' N719, which is marketed as being more soluble than N3 and able to produce higher cell voltages, is one of them. Another is the 'black dye' N795, which has a broader absorption spectrum. Purely organic dye molecules like SQ2 and RK1, which are less effective choices on the market, offer the clear advantages of being less expensive because rare earth elements are not present. The scientific community has also been attempting to balance efficiency and affordability by preserving metal-centered complexes while employing more accessible materials like copper [33] or iron [34, 35].

A significant role for photovoltaics in our future energy supply is predicted by the growing economic interest in the technology as well as environmental concerns and more pro-active environmental legislation. According to

calculations, solar cells will be able to meet all of the world's energy needs by the year 2065 [36]. To meet our energy needs, different types of solar cells are required. For example, silicon works well on rooftops and will dominate that industry. But if we are going to take advantage of the power-generating capacity of all illuminated surfaces then we also need transparent solar cells which could be perovskite or dye-sensitised windows.

## 1.3 Charge transfer dynamics

It is important to investigate the movement of photoexcited electrons between adsorbates and surfaces in order to comprehend the mechanism of charge transfer between dye molecules and surfaces in dye sensitised solar cells (DSSCs). Resonant photoemission spectroscopy (RPES) has been used in earlier research to examine the charge transfer dynamics in simplified/model systems in an effort to understand how actual devices work. Similar to the photoexcited state in DSSCs, when a photon excites an electron from the HOMO to the LUMO, resonant photoemission includes the photoexcitation of an electron from an occupied level into a LUMO state, allowing the electron to charge transfer to the surface. These investigations often compare model systems of molecule films that are both monolayer and multilayer on the corresponding surface. In the monolayer scenario, every molecule examined permits electron transport from the molecule to the surface. Multilayer films serve as a representation of the bulk molecule where the contribution of the surface is excluded due to the high surface sensitivity of electron photoemission. By analysing the subsequent decay mechanisms, these measurements rely on inferring the charge transfer behaviour that takes place when the molecule is in its core excited state. Understanding the various decay possibilities is therefore necessary in order to interpret the measurements. The possible decay mechanisms are shown in Figure 1.3 for a hypothetical molecule whose LUMO lies entirely within the bandgap of semiconductor surfaces, which does not allow charge transfer

between the LUMO and the surface's occupied valence structure but originally excited electron from LUMO+1, LUMO+2 transferred to the conduction band of the substrate. The example demonstrates the resonant excitation of an electron from a core level in the molecule—like carbon, nitrogen, etc.- that does not feature in the substrate. The interpretation would be far more challenging if we were to excite, for instance, from the valence structure/HOMOs where both the surface and the molecules contain a number of overlapping states.

The first process shown on the left of Figure 1.3, describes the resonant excitation process creating a core hole and a photoexcited electron in a LUMO state. Following the arrows to the right top and right middle show the decay options from the various states and the various charge transfer options available to this photoexcited system are highlighted to the right bottom. The molecule may relax immediately via either the participator or spectator processes, as demonstrated, without any charge transfer taking place. In the case of the participator channel, the photoexcited electron participates in an Auger like decay process. While in the spectator decay, photoexcited electrons remain at the unoccupied level for the duration of the core-hole lifespan while electrons from other orbitals go through the decay process. Notably, in all these Auger-like systems, the function of the electrons may be reversed without affecting the observable electron state. Both the photo-excited electron emitting or transitioning down to fill the core hole are legitimate outcomes for the participator decay scenario. The other potential decay pathways include charge transfer from the molecule to the surface, which leads to classic Auger decay when the photoexcited electron tunnel through the surface. The goal is to be able to distinguish the outcomes of the decay mechanisms using resonant photoemission. It is feasible to compare the strength/intensity of the participator decay channel with the normal Auger decay channel (coming from charge transfer), for instance, adopting a basic system where charge transfer only occurs in the molecule to surface direction. The so-called "core-hole clock" approach [40] may be used to determine charge transfer times by using this ratio, the known

core hole lifetimes, and the ability to compare monolayer and multilayer films [37]. The core-hole clock approach has been implemented to study charge transfer dynamics on C60 [38, 39], bi-isonicotinic acid [15, 20, 21, 23, 28], as well as N3 [11, 17, 38].

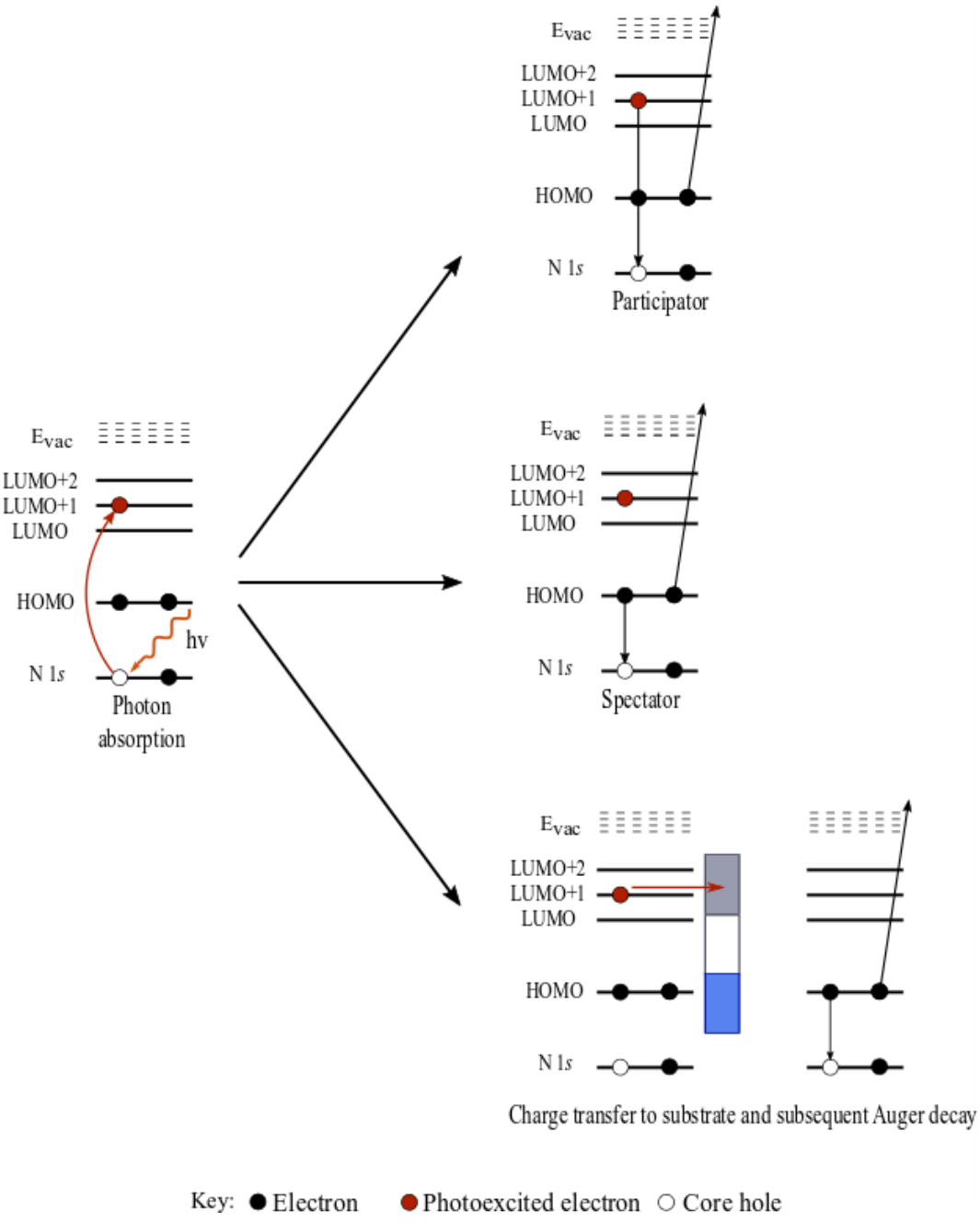



**Figure 1.3:** *Schematics of proposed decay and charge transfer mechanisms after excitation of an core electron. Through participant or spectator processes, the excited state might decay without transferring any charges. The molecule can relax via Auger decay if the photoexcited electron charge transfers into the surface.*

## 1.4 Bulk assisted reoxidation of defective rutile $TiO_2$

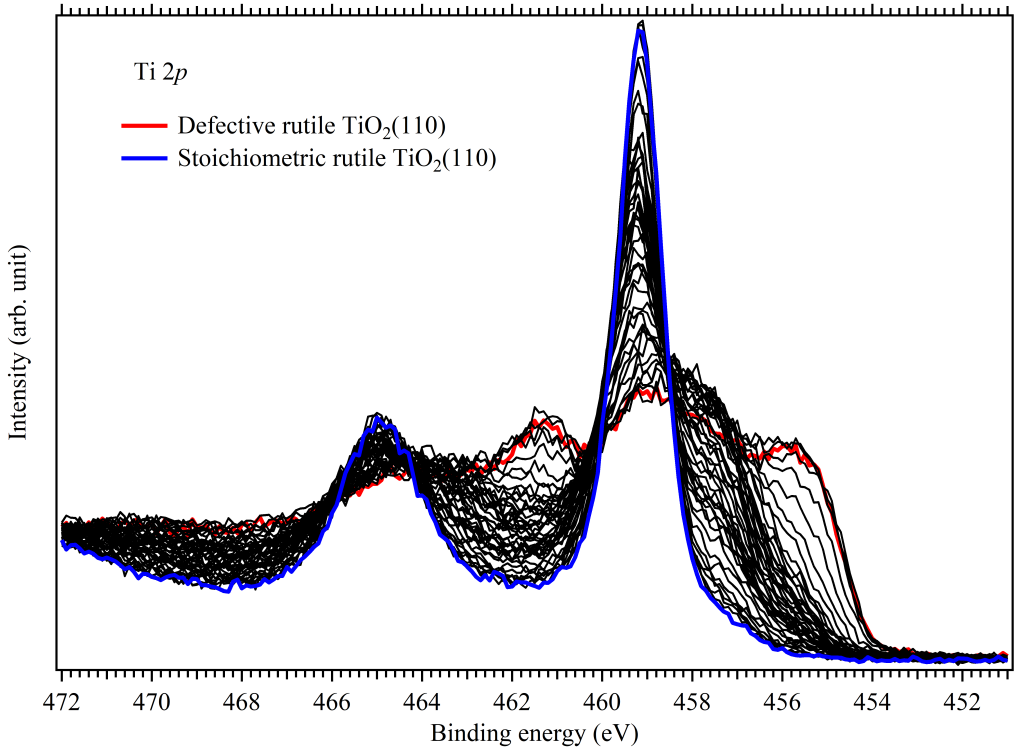



**Figure 1.4:** *Ti 2p XPS spectra present change of defective state until restoring stoichiometry of reduced rutile $TiO_2$(110) by annealing, measured at normal emission (NE). Red and blue spectra represents defective and stoichometric states of rutile $TiO_2$, respectively.*

It is important to prepare and measure samples without even the least amount of contamination. Ion sputtering is one of the most popular surface cleaning techniques used by surface scientists. The ion sputtering preferentially removes oxygen from the surface and subsurface and damages the crystallinity of the sample. Fortunately, the surfaces of rutile $TiO_2$ are forgiving and the overall stoichiometry of reduced rutile $TiO_2$ can be restored by annealing in a vacuum. Oxygen diffusion via defect migration is well known for reduced $TiO_2$ and has relatively high defect mobility. Oxygen vacancies created at the surface by ion bombardment migrate to the subsurface via a site exchange mechanism and $Ti^{3+}$, $Ti^{4+}$ interstitials diffuse through the crystal along the crystallographic c-axis[40, 41]. According to the bulk assisted oxidation mech-

anism, the vacuum reduced rutile $TiO_2(110)$ surface by ion sputter can be expressed as $Ti_aO_b$, where $a$ is greater than $b/2$ but probably less than $b$. On annealing, reduced surface restores overall stoichiometry by bulk assisted oxidation. This process has two possible mechanisms, which are the oxygen vacancies diffusion mechanism and $Ti^{3+}$ interstitial diffusion mechanism. In the oxygen vacancies diffusion mechanism, bulk supplies $O^{2-}$ anion to the reduced surface to achieve $b$ value equal to the value of $2a$ and in return receives oxygen vacancies. On the other hand, in $Ti^{3+}$ interstitial diffusion mechanism, bulk receives $Ti^{3+}$ to restore surface stoichiometry by decreasing $a$ to a value of $b/2$. Both of these models suggest that surface stoichiometry is restored by the bulk assisted oxidation[42]. Figure 1.4 shows the change of defective state until restoring the overall stoichiometry of reduced rutile $TiO_2$ by annealing. The most considerable mechanism to restore stoichiometry is bulk assisted oxidation.

## 1.5 Aim of this thesis

This thesis is intended to provide insights into the nature of defects of the single crystal rutile titanium dioxide and examine the bonding and charge transfer dynamics of complicated molecular systems that are important for light harvesting by using X-ray spectroscopies. In chapter three, annealing-induced defect migration on water exposed defective rutile $TiO_2(110)$ has been investigated. Water is exposed to highly defective single crystal rutile titanium oxide to create a highly defective subsurface coexisting with a defect-free surface. Which gives a platform to study defect migration from subsurface to surface during annealing by XPS. This has been published in the journal Surface and Interface Analysis [43]. Then in chapter four, the change of defect concentration of highly defective rutile titanium dioxide due to exposure to ambient pressure at five different temperature is discussed and compared with in-situ 0.2 mbar water, 1 mbar oxygen and 5 mbar air respectively. To invest-

igate the effect of each exposure, a similar defective state of rutile titanium dioxide is created by $Ar^+$ ion sputtering. The adsorption and charge transfer time (by using core-hole clock implementation) of bi-isonicotinic acid on rutile, anatase and mesoporous titanium oxide surface is investigated using XPS and resonant photoemission and presented in chapter five. Finally, the aim of chapter six is a thorough soft-X-ray synchrotron study examining the monolayer and multilayer coverage of the N3 dye complex on mesoporous $TiO_2$. The observed intense features and vibronic coupling mechanism in resonant inelastic X-ray scattering and resonant photoemission data are also discussed thoroughly with the help of DFT calculation.

# Chapter 2

# Experimental Method

## 2.1 Sample preparation techniques

It is important that sample preparation and experiments should be conducted in an ultra-high vacuum (UHV) environment to maintain the surface's cleanliness effectively, allowing us to measure only the desired properties without being sidetracked by contaminants and removing extraneous particles from the system after deposition. The experiments described here involve cleaning and depositing molecules onto a single crystal's surface in-situ in UHV before measurement. A brief description of how this was accomplished is given below.

### 2.1.1 Surface cleaning

Surface cleaning in ultra high vacuum (UHV) is typically accomplished using a combination of sputtering and annealing. All the samples used in the experiments reported here were cleaned using simple argon sputtering, in which argon gas was ionised and propelled towards the surface at energies ranging from 0.5 keV to 2 keV using commercially available sputter guns. This high-energy bombardment lifts fragments away from the surface while inflicting significant damage. The surface is restored by annealing at temperatures above 500 °C. During the experiments at the FlexPES beamline, MAX IV, surface crystallinity was frequently examined using low energy electron diffraction (LEED) to

ensure that the annealing was adequate to re-form the surface after sputtering. To ensure the surface is suitably clean, many rounds of sputtering and annealing are generally necessary; this may be tested using X-ray photoelectron spectroscopy to verify no unexpected impurities are present.

### 2.1.2 Molecular deposition techniques

In this thesis, we have deposited molecules on the surface in both in-situ and ex-situ techniques. Most of the depositions were carried out in-situ using gas dosing and sublimation techniques but the monolayer deposition of molecules on a mesoporous surface was prepared ex-situ using the solution deposition method. These preparation methods are discussed briefly in this section.

#### Gas dosing

The easiest technique to introduce a species onto a surface is to expose it to the molecule's partial pressure by leaking gas phase molecules into the vacuum chamber. A UHV leak valve, in its most basic form, is used to let a regulated amount of gas into the chamber. This has the benefit of making it easier to estimate the dosage (which is typically thought to be a function of the partial pressure and the exposure period), however, caution must be taken because pressure gauges vary in their sensitivity to various gases. In addition to normal room temperature/pressure gases (such as oxygen), high vapour pressure liquids (such as water) can be supplied in this manner. The formation of a liquid water layer on the titanium dioxide surface is demonstrated in chapter 3 by using this method, whereas controlled dosing of water vapour, oxygen and air is also demonstrated in chapter 4.

#### Molecular beam

Knudsen cell (generally known as K-cell) sublimation is one of the most commonly used techniques for molecular deposition. Basically, an evaporant is

contained in the crucible heated by current operated filament heater. A thermocouple is attached to the K-cell to measure the temperature of the material. The evaporator containing evaporant (generally a powder) was properly degassed. In UHV, molecules from K-cell can be deposited on the sample surface in direct line of sight by heating at the sublimation temperature of molecules. The evaporated source has long mean free path to travel along a straight line and stick on the substrate surface. This technique can produce a uniform layer over the wide surface of the substrate. The amount of molecules deposited on the substrate depends on the deposition time and temperature of the K-cell. The monolayers of bi-isonicotinic acid on rutile and anatase titanium dioxide and multilayer were prepared by Knudsen-cell thermal evaporation method (discussed in chapter 5).

**Soaking in solution**

In this method, samples are immersed in a saturated solution of the molecules in a suitable solvent until the necessary monolayer of molecules is obtained. The samples are then washed in a solvent before being left to soak for several hours in the solvent. This procedure is often repeated until the solution is clear. It is also critical to ensure that the solvent used to dissolve the molecule does not stay on the sample. If the solvent remains, it can disrupt the formation of a monolayer and contaminate the sample. When any dye does not dissolve very well in the solvent, then the method is much more involved than this. For example, bi-isonicotinic acid powder is only sparingly soluble in isopropanol. For the monolayer of bi-isonicotinic acid on mesoporous $TiO_2$ preparation, the sample was left in a small beaker of iso-propanol in a large beaker of iso-propanol together with another small beaker containing a small amount of bi-isonicotinic acid powder. Over the course of a week, the bi-isonicotinic acid adsorbs onto the mesoporous $TiO_2$. The bi-isonicotinic acid beaker is then removed and the iso-propanol is replaced in the large beaker with clean iso-propanol, and then a fresh mesoporous $TiO_2$ sample is added to scavenge any

excess bi-isonicotinic acid. This process is repeated several times to ensure that all physisorbed bi-isonicotinic acid is removed from the sample.

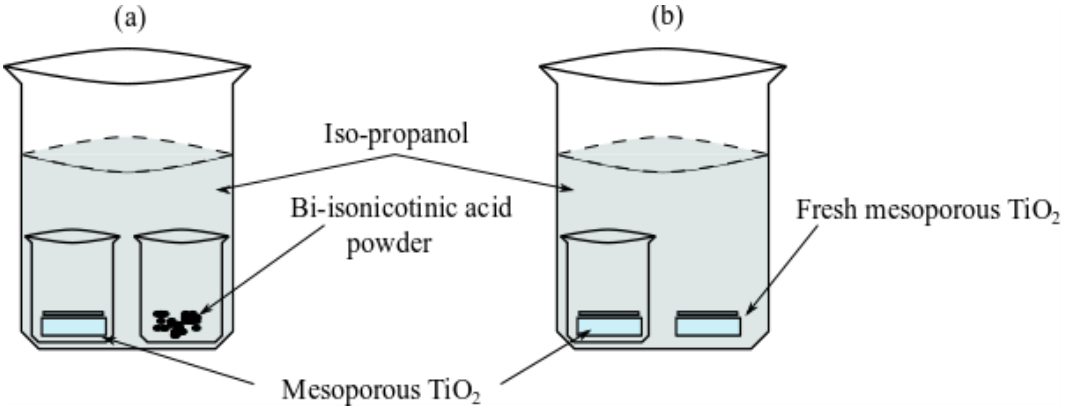



**Figure 2.1:** *Schematic diagram presenting ex-situ preparation of the monolayer of bi-isonicotinic acid on mesoporous $TiO_2$ preparation.*

## 2.2 Photoemission spectroscopy

### 2.2.1 Near ambient pressure X-ray photoelectron spectroscopy (NAP-XPS)

A SPECS Devi-sim near ambient pressure X-ray photoemission spectroscopy (NAP-XPS) system equipped with UHV preparation chamber, NAP cell, Phoibos 150 NAP hemispherical analyser and monochromatic Al k$\alpha$ X-rays (h$\nu$ = 1486.6 eV) was used to conduct this experiment. The base pressure recorded during the experiments in the analysis chamber was in the low $10^{-10}$ mbar range. It is possible to prepare the sample in the preparation chamber and transfer it to the NAP-cell without breaking the vacuum. During NAP-XPS measurements, NAP-cell was docked to the entrance cone of the analyzer. It is also facilitated with sample preparation systems such as electron beam heating, argon sputtering, Knudsen cell evaporator deposition, dose gasses, and electrospray deposition.

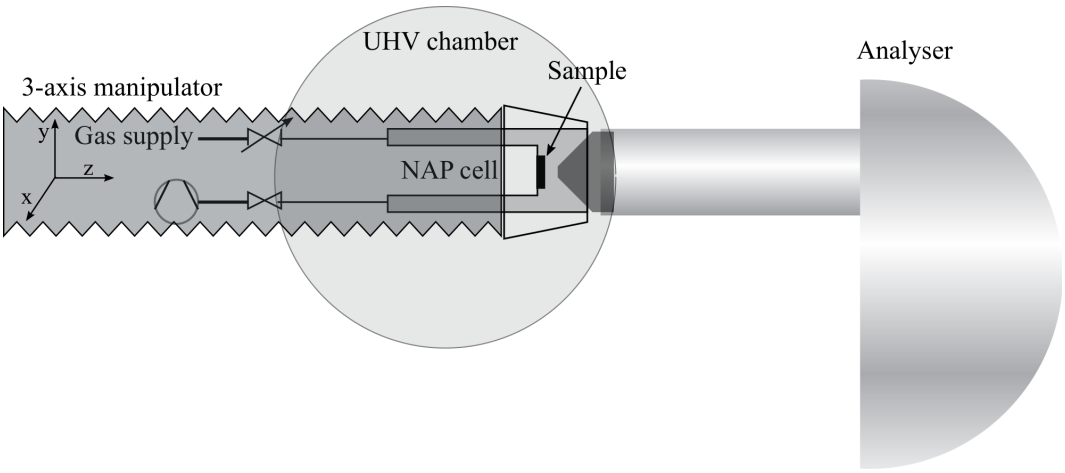



**Figure 2.2:** *Schematic diagram of near ambient pressure X-ray photoemission spectroscopy (NAP-XPS) system equipped with UHV preparation chamber, NAP cell, Phoibos 150 NAP hemispherical analyzer, and monochromatic Al kα X-rays.*

### X-ray photoelectron spectroscopy (XPS)

XPS is one of the most used methods for analyzing surface chemistry. XPS is widely used for identifying chemical composition, depth profiling on surfaces, the study of surface contamination, organic overlayers, Catalysis, and corrosion. XPS also gives insights into valence band and electronic structure. The working principle of XPS is based on Einstein's explanation of the photoelectric effect [44], illustrated in Figure 2.3. By using this theory, the kinetic energy of the emitted electron can be estimated as follows:

$$E_K = h\nu - \phi - E_B \tag{2.1}$$

where, $E_K$ = kinetic energy, $\phi$ = work function and $E_B$ = binding energy.

In XPS, the incidence of monochromatic X-ray on the solid surface excites photoelectrons from both core and valence levels of the surface atoms to the vacuum level. The photon energy h$\nu$ is available to excite the core electron and part of the photon energy is used to overcome the potential barrier and attraction of the electron for the nucleus, ($E_B$+ $\phi$). The remaining energy is the kinetic energy of the photoemission electron. This kinetic energy contrasts systematically from element to element.

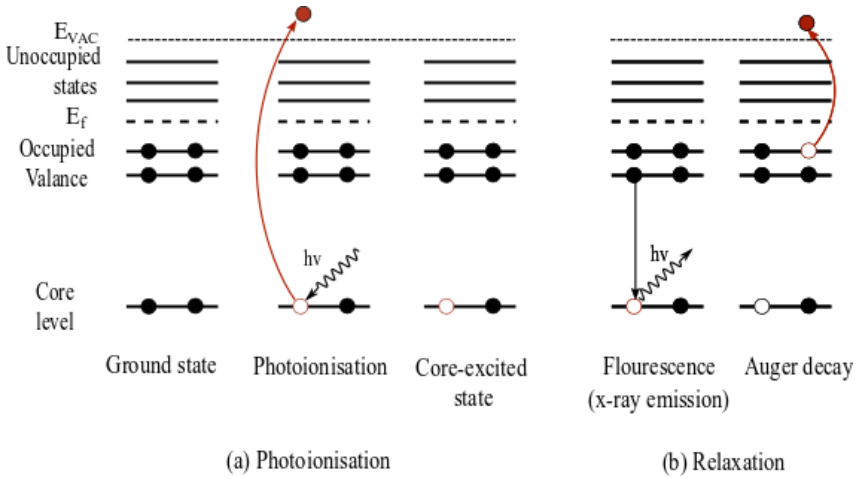



**Figure 2.3:** *Schematic illustration of the working principle of XPS. XPS mechanism consists of energy level diagram showing the initial ground state of an atom, the photoionization process where a core level electron is liberated to the vacuum, and the final core-excited state where a core-hole remains. This final state is unstable and will relax back to the ground state by the two main decay mechanisms - fluorescence/photon emission and Auger decay.*

### Monochromatic X-ray source

A high-intensity XR 50M twin anode (Al/Al) X-ray source was used as the X-ray source. Generally, the current in the wire heats up the filament. Electrons produced from heated Thoria-coated tungsten filaments (thermionic emission) hit the selected active anode face at the correct spot and generate X-ray in two ways: the Bremsstrahlung process and characteristic X-ray production. As shown in Figure 2.4, The aluminium anode Specs X-ray source is used in combination with $\mu$-FOCUS 500 monochromator. This high-performance monochromator is equipped with a Rowland circle diameter of 500 mm. The X-rays generated at the anode pass through the monochromator and hit the sample in the analysis chamber. The achievable spot size varies between 250 $\mu$m and larger than 1 mm. Turbulent water flow which is situated in the anode internal structure prevents the aluminium surface from evaporation. More than 99% of the kinetic energy of the incident electron beam is converted into heat at the anode. This heat energy converts the anode from solid to gas resulting in failure of proper operation by the X-ray source. Besides, the X-ray tube starts to short circuit or arc which causes more gas between the anode and

cathode electron source and due to the degradation of the internal vacuum x-ray tube become non-functional.

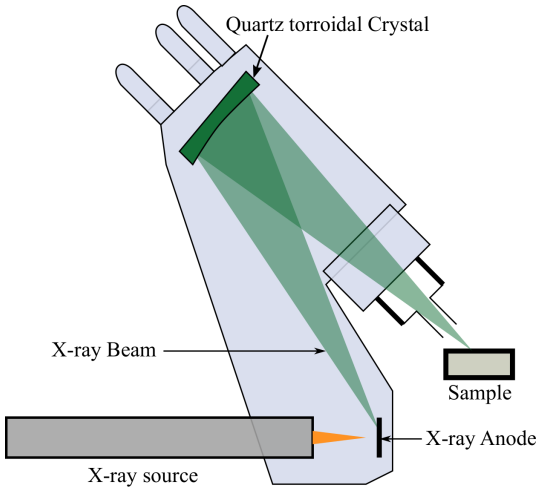



**Figure 2.4:** *Schematic diagram of the aluminium anode specs X-ray source in combination with μ-FOCUS 500 monochromator.*

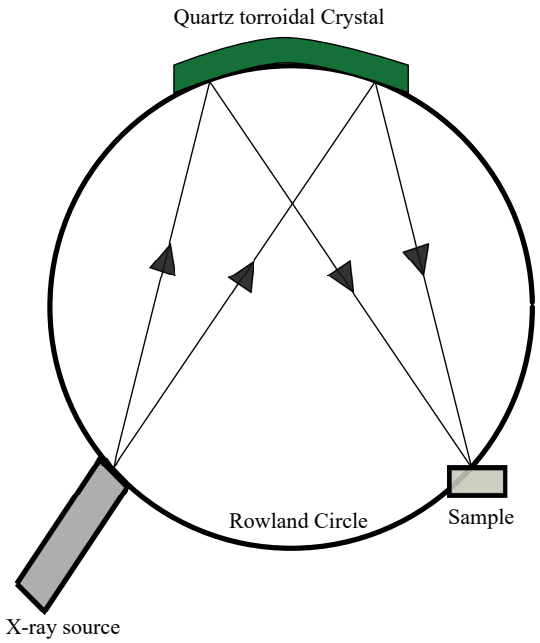



**Figure 2.5:** *Schematic diagram of the Rowland circle set up.*

The Bremsstrahlung process and characteristic X-ray production processes are illustrated in Figure 2.6. When accelerated electrons ejected from filaments hit the target, they excite electrons from the lower to higher energy band. After that relaxation occurs through the emission of the characteristic X-ray of energy equivalent to the energy gap. Whereas Bremsstrahlung X-ray emits when projectile electron decelerates by the electrostatic interactions with

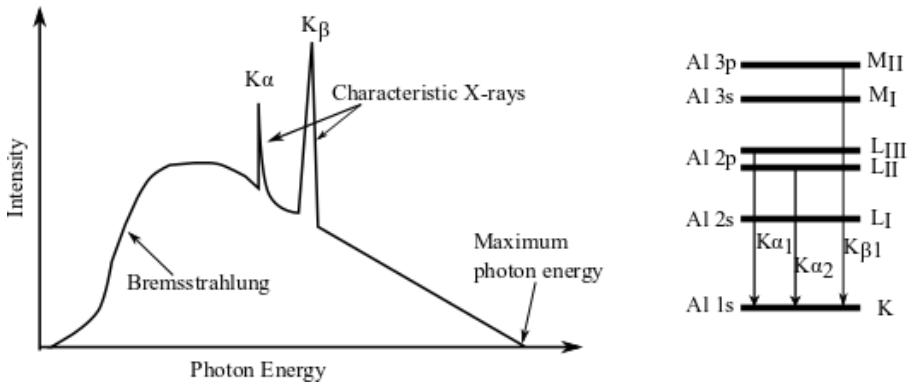



**Figure 2.6:** *Diagram represents characteristic X-ray emission and Bremsstrahlung background for Aluminium.*

electrons in the target. This change in the momentum of the electron causes X-ray photons to be emitted.

### NAP-cell

DeviSim NAP-cell is a reactor cell with a built-in manipulator, which can be easily docked into the UHV analysis chamber with PHOIBOS 150 NAP analyzer. It is designed with an easy sample transfer mechanism between the analysis chamber manipulator and the NAP-cell manipulator. The cell is also equipped with a wide range of gas inlet systems. The sample heating mechanism allows for heating up to 6 00° C at 20 mbar of $N_2$ pressure and cooling with liquid Nitrogen down to at least 200 K and a gas handling system. It allows near ambient pressure XPS measurements at pressures 30 mbar for $N_2$.

### Analyzer

As shown in Figure 2.7, the photoelectron energy distribution is mostly measured using an electrostatic energy analyzer entail of two electrically remote concentric hemispheres by a potential difference between them, so that the course of the inbound electrons is bent into a curve. The electrostatic forces allow only the electrons of preferred kinetic energy (also known as pass energy, $E_P$) through to the detector. Photoelectrons of a chosen energy are focused by

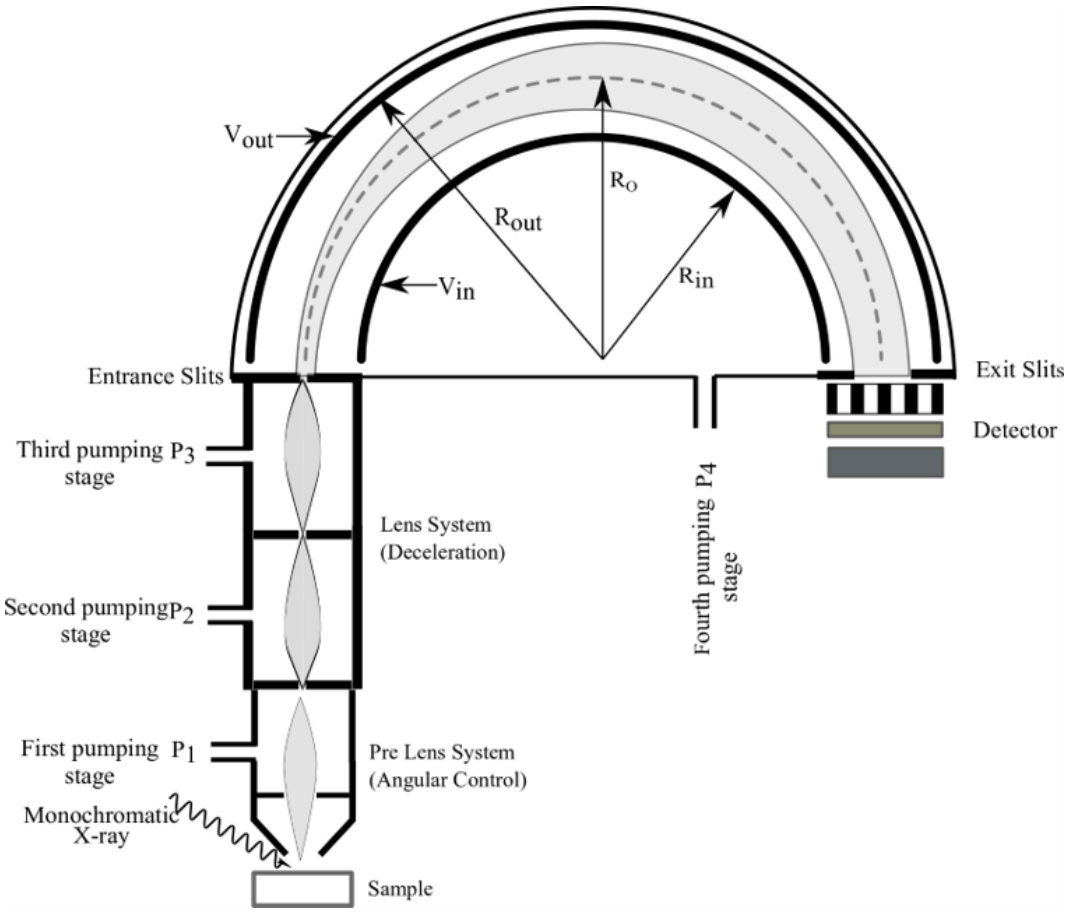



**Figure 2.7:** *Schematic diagram of PHOIBOS 150 NAP analyzer.*

the lens at the slit of the spectrometer and the lens also controls the sampling area. Electrons of kinetic energy other than preferred pass energy will crash onto the outer and inner hemispheres and be neutralized.

The applied potential difference between the two hemispheres to bend the electron trajectory is $\Delta$V. At a given $\Delta$V, only the electrons with pass energy can reach the exit slit along the median trajectory of radius $R_o$, shown in figure presented by dashed line where, $R_o=\frac{1}{2}(R_{in}+R_{out})$ [45, 46]. $R_{in}$ and $R_{out}$ are the radius of the inner and outer hemisphere respectively. High pass energy provides better energy resolution for the analyzer whereas lower pass energy gives better resolving power. The pass energy is typically chosen in the range between 5 eV and 200 eV, depending on the materials. Along with the pass energy, the size of the spectrometer and the sum of the entrance and exit slits, $S= S_{entrance}+S_{exit}$ also have a great contribution to the energy resolution of the analyzer. Slimmer slits and larger spectrometers provide a

better resolution. The smallest FWHM, ΔE can be obtained by the following equation.

$$\frac{\Delta E}{E_P} = \frac{S}{2R_o} \tag{2.2}$$

In this study, two different types of detector were used. A combination of microchannel plate (MCP), phosphorous screen along with charged coupled device (CCD) camera was used in the synchrotron facility. MCP produces a cloud of several thousand electrons from one incident electron caused by the cascade process and emerges from the rear of the plate and hits the phosphorus screen which creates flashes of light. These flashes are then detected by the CCD sensor. MCP is a massively used detector because of its high gain, high spatial resolution, and high temporal resolution output. It can produce a pulse of $10^8$ or more electrons from one incident electron. But it is not very advantageous for gaining timing information or rapid readouts due to the slow electronic readout of the optical image with its microsecond time resolution. The Phoibos 150 NAP hemispherical analyser at home in Nottingham is equipped with 2D-DLD detector. The 2D-DLD detector is a high-performance detector system for time-resolved measurements and traditional hemispherical energy analyzers. It has a very low dark count rate and strong linearity. An MCP chevron stack for electron multiplication is used in the detection method, which is then followed by a two-dimensional delayline detection array. The detector is synchronised with an external signal, such as one from a pulsed light source, using a time-to-digital converter. This 2D detector consequently offers an actual count rate in cps.

### 2.2.2 Synchrotron radiation

When electrons or other charged particles moving at relativistic speeds are forced by a magnetic field to move in a curved path, then they emit electromagnetic radiations also known as synchrotron radiation along the direction of

their motion due to the change of momentum to comply with the conservation law. Synchrotron radiation has become one of the more powerful tools for studying electronic configurations and the properties of energy surface materials. Today synchrotron radiation can prove a very intense and wide spectral range from infrared to hard X-rays to users. Up till now three generations of synchrotron radiation sources have been developed with increasing quality. At present, the fourth generation, based on free-electron lasers, already produces high power and ultrafast pulses of highly coherent radiation.

Synchrotron radiation was first discovered in 1947 [47]. The first generation synchrotron radiation, rather than dedicated to synchrotron radiation studies, was used for high energy physics experiments during the 1960s and early 1970s. But in the mid-70s, the synchrotron radiations were mainly produced by bending magnets and solely dedicated to the synchrotron light, which is called second-generation synchrotron radiation. The magnetic field devices called wigglers also became part of the second generation synchrotron source. After that, the use of wigglers and undulators in the straight section of the storage ring made it possible to produce a very intense and wide spectral range of synchrotron radiation known as third-generation synchrotron radiation.

Basically, electron synchrotrons are consist of an electron source, linear accelerator, or 'LINAC', a booster ring, and a storage ring. At first, electrons are accelerated to several millions of electron volts (MeV) energy by a linear accelerator and then a booster ring increases the energy by almost up to billions or Giga electrons volts (GeV). Finally, accelerated electrons are injected into a storage ring where they circulate in a closed loop. The storage ring consists of straight sections and corners instead of a circular ring. At the corner bending magnet (dipole magnet) forces to constrain the motion of electrons into a circular path. They lose energy during each turn and part of their energy emitting as synchrotron radiation. The two types of insertion devices used in the '3rd generation' light sources are wigglers and undulators. Both of these devices force the path of electrons to oscillate and create a sinusoidal

magnetic field with the help of a periodic array of dipole magnets, presented in Figure 2.8. Wigglers are designed in such a way that it can create larger electron oscillations than undulators. This, however, does have a dramatic effect on the radiation produced. Most of the radiated energy is produced at the turning points when the momentum of electrons changes. Wigglers and bending magnets produce radiation of similar properties but wigglers produce high-intensity radiations than bending magnets. Wigglers rely on the light output at these two extremes being physically separated so interference effects are limited. The output intensity is given by the sum of the intensities of all the "emission cones" so scales with 2N (where N is the number of periods in the wiggler). In undulators, unlike wigglers, electrons undergo much smaller amplitude oscillations meaning the light output from each oscillation overlaps. The resulting interference produces narrow regularly separated bands of intense radiation. This is shown in Figure 2.8(c).

There are three parameters to operate undulators. Firstly, the 'gap', which describes the separation between the magnetic arrays, controls the field strength which determines the position and separation between the harmonic bands. Smaller gaps also produce more intense harmonics. Secondly, some undulators allow a taper of the magnetic arrays to be set. This allows the flux to be more uniform for a given energy range. Finally, a lateral offset between magnetic arrays allows control over the polarisation (often 4 arrays are used for this). When the magnets are perfectly aligned, the polarisation is linear as the electrons oscillate back and forth on a 2D plane. By applying an offset between magnetic arrays, the electrons can be made to undergo a three-dimensional helical path. Not only does this affect the polarisation but it also causes higher harmonics to be dominant. This study does not make use of these 'helical' undulators - only linearly polarized light is considered [48, 49]. After emitting radiation, electrons passe through the radio frequency (RF) cavities, which provides enough electric field to fully restore the lost energy. This electron is called a synchronous electron.

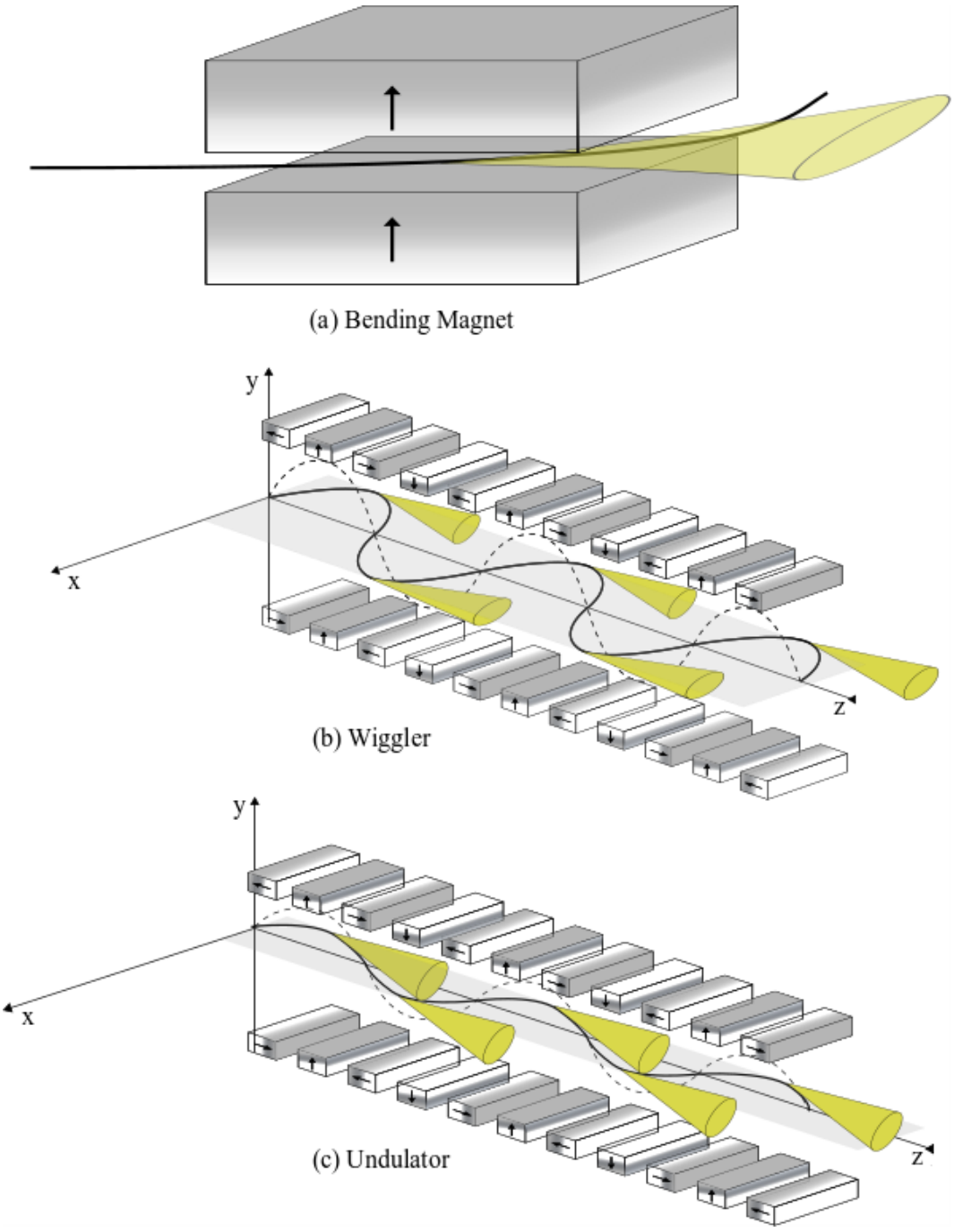



**Figure 2.8:** *Schematic illustration describes the working principle of (a) bending magnets (b) wiggler and (c) undulator. Where the dashed line represents the magnetic field on (y, z) plane, and the solid line presents the motion of electrons on (x, z) plane. Yellow cone denotes the photon emission.*

**SEXTANTS beamline at SOLEIL synchrotron facility**

The SEXTANTS beamline covers the photon energy range from 50 eV to 1700 eV with high energy resolution, with an estimated sample at $1\times10^{14}$ photons per second, providing a beam spot size of $80\,\mu\text{m}\times2\,\mu\text{m}$. The branch line is equipped with a high-efficiency $1024\times1024$ $13\,\mu\text{m}$ pixel back-illuminated CCD detector held in a fixed position. The energy range is selected by adjusting the grating angle using an encoded sine-bar drive, resulting in precise and straightforward energy calibrations.

**FlexPES beamline at MAX IV synchrotron facility**

Surface and Material Science (SMS) endstation on the FlexPES beamline at the MAX IV synchrotron radiation facility in Sweden was used for the measurements. FlexPES, located on the 1 GeV storage ring, equipped with a planar undulator and collimated plane-grating monochromator to emit photons ranging in energy from 40 to 1500 eV, which may be focused to a $65\times10\,\mu\text{m}$ spot at the SMS branch sample point or defocused to produce a larger size of $1.0\times0.4\,\text{mm}^2$. The experimental station is outfitted with a Scienta SES-2002 hemispherical analyzer for photoelectron spectroscopy (PES) and a home-built partial electron yield (PEY) microchannel plate (MCP) detector for X-ray absorption studies.

### 2.2.3 X-ray absorption spectroscopy

X-ray Absorption Spectroscopy (XAS) is a strong and well-established method for determining the distribution of unoccupied states in the energy and space domains based on element and symmetry. In order for molecular electrical devices to function, the alignment of unoccupied energy levels, such as the LUMO states, is essential. X-ray absorption spectroscopy (XAS) enables us to investigate these levels. A core electron may be promoted into various unoccupied states as a result of X-ray photon absorption; the probability of

this promotion is greatly dependent on photon energy and experimental geometry. When an outgoing electron's kinetic energy is low (approximately less than 50 eV), it experiences repeated scattering from atoms around the atom-absorber, resulting in noticeable absorption resonances both below and slightly over the absorption threshold. This low-energy section of the XAS spectrum is known as the Near-Edge X-ray Absorption Fine Structure (NEXAFS) spectrum in the area of soft X-ray spectroscopy.

This spectroscopic method operates as shown in Figure 2.9 by sweeping through photon energies over an absorption edge of a sample. Photons with energies that correspond to the energy difference between the occupied and unoccupied levels can be absorbed, promoting an electron into the unoccupied level. The resulting core-excited state decays via Auger or fluorescence emission back to the ground state. Therefore, we may map out the density of unoccupied states that are reachable by X-ray absorption by counting these electrons or photons as a function of photon energy (as determined by dipole selection rules).

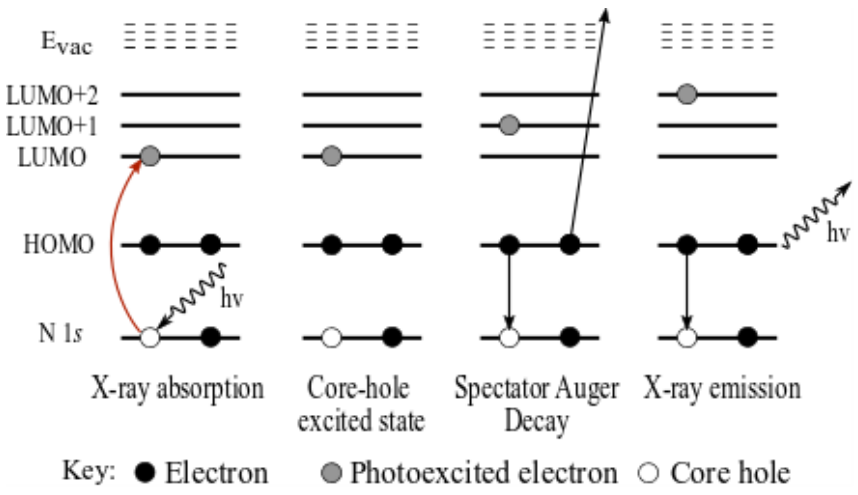



**Figure 2.9:** *Schematic illustration of the working principle of X-ray absorption spectroscopy.*

### 2.2.4 Resonant photoelectron spectroscopy (RPES)

Resonant photoelectron spectroscopy (RPES) plays an important role in determining charge delocalisation and charge transfer processes in organic photo-

voltaics and DSSCs. RPES is similar to the XPS measurements with XAS in that an electron is excited from the core-hole to the system's unoccupied bound states, and the kinetic energy of the photoelectrons, and hence the binding energy, is calculated during a subsequent Auger decay at different photon energies. The decay mechanism of an adsorbate-surface interface can be examined in this way. The RPES data is usually presented as the two dimensional plots, in which the intensity of emitted valance photoelectrons is plotted as a function of incident photon energy and their measured binding energy.

Figure 2.10 shows an example of an RPES map measured for a bi-isonicotinic acid monolayer on rutile $TiO_2$, which has a number of significant features indicating electron transfer between the surface and the molecule. In this example, XPS of the valence band region (a constant binding energy window) is measured as a function of photon energy over the C1s absorption edge. The horizontal dashed lines show intensity associated with excitation into the lowest unoccupied molecular orbital (LUMO) states, which appear at constant excitation energy. Constant kinetic energy features, denoted by diagonal dashed lines in the monolayer RPES spectrum, disperse linearly along the RPES binding energy window as photon energy increases. The spectator and Auger decay channels are corresponds to these diagonal lines. The HOMO states are enhanced when we are on the LUMO resonance (marked with vertical dotted lines). This is due to the participator decay channel, in which the electron that was excited into the LUMO state descends back down to fill the core hole; the energy it loses in this process is transferred to an electron in a HOMO state, causing it to be released into the vacuum. It is worth noting that the ultimate state following participator decay is identical to that of ordinary HOMO photoemission. In terms of measured binding energy, the two processes are thus indistinguishable, but their presence is inferred from the intensity augmentation of the HOMO when measured at the LUMO's excitation energy.

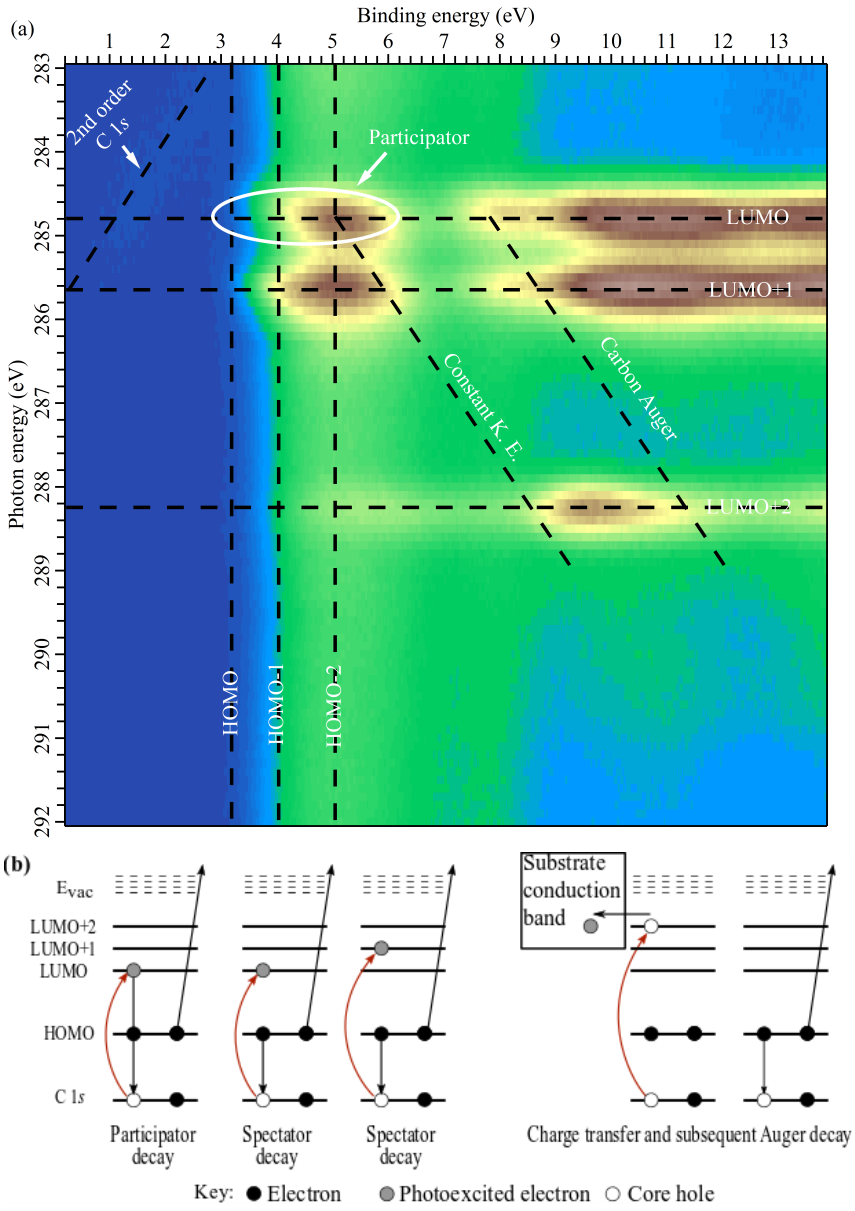



**Figure 2.10:** *(a) RPES map, measured on the Flexpes beamline at Max IV Laboratory, of a monolayer of bi-isonicotinic acid on rutile $TiO_2$. This is an example system demonstrating the charge transfer of electrons between the surface and the molecules. Key features are annotated. Photoemission HOMO features measured at the LUMO resonance are are enhanced due to participator decay channels (circled). Dashed lines show constant kinetic energy features. (b) Schematic illustration of the working principle of resonant photoemission spectroscopy (RPES).*

### 2.2.5 Resonant inelastic X-ray scattering (RIXS)

The core-hole decay as an emission of photons instead of an emission of an Auger electron is also possible through a photon-in-photon-out process. This emitted photon will be a scattered photon and it is in principle possible to determine the momentum, energy, and polarization of this photon. This syn-

chrotron based technique is called resonant inelastic X-ray scattering (RIXS). The momentum, energy, and polarisation of the incident photon can be chosen in the experimental setup to resonant with one of the system's atomic X-ray transitions. Measuring the difference in physical parameters between these and the emitted photon offers information about the system. By selecting the appropriate resonance, the inelastic scattering cross section may be increased by several orders of magnitude, and information on the system's charge, magnetic characteristics, and orbital degrees of freedom can be collected.

The initial stage of RIXS is similar to the aforementioned RPES and XAS techniques. When the incident photon is absorbed, and an electron is excited to the unoccupied states from core-level and leaves a core-hole, which will be followed by a relaxation process through core-hole decay. Schematic illustration of the electronic states and transitions involved in the study of RIXS core-hole decay channels is described in Figure 2.11. In the RIXS, initially, a core level electron is excited to the lowest unoccupied molecular orbitals, in this case from the N 1s level. In the absence of charge transfer, two kinds of decay can occur, participator decay and spectator decay with X-ray emission.

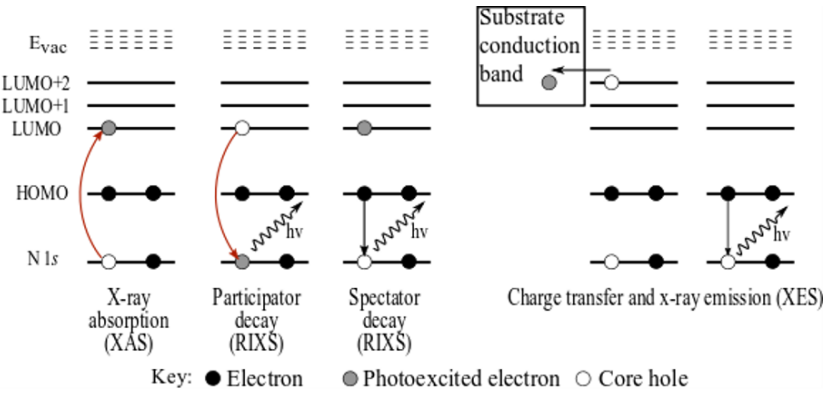



**Figure 2.11:** *Schematic illustration of the electronic states and transitions involved in the study of RIXS core-hole decay channels with the two main decay mechanisms - fluorescence/photon emission and Auger decay. RIXS describes the core-excitation of an N 1s electron to an unoccupied molecular orbital, participator, and spectator decay channels on the time scale of the core-hole lifetime. The charge transfer mechanism with subsequent x-ray emission is also illustrated here.*

### 2.2.6 Surface sensitivity

Surface sensitivity is one of the main advantages of employing photoemission spectroscopy for surface science research. The escape depth of photoelectrons is noticeably smaller than the soft X-ray penetration depth, which is on the order of microns [50]. Generally of the order of a few monolayers or nanometres. This is due to the intense interaction between electrons and matter; as a result, scattering events are frequent and the mean free path, which is determined by the electrons' energy, is short. The mean free path was calculated empirically using data from several measurements of inorganic and organic substances as well as common elements. Reference [51] contains an examination of these datasets, and one of the fits is shown plotted out in Figure 2.12.

The measured intensity of electrons passing through a material of thickness d is given by the following equation where the inelastic mean free path is defined as the distance through a material at which the electron intensity is attenuated by 1/e.

$$I = I_O \exp\left(-\frac{d}{\lambda(E)}\right) \tag{2.3}$$

where $I_0$ is the initial intensity of electrons and $\lambda$(E) is the inelastic free mean path. Equation 2.3 defines the intensity of photoelectrons generated from a depth d that reaches the surface and can be measured in the case of photoelectrons generated in the bulk of a sample. We can consider a realistic example case would be for $\lambda = 2\,\text{nm}$, corresponds to 1000 eV from the universal curve in Figure 2.12. In this scenario, about 5% of $I_0$ can be attributed to photoelectrons escaping from below 5 nm. In other words, the top 5 nm of the material account for 95% of the measured intensity. Generally speaking, we can state

$$\frac{I_d}{I_{total}} = 1 - \exp\left(-\frac{d}{\lambda(E)}\right) \tag{2.4}$$

where $\frac{I_d}{I_{total}}$ is the ratio between the measured photoelectrons that originate

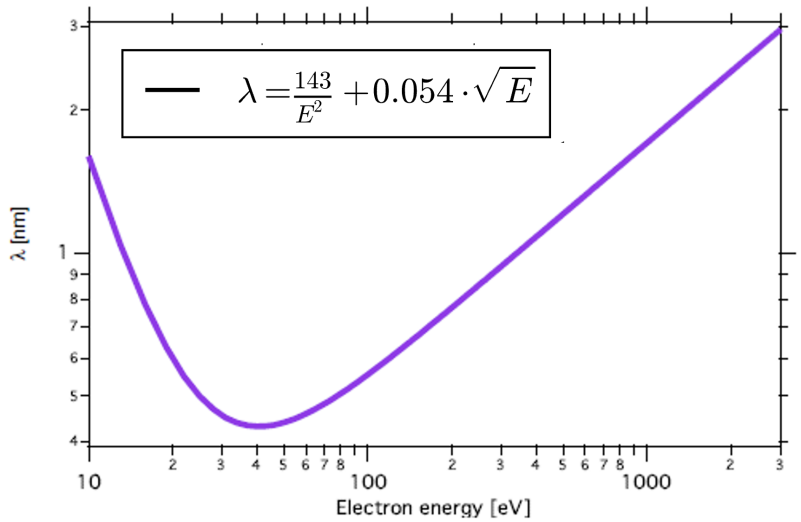



**Figure 2.12:** *The "Universal Curve" taken from the "elements" dataset in reference [51], showing the inelastic mean free path for electrons travelling through a solid. Where E is the electron energy.*

from within a depth d of the surface and the total measured intensity. Finally, we need to take into consideration the more general case where there is an angle between the surface normal and the entrance to the electron analyzer. We need to take into account the increased path length the electrons need to take, d/cos. Substituting this in and factoring out $I_0$ gives

$$\frac{I_d}{I_{total}} = 1 - \exp\left(-\frac{d}{\lambda(E)\cos\theta}\right) \tag{2.5}$$

This implies that the more grazing the sample is to the path of analyser, the more surface sensitive the measurement will be because electrons from within a depth d will make up a greater proportion of the measured signal [52].

### 2.2.7 Interpreting XPS spectra

#### Spin-orbit splitting

When photoelectrons are from orbitals with angular momentum, spin orbit coupling results in the splitting of XPS peaks. Such as spin-orbit splitting is possible for p, d and f orbital, and corresponding values of the angular

momentum are $l = 1$, 2, and 3 respectively. Spin-orbit splitting doesn't occur for the s levels for which $l = 0$. Without taking spin orbit coupling into account, we would anticipate that electrons of any spin would have the same kinetic energy - i.e. there is no degeneracy between the two electron configurations. The degeneracy results in peak splitting where the spin up and spin down electrons appear at slightly different energies due to their interaction with the orbital angular momentum vector.

A degeneracy is given by, Degeneracy = 2j+1, where the total angular momentum, j =$|l+s|$ and $l$ is the angular momentum quantum number. If the spin angular momentum vector is parallel to the angular momentum vector, so j = $l + \frac{1}{2}$, the interaction is favourable increasing the kinetic energy of the electron. If they are anti-parallel, so j = $l$ - $\frac{1}{2}$, the interaction is unfavourable reducing the kinetic energy. The size ratio of two peaks due to spin orbit splitting of an orbital can be determined by the ratio of the degeneracy values. This is listed for the sub-shells in Table 2.1.

| Orbital | j values | Degeneracy | Peak ratio |
|---|---|---|---|
| s ($l$ =0) | $\frac{1}{2}$ | 0 | |
| p ($l = 1$) | $\frac{1}{2}, \frac{3}{2}$ | 2,4 | 1:2 |
| d ($l = 2$) | $\frac{3}{2}, \frac{5}{2}$ | 4,6 | 2:3 |
| f ($l = 3$) | $\frac{5}{2}, \frac{7}{2}$ | 6,8 | 3:4 |

Table 2.1: Total angular momentum, electron degeneracy and resulting peak areas for XPS of s,p,d and f orbitals.

### Shake-up and Shake-off features

Shake ups and shake offs are the two resolvable loss processes. Figure 2.13 presents a schematic illustration of them. Another high-lying electron is excited as the primary photoelectron exits the atom or molecule by providing it with some energy. A high-lying electron may be excited to the vacuum level or above, which is known as shake off, or it may excite a high-lying electron to an unoccupied level, this event is known as shake up. The primary electron can be thought of as completely shaking an electron out of the atom or

molecule, or shaking an electron further up the energy level diagram. As a result, the measured photoelectron's kinetic energy is decreased, and the distance between the core level peak and the first shakeup satellite should be equal to the HOMO-LUMO gap. It is feasible for other shake-up satellites to form between different valence and unoccupied states that arise at even lower kinetic energy. Although the valence electron is discharged into the continuum of unbound states above the vacuum level during the shake-off process, it still uses the same mechanism. Therefore, shake-off features are quite broad and have the ability to blend into the background.

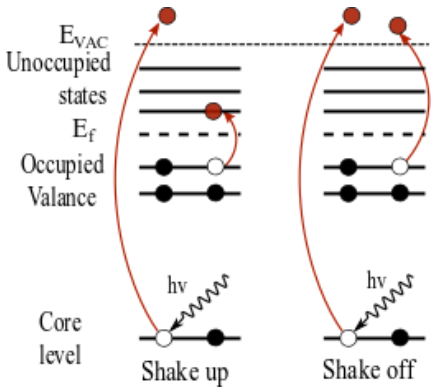



**Figure 2.13:** *Schematic Electronic energy level diagrams Demonstrating the shake up and shake off loss processes in photoemission spectroscopy.*

### Charging

The photoemission process is constantly removing electrons from the surface into the vacuum, which, in the extreme situation of the sample being an insulator, subsequently causes photoemission peaks to shift to higher binding energy and become very broad. By generating a cloud of low energy electrons over the surface of the measuring insulator that can replace lost electrons, electron flood guns can be employed to counteract this effect. When a conductive sample is grounded without the use of a flood gun, no net charge accumulates. On such a sample, thick non-conductive coating growth can nevertheless generate charging effects. Therefore, the position of XPS features in thick films may appear to be moved in relative to surface features or those of a comparable

thin film, even after adequate calibration of the binding energy scale.

#### Screening effects

The electrical coupling is strongest for thin films. Electronic interaction between a molecule and a metal surface can result in screening effects when there is a thin film of molecules on the metal surface. The polarisation of the atoms near the core hole [53] leads to screening by reducing the localised work function, which manifests as a shift to the lower binding energy. This final state effect can be utilised to monitor interactions between molecules and surfaces. In multilayer films, where XPS probes molecules close to the surface of the films, the screening effect is reduced.

## 2.3 Data processing

### 2.3.1 XPS data processing

#### Background subtraction

To fit the background under curves, many functions are utilised, allowing for peak fitting and other quantitative analysis. XPS backgrounds may be complicated; they are primarily caused by the accumulation of low energy secondary electrons and inelastic scattering, which means that simple linear backgrounds rarely offer an acceptable quality fit. The method used to fit the inelastic background utilised here was described by Shirley [54], who made the basic assumption that the intensity of the background is solely generated by the scattering of higher energy electrons. As a result, the background at a given energy is proportional to the integral of the intensity above that energy.

The Tougaard background [55] is an alternative to the Shirley background that was not used in this thesis but is discussed here for comparison. When detecting low kinetic energy peaks, spectra can frequently sit on the tail of the secondary electron cut-off. In this scenario, an exponential or power law fit of

the background was often applied.

#### Peak fitting

Several variables influence the form of XPS peaks, which lead to Gaussian or Lorentzian broadening. A mixture of these two functions is commonly employed for curve fitting via a pseudo-Voigt function, which uses a weighted sum of the two curves [56]. Following that comes a brief explanation of Lorentzian and Gaussian broadening.

#### Lorentzian contributions

The core hole life time ($\tau$) determines the fundamental limit of an XPS peak's width. The uncertainty principle may be used to estimate this Lorentzian contribution, known as the natural line width ($\Delta E_O$).

$$\Delta E_0[eV] = \frac{\hbar[eV.s]}{2\tau[s]} = \frac{6.6 \times 10^{16}[eV.s]}{2\tau[s]} \tag{2.6}$$

where $2\Delta E_O$ denotes the peak's full width (rather than half width) [57].

#### Gaussian contributions

The combined effects of different forms of broadening are often thought to be Gaussian [58]. These can include instrumental broadening, such as the energy resolution of the spectrometer or the X-ray source, as well as actual fluctuations in the energy of electrons in the sample, such as from vibrational broadening [59].

### 2.3.2 XAS data processing

#### Photon energy calibration

At a synchrotron, photon energy is frequently estimated by measuring the kinetic energy of a core level using both first and second order light generated by the beamline's monochromator. The first and second order peaks are found

at:

$$E_{K1} = h\nu - E_B \tag{2.7}$$

$$E_{K2} = 2h\nu - E_B \tag{2.8}$$

The difference in energy between these two spectra is thus equal to the photon energy. This works because every action that might modify the measured kinetic energy has an identical impact on both measurements. This approach was utilised after a XAS or RPES scan to determine the precise energy that the scan produced.

### Density of states

To generate a density of states plot, XAS data may be shown on a binding energy scale with valence band XPS measurements. The binding energy of a point in a NEXAFS spectrum can be expressed relative to the binding energy of the core hole created by the X-ray absorption process, which is referenced to the Fermi level by XPS measurements (the binding energy position of the N 1s core level is used for XAS over the nitrogen K edge). This can be achieved after calibrating the NEXAFS photon energy scale and the XPS binding energy scale, by subtracting the binding energy position of the core level from the NEXAFS photon energy scale. This principle is explained in Figure 2.14.

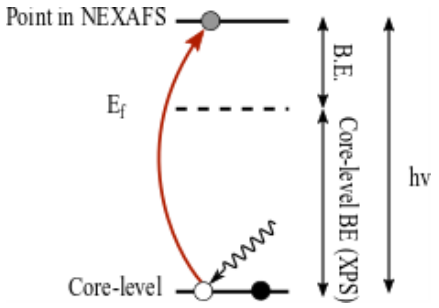



**Figure 2.14:** *Demonstrating how a NEXAFS data may be placed on a common binding energy scale with XPS measurements (referenced to the Fermi edge).*

It is important to note that this shows the position of the unoccupied energy levels in relation to the binding energy when in the core excited state.

## 2.4 Summary and Conclusions

In this chapter, an overview of ranging from sample preparation techniques to methods of characterization, as well as important experimental elements and synchrotron-specific characteristics is presented. A description of the primary X-ray methods applied in this work, together with the interactions between X-rays and matter: resonant inelastic X-ray scattering (RIXS), X-ray photoelectron spectroscopy (XPS), X-ray absorption spectroscopy (XAS), resonant photoemission spectroscopy (RPES), and the analysis performed for these techniques, including the core-hole-clock interpretation, and key features associated to the characterization techniques are discussed in detail.

# Chapter 3

# Annealing induced defect migration study on water exposed defective rutile $TiO_2(110)$

## 3.1 Introduction

The production of hydrogen through solar-driven water splitting has become a promising branch of next generation energy technology with the potential to provide low cost, sustainable and clean energy [60, 61]. The overview of the recent progress of photocatalysis on this topic has been discussed in many of the recent review articles [62–65]. In recent years, titanium dioxide has been studied extensively because it is recognised as an attractive photocatalyst due to its chemical stability, abundance and nontoxicity. Titanium dioxide has been widely considered as a candidate not only for water splitting [66] but also water purification [67, 68] and numerous other photocatalytic applications [69]. Further, titanium dioxide is well sensitised with dye molecules to increase visible light absorption [32] or photocatalytic properties can be modified by doping, [70] for example, stabilising reactive facets on the surface of the catalyst [71].

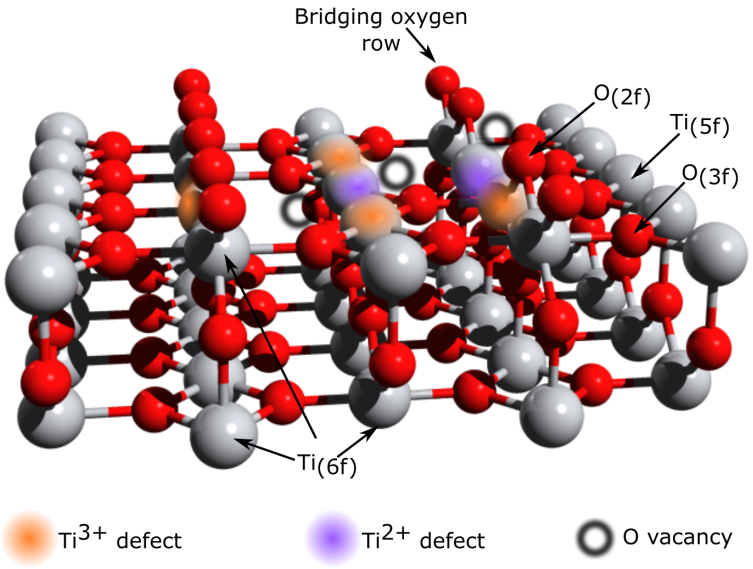



**Figure 3.1:** *The rutile $TiO_2$(110) surface, which in the defect free form consists of five and six fold coordinated Ti environments ($Ti_{(5f)}$ and $Ti_{(6f)}$) with corresponding two and three fold co-ordinated oxygen environments ($O_{(2f)}$ and $O_{(3f)}$). Examples of oxygen vacancies, both in a bridging oxygen row and in the main crystal structure are highlighted alongside corresponding Ti defects.*

The catalytic activity of titania depends heavily on the surface crystallinity, for example, exposure to (101) and (001) facets of anatase act as reduction and oxidation sites respectively [72]. In contrast, the rutile $TiO_2$(110) surface is not catalytically active as anatase but can be used to split water and produce stoichiometric quantities of hydrogen and oxygen [73].

Single crystal surfaces have been thoroughly investigated in an effort to better understand the underlying surface chemistry influencing catalytic performance as part of the endeavour to produce appropriate photoelectrodes for water splitting [74–77]. The structure of the rutile titanium dioxide (110) surface is shown in Figure Fig. 3.1. The bulk defect free rutile $TiO_2$(110) crystal consists of the six-fold coordinated titanium atoms and three-fold coordinated oxygen, but at the (110) surface, there are additional rows of two-fold coordinated oxygen, located at the bridge sites running in the [001] direction and five-fold coordinated titanium [40, 78]. It is now well acknowledged that the photocatalytic activity of titanium dioxide is significantly influenced by defects in the crystal structure. for example, water does not dissociate on the defect free $TiO_2$(110) surface [79, 80]. Water dissociations and water

chemistry[74, 80] on rutile $TiO_2$(110) are largely influenced by oxygen vacancies in the rows of bridging oxygen atoms and often dependent on the nature and density of these surface defect sites [81–84]. Water molecule dissociates into an $H^+$ and $OH^-$ near the oxygen vacancy site where the OH group fills the oxygen vacancy ($V_{Obridge}$) and an H atom that forms an identical species by binding to another bridging oxygen site ($O_{bridge}$). This mechanism can be presented as follows:

$$H_2O + V_{Obridge} + O_{bridge} \rightarrow 2OH_{bridge} \tag{3.1}$$

Defects in $TiO_2$(110) surface can be easily prepared by $Ar^+$ ion sputtering, which damages the crystallinity and preferentially removes oxygen atoms from both the crystal surface and sub-surface layers [42]. The resulting reduced single crystal rutile $TiO_2$(110) mainly consists of two types of defects, which are (i) oxygen vacancies (missing atoms in the rows of bridging oxygen rows) and (ii) titanium interstitials (titanium atoms which are not assigned to a lattice point and can move through the crystal)[40].

Oxygen diffusion via defect migration is well known for reduced $TiO_2$(110) and has relatively high defect mobility. Oxygen vacancies created at the surface by $Ar^+$ bombardment migrate to the subsurface via a site exchange mechanism and titanium interstitials diffuses through the crystal along the crystallographic c-axis [40, 41]. It is also well known that the overall stoichiometry of reduced rutile $TiO_2$(110) can be restored by annealing in a vacuum and the most considerable mechanism is bulk assisted oxidation, which entirely depends on the mobility of the defects. This process has two possible mechanisms, which are the oxygen vacancies diffusion mechanism and the titanium interstitial diffusion mechanism. In the oxygen vacancies diffusion mechanism, bulk supplies $O^{2-}$ anion to the reduced surface/subsurface. In the titanium interstitial diffusion mechanism, bulk receives excess $Ti^{3+}$ to restore surface stoichiometry. Both cases suggest that surface stoichiometry can be restored

by the migration of defect to and from bulk [42]. It is also found in the earlier investigation that the presence of small quantities of water vapor increases the diffusivity of oxygen vacancies or decreases the diffusivity of titanium interstitials [85].

It is not unexpected that the relationship between water and defective titanium dioxide surfaces has been widely explored using a variety of techniques given the importance of defect chemistry on the catalytic activity of titania [83, 86–91]. Near ambient pressure X-ray photoelectron spectroscopy (NAP-XPS) is a very powerful technique to investigate the water interaction with metal oxide surfaces. So far, a lot of investigations have been carried out on water interaction with $TiO_2$ in near ambient pressure. The effect of oxygen vacancies as water nucleation sites has been investigated on rutile $TiO_2(110)$ [81] and on the anatase $TiO_2(101)$ [92]. The oxygen vacancies created on anatase surface by $Ar^+$ sputter migrate to the subsurface and has higher photocatalytic reactivity because the subsurface defect has a tendency to lie subsurface, trap photoexcited charge carriers, are not so easily quenched by adsorbed ambient molecules, including water if they remain subsurface [92, 93]. This differs from rutile where oxygen defects are more common on the surface (compared to the sub-surface), where they are stable and tend to remain [92, 93]. Water dissociation on rutile occurs directly at these surface oxygen vacancies [94]. This difference has also been studied computationally [95].

In this study, highly defective rutile $TiO_2(110)$ was prepared by $Ar^+$ ion sputtering and the defective surface was healed in-situ by exposure to liquid water using near-ambient pressure XPS instrument. Subsequent XPS measurements confirm a defect-free surface, whilst the subsurface remains highly defective. The resulting combination of a defect-free surface and a highly defective sub-surface is used as a platform for an XPS study of annealing-induced defect migration.

## 3.2 Method

A SPECS DeviSim near ambient pressure X-ray photoelectron spectroscopy (NAP-XPS) system equipped with a UHV chamber, interchangeable NAP reaction cell, and Phoibos 150 NAP hemispherical analyzer was used to conduct this experiment. It is possible to prepare the sample in the UHV chamber and transfer it to the NAP-cell without breaking the vacuum, this arrangement has been described elsewhere [96]. The NAP-cell used allowed precise control of the sample temperature, in the $\sim \pm 50\,^{\circ}\mathrm{C}$ range using a thermoelectric Peltier heater/cooler via a proportional integral derivative (PID) controller and a thermocouple mounted on the sample plate beneath the crystal.

A rutile $TiO_2(110)$ crystal (PI-KEM Ltd.) was cleaned in the UHV chamber, by rounds of 1 kV argon-ion sputtering and 800 K annealing until no evidence of contamination or surface defects were visible in the XPS. Then the sample was sputtered at 2 kV argon ion for 10 minutes to create a highly defective surface and subsurface. The crystal was then transferred to the NAP-cell. Deionized water using a Triple Red purification system and further degassed by freeze-pump-thaw cycles was connected to the cell via a UHV leak valve. Liquid film of water on the surface was achieved by condensation of water vapor by cooling the sample to 275 K and increasing the pressure of water in the NAP-cell to 6 mbar, which corresponds to 100% RH at this temperature. After liquid water exposure, the NAP-cell was pumped down and the sample transferred to the UHV chamber (base pressure in the low $10^{-10}$ mbar range) where the sample was then annealed in situ using an electron beam heater behind the sample plate. The temperature during annealing was measured using a thermocouple located at the edge of the sample plate ($\sim$3 mm from the edge of the sample).

XPS measurements in the UHV chamber and NAP-cell were made at 20 eV and 40 eV pass energy respectively. The geometry of the NAP-cell allowed measurement at normal emission (NE). In UHV, XPS measurements

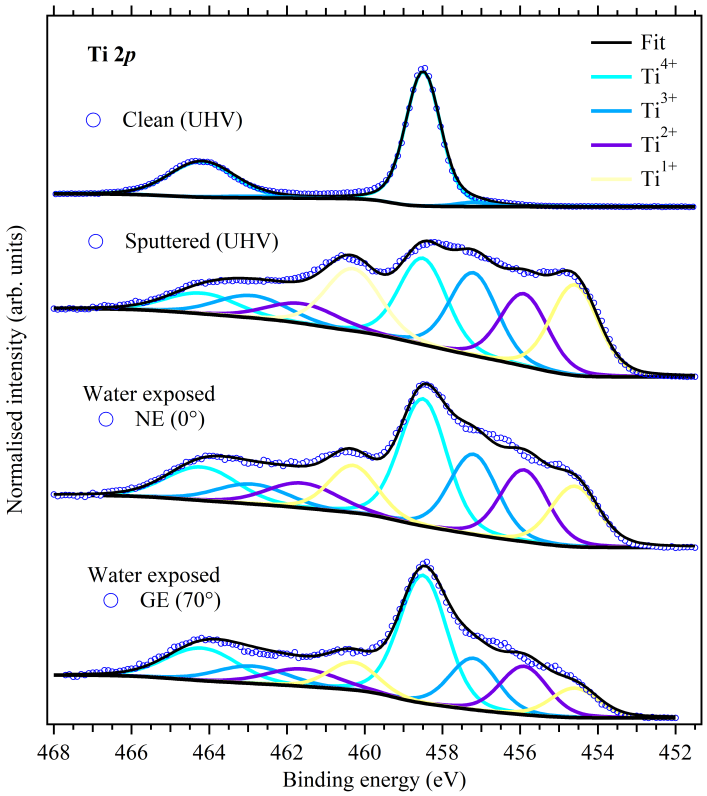



**Figure 3.2:** *Ti 2p XPS measurements of 'clean' surface prepared by sputtering and annealing, 'sputtered' surface created by $Ar^+$ sputtering, and 'water exposed' surface taken after healing the surface defect. All surfaces measured at normal emission (NE) but the 'water exposed' surface also measured at* 70° *grazing emission.*

were taken at both NE (0°) and 70° grazing emission (GE). Monochromatic Al k$\alpha$ X-rays (h$\nu$ = 1486.6 eV) were used for all measurements. The O 1$s$ XPS peak at a binding energy of 530.05 eV was used for calibrating the binding energy scale [27]. Peak fitting was performed using a pseudo-Voigt line shape into a fixed Lorentzian width (0.3 eV) and variable Gaussian width following the subtractions of a Shirley background [97].

## 3.3 Results and Discussion

Figure 3.2 shows Ti 2$p$ XPS measurements of rutile $TiO_2$(110) following three sequential preparation stages: 'clean', 'sputtered' and 'water exposed' surfaces respectively. The 'clean' sample was prepared by sputtering and annealing in UHV. The sample was then sputtered by $Ar^+$ ion at 2 KeV to create 'sputtered' surface. Finally, the 'water exposed' surface was obtained by liquid water

exposure. The 'clean' spectrum shows a doublet attributed to $Ti^{4+}$ with a trace of residual $Ti^{3+}$ defects which are visible as a shoulder at the lower binding energy side of $Ti^{4+}$ [40]. After sputtering, a series of lower binding energy features created in the 'sputtered' spectrum extended down to ~453 eV. Sputtering preferentially removes oxygen from the surface and subsurface and creates lower oxidation states ($Ti^{3+}$, $Ti^{2+}$, $Ti^{1+}$), suggesting the presence of non-stoichiometric oxides[82] as $Ti_2O_3$, $Ti_2O$, and TiO. We have curve fitted to four spin-orbit doublets associated with lower Ti oxidation states ($Ti^{3+}$, $Ti^{2+}$, $Ti^{1+}$) that result from the removal of oxygen atoms [82, 98]. These defects extend nanometers into the surface. This highly defective sample was then subsequently exposed to liquid water in an effort to heal the defects at the crystal's surface. Figure 3.3 displays the in-situ data collected during this process. The sample was exposed to liquid water during the fourth XPS spectra (i.e. scan 4) and remained exposed until the nineteenth spectra. The sample temperature was held at 275 K. The high binding energy tail on the UHV (before NAP-cell) spectrum is attributed to defects in the lattice caused by the sputtering and this intensity is further increased slightly in the NAP cell due to the adsorption of a small amount of residual water from the NAP-cell itself.

Figure 3.2 also shows Ti $2p$ spectrum after water exposure on the rutile $TiO_2$ (110) surface. This spectrum shows that the relative intensities of the subsequent Ti oxidation states decrease. Figure 3.4 shows repeatedly prepared water healed surface by exposure to liquid water at the defective surface. This preparation process consistently produced relatively identical defect concentrations.

The surface sensitivity of XPS can be varied by changing the angle of the sample with respect to the spectrometer [99]. The escape depth of Ti $2p$ photoelectrons at NE (0) and GE (70) were calculated to be ~7 nm and ~2 nm respectively, using the formula described elsewhere[100], considering inelastic mean free path (IMFP) for a substrate signal attenuated by 95% .

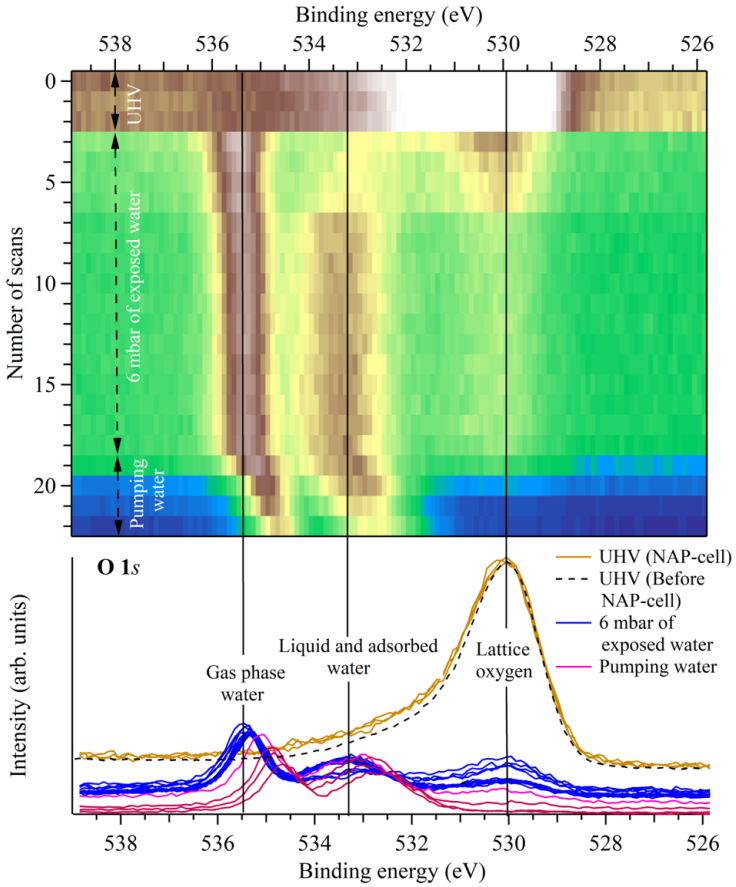



**Figure 3.3:** *O 1s XPS of the sputtered $TiO_2$ measured at normal emission in-situ during preparation of defect-free surface (above highly defective sub-surface) by exposure to liquid water in the NAP-cell. All the spectra were measured at normal emission*

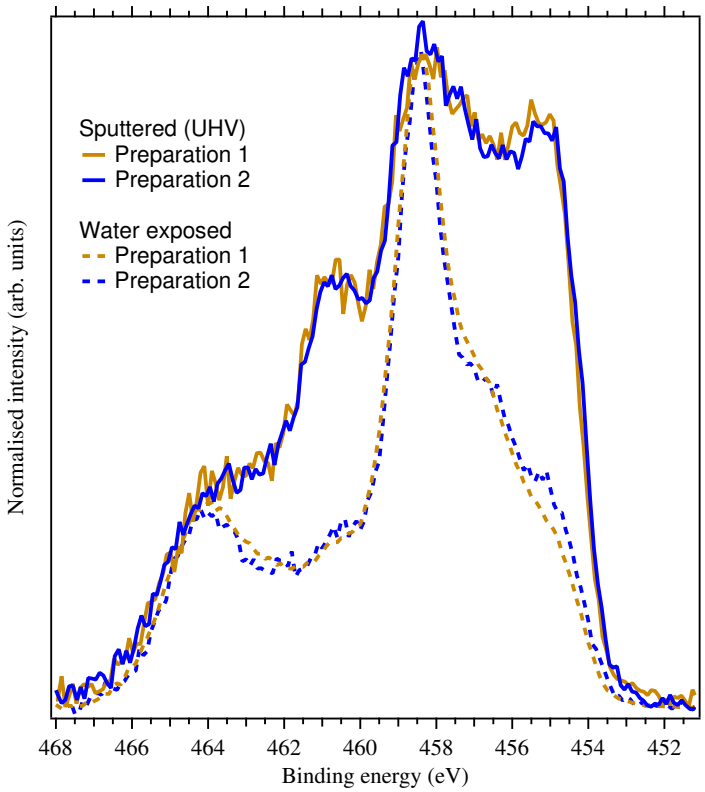



**Figure 3.4:** *Ti 2p XPS spectra of repeatedly prepared water healed surface and defective sub-surface (dashed lines) by exposure to liquid water from similar defect concentration (solid lines) of rutile $TiO_2(110)$ created by $Ar^+$ sputter. All the spectra were measured at grazing emission.*

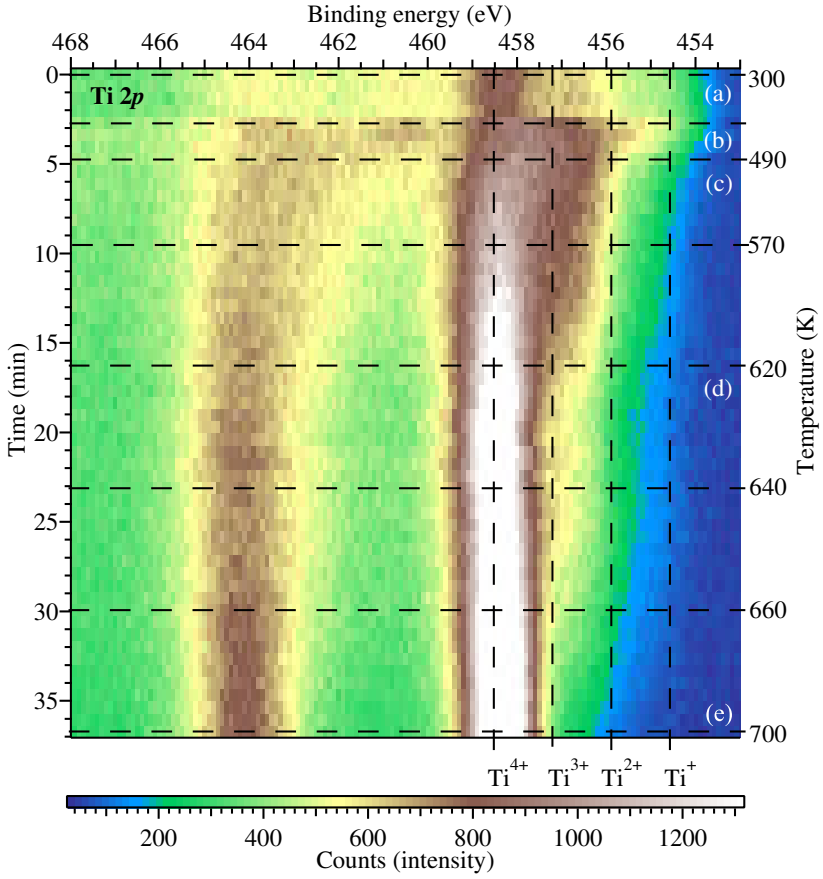



**Figure 3.5:** *In situ XPS measurements of Ti 2p spectra during annealing of water exposed rutile $TiO_2$ (110). Horizontal lines indicate annealing temperature of corresponding time during measurements and horizontal line marked (a - e) were extracted for detailed analysis in Fig. 3.6.*

XPS measurement at NE and GE emission in Figure 3.2 implies that the water exposed surface is less defective than the bulk as, when compared to the NE data, the more surface sensitive GE spectrum (Water exposed GE) shows fewer defect states relative to the $Ti^{4+}$. This is consistent with an independent study, where they measured XPS data on water exposed defective $TiO_2$ surfaces and also found that defects at the surface are healed more readily than those sub-surface [101]. The defective states do not disappear completely after water exposure in the GE spectrum presented in Figure 3.2 because the calculated information depth (inelastic mean free path of the electron) is $\sim$2 nm and it is assumed that water exposure only heals defects directly accessible on the surface.

Figure 3.5 provides information about the change of defective states of the water healed sample as a function of the time and temperature during annealing in UHV. During the first three minutes of annealing, the intensity of the defect state increase. After that, the defect state decreases slowly. This trend continued until the sample is dominated by $Ti^{4+}$ as the temperature approaches 700 K.

For better understanding, five individual Ti $2p$ spectra labelled (a)-(e) have been selected for curve fitting to explain the variation of intensity of defects and presented in Figure 3.6, alongside the corresponding O $1s$ spectra. The curve fitting makes it possible to identify the spectrum contribution of the various Ti oxidation states. The peak located at 458.5 eV correspond to the Ti $2p_{3/2}$ of the $Ti^{4+}$ oxidation state of $TiO_2$ [102]. The three peaks located at 457.2 , 455.9 and 454.6 eV are attributed to the $Ti^{3+}$ $2p_{3/2}$, $Ti^{2+}$ $2p_{3/2}$ and $Ti^{1+}$ $2p_{3/2}$ oxidation states respectively. A branching ratio of $0.45 \pm 0.03$ and a spin-orbit splitting of 5.7 eV was used to determine the appropriate fit components for the Ti $2p_{1/2}$ states. Due to multiplet splitting, the $Ti^{3+}$, $Ti^{2+}$ and $Ti^{1+}$ peaks are likely to be broadened with a rather complicated line shape. We have chosen to keep the peak fitting as simple as possible and have not modelled the multiplet splitting, which will actually cause an asymmetric broadening

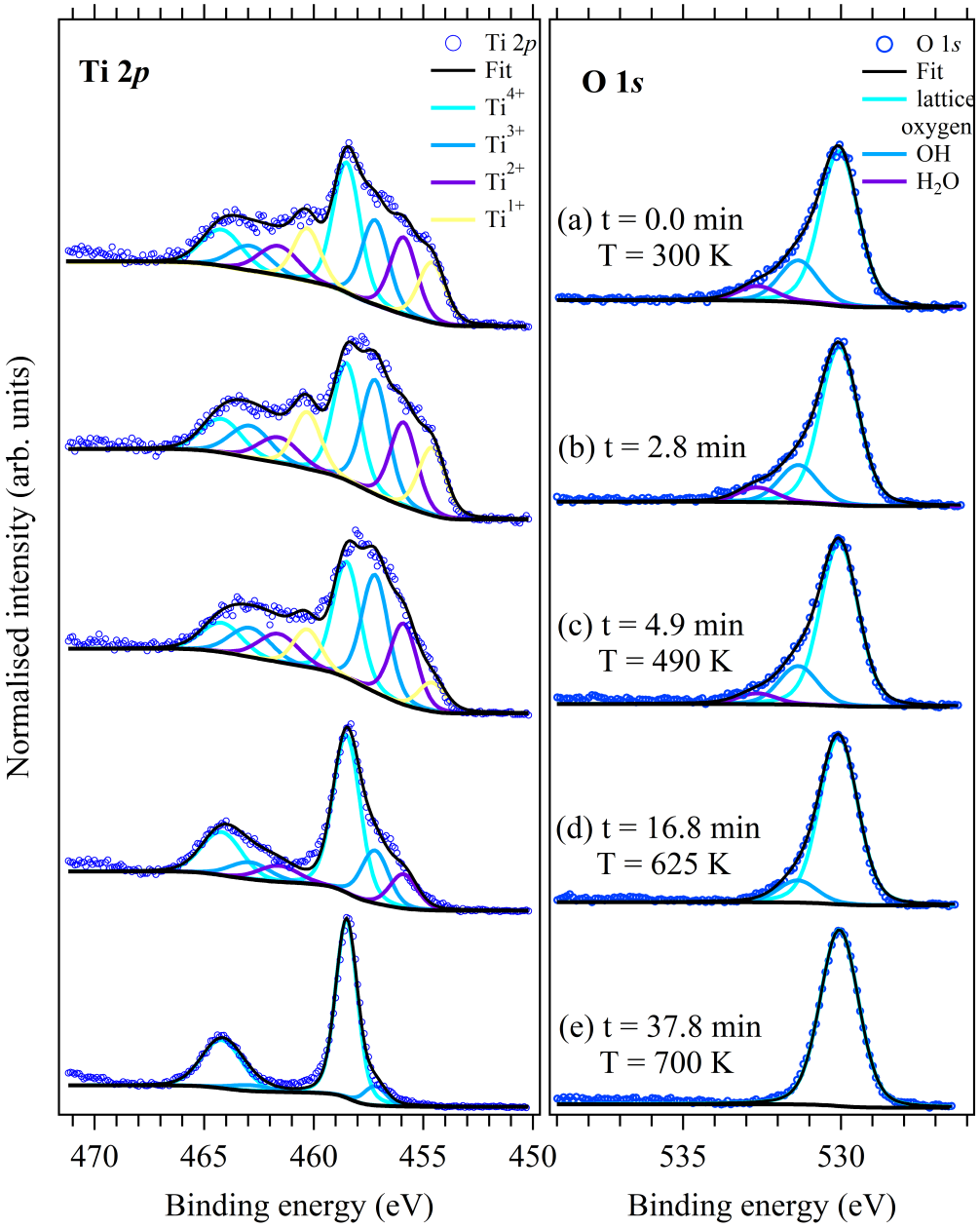



**Figure 3.6:** *(Left) Ti 2p spectra displays the migration ((a) to (b)) and transformation of intermediate oxidation states ((c) to (e)) of $TiO_2$ (110) during annealing. (Right) corresponding O 1s spectrum, which represents the change of lattice oxygen, hydroxyl group, and adsorbed water during annealing after water exposure. All the spectra were measured at normal emission.*

of the $Ti^{3+}$, $Ti^{2+}$ and $Ti^{1+}$ on the higher BE side. Since the intensity of the multiplet peak is likely to be very small in comparison to the main peak, it is likely that this decision will not significantly alter the quantitative analysis we present. During the first minute of annealing, the intensity of the $Ti^{3+}$ feature is observed to increase as shown in Fig. 4.3 (a), (b). After this point, starting from t≈5 minute (Fig. 4.3(c), T≈490 K) the intensity of the lower oxidation states has decreased and continued to decrease as time goes on and the temperature rises.

The O 1*s* spectra in Figure 3.6 are fitted with three peaks. The peak at 530.05 eV corresponds to lattice oxygen, whereas the features located at 1.3 and 2.6 eV higher binding energy than the lattice oxygen peak attributed to adsorbed hydroxide and water, respectively. The relative positions of these features are consistent with a previous study of a water exposed rutile $TiO_2$(110) surface [81]. The intensity of the adsorbed hydroxide and water features remain similar during the first two spectra ((a), (b)). However, in the third spectrum (c), at t≈5 minute and (T≈490 K), indicates a loss of adsorbed water. The molecular water is no longer observed and the OH peak has started to decrease by fourth spectra (d), at t≈17 minute and T≈620 K. Finally, by t≈38 minute and T≈700 K, the hydroxide and molecular water features are completely disrobed as shown in Figure 3.6(e) spectrum. This is consistent with the reported experiment on water exposed $TiO_2$ surfaces showing that hydroxide and adsorbed water do not desorb below 550 K [101]. It is interesting that we do not observe a decrease in the hydroxide/water features at lower temperatures, which may indicate that the water is not actively helping to heal any $Ti^{3+}$ defects that may have migrated to the surface. This is possible because physisorbed water is not kinetically active enough in comparison to the gas and liquid phases, which are known to help heal defects. The entire experiment was repeated using in-situ XPS measurements at a more surface sensitive grazing emission angle after we healed the defective surface with water exposure and tracked the defect while annealing. The curve fitted Ti 2*p*

XPS of five individual chosen spectra has been presented in Fig. 3.7, alongside the corresponding O 1*s* spectra.

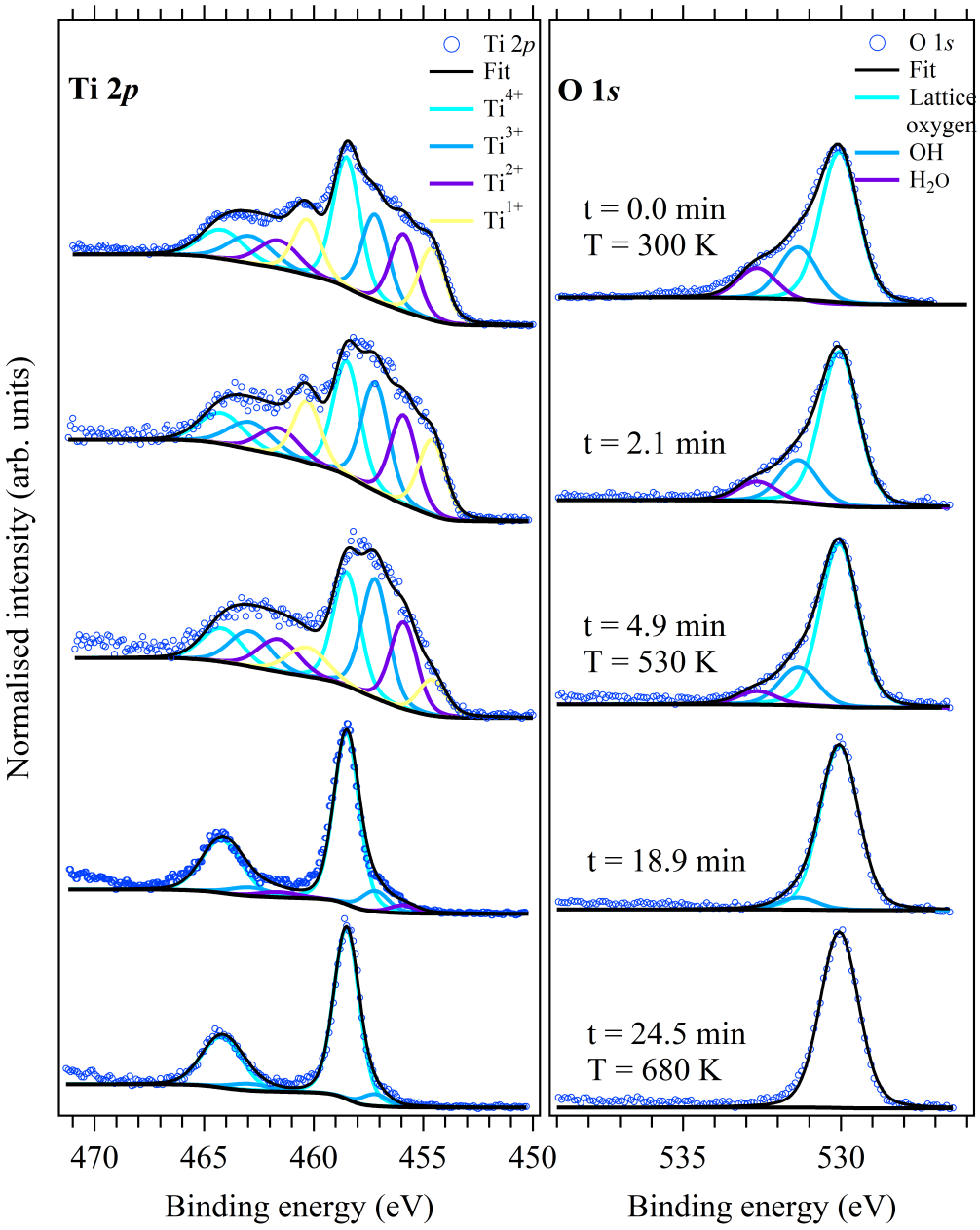



**Figure 3.7:** *Left: Ti 2p spectra where peak fitting tracks the behaviour of intermediate Ti oxidation states during annealing. Right: associated O 1s spectra highlighting the relative change of lattice oxygen, hydroxyl groups, and adsorbed water. All the spectra were measured at grazing emission.*

Figure 3.8 provides information about the quantitative changes of the relative concentration of all oxidation states of titanium during annealing as a function of time and temperature measured at (a) NE and (b) GE. To facilitate discussion, the plot measured at NE has been chosen and divided into three

sections, A through C. We do emphasise, however, that there may be an overlap between the boundaries of these regions and the mechanisms dominating the behaviour in the regions.

In region A, that is for the first $t \approx 3$ minute shows a decrease in $Ti^{4+}$ concentration, whereas the concentration of $Ti^{3+}$ increases and the corresponding concentration of lower oxidation states remains almost constant. This indicates that $Ti^{3+}$ defects are likely migrating from the sub-surface *to* the surface during low annealing temperature until the concentration between the surface and subsurface is minimised as the $Ti^{4+}$ reaches a minima at $t \approx 3$ minute.

In region B, between $t \approx 3$ and $t \approx 6$ minute, With increasing annealing temperature the concentration of $Ti^{1+}$ decreases dramatically, whereas the concentration of $Ti^{4+}$ and $Ti^{3+}$ increase proportionally. The concentration of $Ti^{2+}$ remains constant. If the conversions of $Ti^{1+} \rightarrow Ti^{2+}$ and $Ti^{2+} \rightarrow Ti^{3+}$ have equal rates, then this might perhaps be consistent with progressive conversion of $Ti^{1+} \rightarrow Ti^{2+} \rightarrow Ti^{3+} \rightarrow Ti^{4+}$; alternatively, intermediate oxidation states may be skipped. Regardless, region B represents a dramatic transition with an activation energy corresponding to a temperature of $\sim$490 K where $Ti^{1+}$ is no longer stable.

In region C, beyond $t \approx 6$ minutes, the $Ti^{1+}$ concentration approaches zero percent, the $Ti^{2+}$ and $Ti^{3+}$ start to gradually and steadily fall at a similar rate, and the $Ti^{4+}$ increases accordingly at a slower rate than in region B. This regime, which finally produced essentially a defect-free spectrum, is attributed to the progressive diffusion of oxygen vacancies and Ti interstitials between the crystal bulk and surface/sub-surface layers. Towards the higher anneal temperatures, where the bridging oxygen atoms are no longer hydrogen terminated, it is possible that residual water in the vacuum chamber may contribute to the healing of surface defects via the water dissociation mechanisms discussed in the introduction section [88, 91, 103].

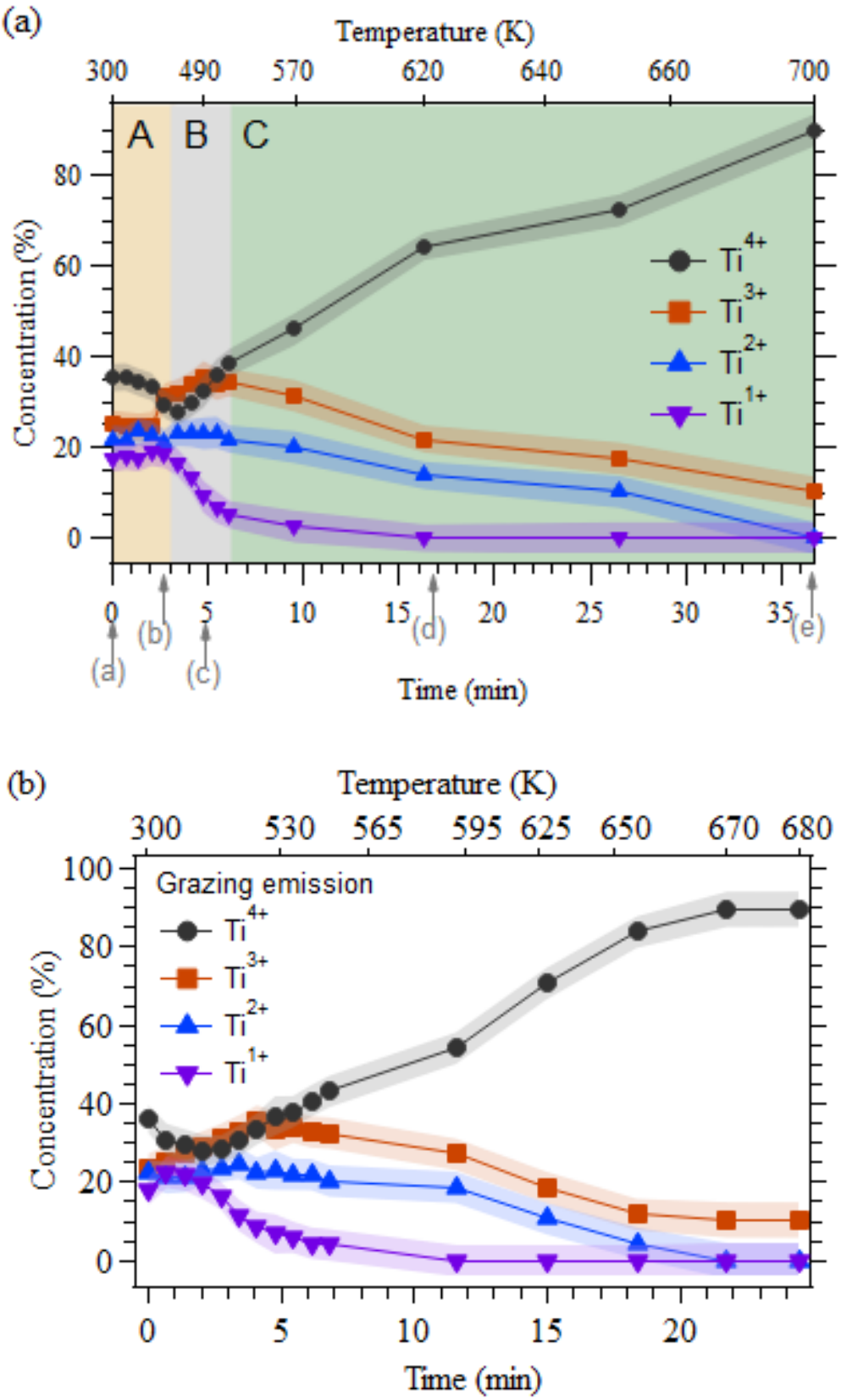



**Figure 3.8:** *Defect concentration, extracted from peak fitting of Ti 2p (a) normal emission (b) grazing emission XPS data (examples in figure 4.3) as a function of time and temperature. Shaded regions around the datapoints indicate an estimated error bar calculated from the standard deviation of the fit residual. Regions A to C represent stages of the annealing process as discussed in the text. Arrow indicated label (a)-(e) corresponds to the spectra presented in Figure 3.6.*

Although the rapid depletion of $Ti^{1+}$ observed in region B is not observed for $Ti^{2+}$ or $Ti^{3+}$, it is worth noting that the rate of heating is much greater at the start of annealing; to an approximation, the temperature change during regions A and B (∼6 min) is comparable to the ∼30 min elapsed in region C. The data reported here cannot distinguish between the effects of annealing temperature and time. As a result, we believe that investigating the processes described here using an instrument optimised for exact temperature controlled XPS measurements would be extremely beneficial in disentangling the thermodynamics from the kinetics and providing more accurate transition temperatures.

## 3.4 Summary and Conclusions

Defective rutile $TiO_2(110)$ prepared by $Ar^+$ sputtering was subjected to liquid water exposure, which hydroxylates the sputtering-created surface oxygen vacancies. The result was a sample with a substantially defective subsurface coexisting with a defect free surface, offering a platform for studies of annealing-induced migration of titanium defects using XPS. We observed an increase in $Ti^{3+}$ concentration at low annealing temperatures, which we attribute to $Ti^{3+}$ migration to the previously defect-free surface. Around 500 K, a fast and distinct depletion of $Ti^{1+}$ is seen, with a corresponding increase in $Ti^{3+}$ shortly followed by $Ti^{4+}$, which is possibly explained by the gradual conversion of $Ti^{1+}$ defects to $Ti^{4+}$ through intermediate oxidation states. We observe a steady fall of the remaining defect concentration at higher annealing temperatures, most likely through known titanium interstitial and oxygen vacancy diffusion mechanisms. The experimental evidence of defects migrating to the surface of rutile at low annealing temperatures is important for the industrial application of titania catalysts, and the methodology presented here is a useful tool for studying the kinetics and thermodynamics of defect migration in a variety of materials.

# Chapter 4

# Water, oxygen and ambient pressure exposure on defective rutile $TiO_2$(110)

## 4.1 Introduction

Titanium dioxide ($TiO_2$) is recognised as one of the most studied materials in surface science due to its numerous application in the production of hydrogen through photocatalytic water splitting [104, 105], dye sensitised solar cells [6], decontamination of air [106] and water purification [107, 108]. However, the photocatalytic water splitting performance of stoichiometric single crystal rutile $TiO_2$(110) still remains unsatisfactory due to its poor photogenerated carrier separation efficiency and insufficient light absorption [109–111]. To extend the absorption edge of the solar spectrum to the visible region and reduce the recombination of electron-hole pairs to enhance the photocatalytic activity it has become necessary to modify the surface of the $TiO_2$. For example, a series of metals and nonmetals have been introduced to partially replace titanium and oxygen atom in the $TiO_2$ lattice [112, 113].

It has been also reported that the ideal defect free $TiO_2$ surface is not reactive with water and oxygen molecules at room temperature [79, 80, 114].

The chemistry of $TiO_2$ surfaces is often dominated by the nature and density of surface defect sites [81–84]. Several research works in recent years confirms that water dissociation occurs at oxygen vacancy defects [88] and the molecular water is adsorbed on the fivefold coordinated $Ti^{4+}$ sites. The water molecules dissociates into $H^+$ and $OH^-$ near oxygen vacancy sites where $OH^-$ group fills an oxygen vacancy ($V_{Obridge}$) and the H binds to a neighbouring bridging oxygen ($O_{bridge}$) which leads to the formation of an additional OH group on the surface. This mechanism can be presented as follows:

$$H_2O + V_{Obridge} + O_{bridge} \rightarrow 2OH_{bridge} \tag{4.1}$$

Whereas, oxygen atom from an $O_2$ molecule fills an oxygen vacancy ($V_{Obridge}$) while the other oxygen atom remains on the surface as an oxygen adatom ($O_{adatom}$) bounds to the fivefold $Ti^{4+}$. This oxygen adatom ($O_{adatom}$) works as additional water dissociation sites and creates two identical OH groups. This mechanism can be presented as follows:

$$O_2 + V_{Obridge} \rightarrow O_{bridge} + O_{adatom} \tag{4.2}$$

$$O_{adatom} + H_2O \rightarrow 2OH_{bridge} \tag{4.3}$$

The structure of the bulk $TiO_2$ crystal consists of sixfold coordinated titanium atoms and threefold coordinated oxygen atoms but the structure of the (110) surface is different to the bulk. The surface consists of additional rows of twofold coordinated oxygen and fivefold coordinated titanium. Oxygen defects can be created by UV irradiation [115], annealing in high temperature in ultra high vacuum but the most effective way to create highly defective surface is $Ar^+$ ion sputtering [43]. $Ar^+$ ion sputtering generates a reduced surface by removing oxygen atoms from crystal surface which results in creating two types of defects: oxygen vacancies and titanium interstitials [40].

The overall stoichiometry of reduced rutile $TiO_2(110)$ can also be restored by annealing in a vacuum and the most significant mechanism is bulk assisted oxidation, where the bulk supplies $O^{2-}$ anion to the reduced surface and receives excess $Ti^{3+}$ from the surface to restore surface stoichiometry [42]. This mechanism has already been discussed in depth in section 1.4.

In real-life applications, catalytically active systems are typically used in high pressure. To understand the surface chemistry of defective rutile $TiO_2(110)$ in ambient conditions, at first the defective surface created by $Ar^+$ ion sputtering (at 2 keV for 10 minutes) was exposed to water, oxygen and 5 mbar air and then the sample was transferred out of the UHV system and exposed to ambient pressure. After exposure to ambient pressure, the sample was transferred back to the UHV system and measured XPS to observe the change in the defective states. This procedure was carried out several times and each time the defective sample was exposed to ambient pressure at different temperatures. The idea is to investigate the effect of different annealing temperatures on the defect intensities.

## 4.2 Method

A SPECS DeviSim near ambient pressure X-ray photoelectron spectroscopy (NAP-XPS) system equipped with an ultra-high vacuum (UHV) preparation/analysis chamber and Phoibos 150 NAP hemispherical analyzer used to conduct measurements. A rutile $TiO_2(110)$ crystal (PI-KEM Ltd.) was mounted and cleaned in the UHV chamber, by rounds of 1 kV argon-ion sputtering and 800 K annealing until no evidence of contamination were visible in the XPS. The sample was then sputtered at 2 kV for 10 min to create a highly defective surface before each exposure to molecules or ambient pressure. The sample was transferred to the NAP-cell without breaking the vacuum and the NAP-cell was docked to the analyzer before subjected to 0.2 mbar water, 1 mbar oxygen and 5 mbar air for 1 hour respectively. The NAP-cell was then

pumped down and the sample returned to the UHV chamber for XPS measurement. For the purpose of exposing the sample to the ambient pressure and annealing in ambient pressure, the highly defective sample was transferred out of the NAP-XPS and placed onto the Stuart UC152 Stirring Hotplate. This hotplate was used to anneal the samples at 323 , 373 , 423 , 523 and 723 K temperature for one hour respectively. After annealing, the sample was transferred back to the UHV chamber where XPS measurements were taken.

XPS can be measured in the NAP-cell at normal emission (NE) and in the UHV chamber at normal emission (NE) and grazing emission (GE). The base pressure recorded during the experiments in the analysis chamber was in the low $10^{-10}$ mbar range. Monochromatic Al k$\alpha$ X-ray source (h$\nu$ = 1486.6 eV) used to conduct this experiment and XPS measurements in the UHV chamber and NAP-cell were made at 20 eV and 40 eV pass energy respectively. The binding energy scale was calibrated using the oxide lattice O 1$s$ peak previously measured to have binding energy of 530.05 eV [82].

## 4.3 Results and Discussion

### 4.3.1 $Ar^+$ ion sputtered rutile $TiO_2$(110) surfaces

It is crucial to fit defect peaks in O 1$s$ XPS spectra in a way that should agree with the defect intensities of the corresponding Ti 2$p$ spectra in order to comprehend the change in the defect concentration with increasing sputtering duration and energy. Assuming that the lattice oxygen peak doesn't move after ion sputtering, the Ti 2$p$ and O 1$s$ spectra in Figure 4.1 represent an initial attempt of the peak fitting operation.

Figure 4.1 shows Ti 2$p$ and O 1$s$ XPS spectra of rutile $TiO_2$ (110) after defect creation by using $Ar^+$ ion bombardment as a function of sputtering voltage and time. The spectra presented here following the consecutive $Ar^+$ ion bombardment at 500 V for 10, 20, 30 seconds, at 1 keV for 1 , 2, 4 minutes

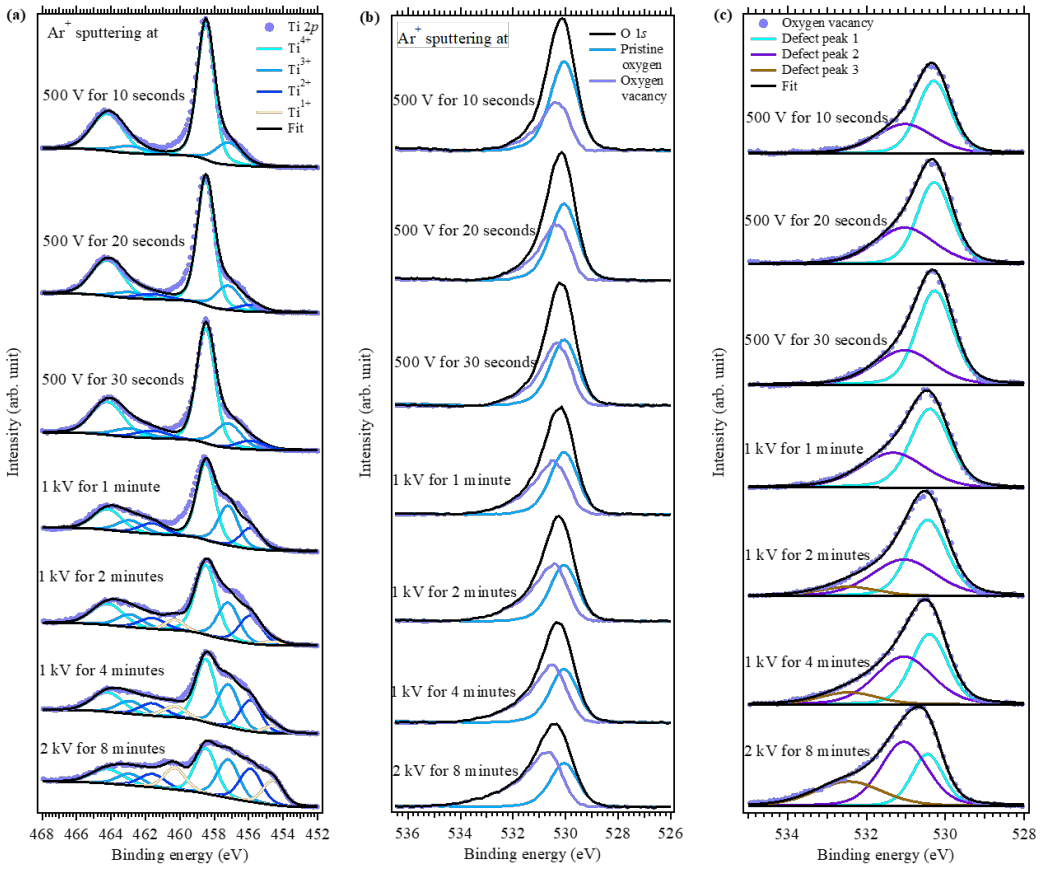



**Figure 4.1:** *Defective surface created by $Ar^+$ sputtering at* 500 V *for 10, 20, 30 seconds, at* 1 keV *for 1 , 2, 4 minutes and at* 2 keV *for 8 minutes respectively. (a) Ti 2p XPS spectra consisting peak fitting to demonstrates the change of intensity of the Ti oxidation states. (b) Oxygen vacancy peak obtained by subtracting stoichiometric oxygen from defective O 1s spectra (c) Oxygen vacancy spectra consisting peak fitting to demonstrates the change of intensity of the defective states respectively. All surfaces measured at normal emission (NE).*

and at 2 keV for 8 minutes. For better understanding, the individual Ti $2p$ and O $1s$ spectrum have been peak fitted, which allows determining the spectral contribution of the different Ti oxidation states and presented in Figure 4.1. For details component analysis of oxygen vacancy from O $1s$ spectra, the stoichiometric oxygen peak has been subtracted from each and every O $1s$ spectrum and peak fitting is carried out, as shown in Figure 4.1(b).

In Figure 4.1 (a), the peak is located at 458.5 eV corresponds to the Ti $2p_{3/2}$ of the $Ti^{4+}$ oxidation state of $TiO_2$. The three peaks located at 457.2 , 455.9 and 454.6 eV are attributed to the $Ti^{3+}$ $2p_{3/2}$, $Ti^{2+}$ $2p_{3/2}$ and $Ti^{1+}$ $2p_{3/2}$ oxidation states, respectively. A branching ratio of $\sim 0.45 \pm 0.03$ and a spin-orbit splitting of 5.7 eV was used to determine the appropriate fit components for the Ti $2p_{1/2}$ states. We have opted to keep the peak fittings as simple as possible and not modelled the multiplet splitting (see section 2.2.7), which in reality will lead to an asymmetric broadening of the $Ti^{3+}$, $Ti^{2+}$ and $Ti^{1+}$ on the higher binding energy side and the intensity of the multiplet peak is likely very small in comparison with the main peak so likely only makes a small difference to the quantitative analysis we present. As shown in Figure 4.1(c), it is impossible to fit with a single defect peak without considering an extremely broad second defect peak to obtain a good fit. The peak associated with oxygen near oxygen vacancies is fitted with two peaks located at 530.25 eV and 531.05 eV. As the peak associated with oxygen near oxygen vacancies grows with $Ar^+$ ion sputtering for 2, 4 and 8 minutes, a third peak located at higher binding energy 532.45 eV is also added. On sputtering at 500 V for 10 seconds, a small feature located at 457.2 eV binding energy of Ti $2p$ spectrum observed due to the creation of $Ti^{3+}$ oxidation state as oxygen is removed from the surface. Creation of $Ti^{2+}$ and $Ti^{1+}$ oxidation states is also observed as the sputtering time increases. The highly defective surface obtained after sputtering at 2 keV for 8 minutes. The corresponding peak associated with oxygen near oxygen vacancies obtained from the O $1s$ by subtraction shows a higher amount of oxygen vacancies and disagrees with the quantitative analysis

of Ti oxidation states presented in the Ti $2p$ spectra. This assumption might not be accurate. The area of the peak associated with oxygen near oxygen vacancies obtained from the O $1s$ spectrum has to be consistent with the oxygen vacancies obtained from the corresponding Ti $2p$ spectrum. So, we went on to the next method and assumed that the lattice oxygen peak moved to the higher binding energy following the defect creation and fill most of the area of the sputtered O $1s$ spectrum.

Figure 4.2 shows a different approach of O $1s$ XPS peak fitting following the $Ar^+$ ion sputtering as a function of sputtering energy and time. The peak located at the 530.15 eV is attributed to the lattice oxygen and the feature located at the 531 eV is due to the oxygen vacancy. A third peak is added at 532.6 eV binding energy corresponds to oxygen vacancy to obtain satisfactory peak fitting for the sputtering time 2, 4 and 8 minutes respectively. These vacancy peaks correspond to the removal of two different types of oxygen: two-fold oxygen (bridging oxygen) and three-fold oxygen (the oxygen through which six-fold and five-fold titanium atoms are bonded together) (the structure of the titanium dioxide surface is shown in chapter 3, Figure 3.1). The $Ti^{3+}$ and $T^{2+}$ intermediate oxidation states are due to the removal of bridging oxygen, whereas $Ti^{1+}$ is due to the removal of three-fold oxygen and two-fold oxygen. So, the second defect peak is expected at higher binding energy due to the removal of three-fold oxygen, however, there may be an overlap between these peaks of oxygen near oxygen vacancies. The quantitative analysis of defect creation in O $1s$ spectra is found to be relatively consistent with the defect creation in Ti $2p$ spectra. This approach seems to be the most suitable, thus we will use it from now on.

### 4.3.2 Exposure to water, oxygen and ambient pressure

Figure 4.3 shows Ti $2p$ XPS of sputtered, 0.2 mbar water exposed, 1 mbar oxygen exposed, 5 mbar air exposed, ambient pressure exposed and annealed

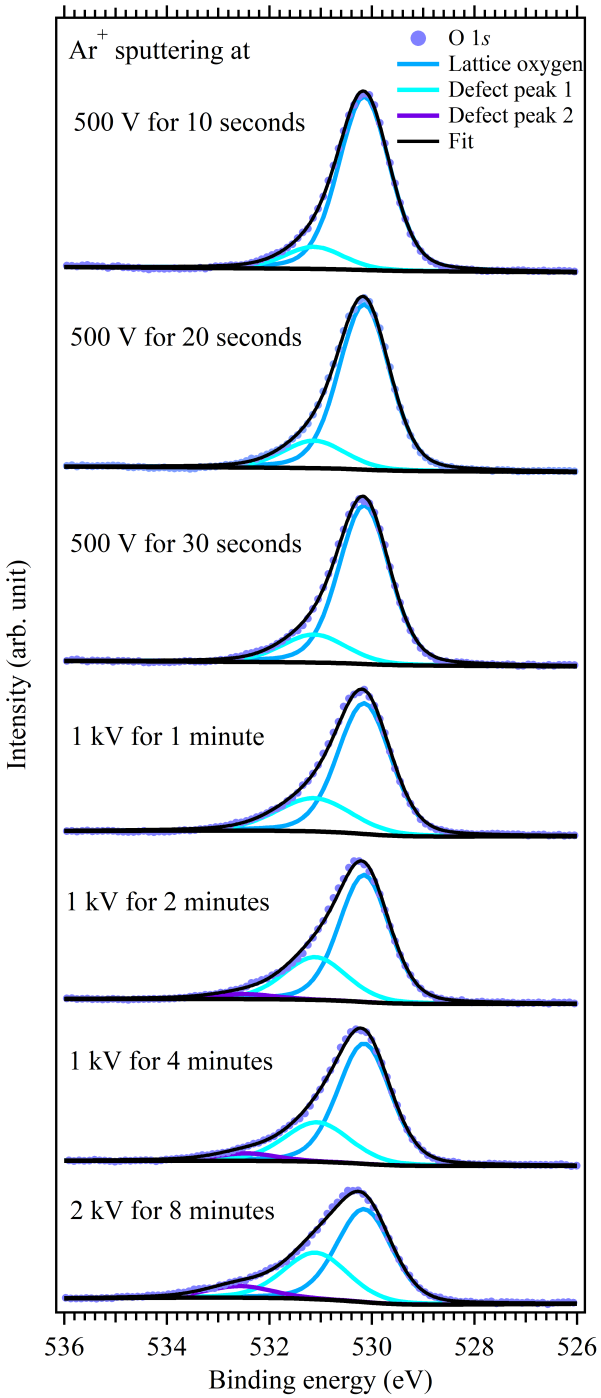



**Figure 4.2:** *O 1s XPS spectra consisting peak fitting to demonstrates the change of intensity of the lattice oxygen and oxygen vacancies. Defective surface created by $Ar^+$ sputtering at* 500 V *for 10, 20, 30 seconds, at* 1 keV *for 1 , 2, 4 minutes and at* 2 keV *for 8 minutes respectively. All surfaces measured at normal emission (NE).*

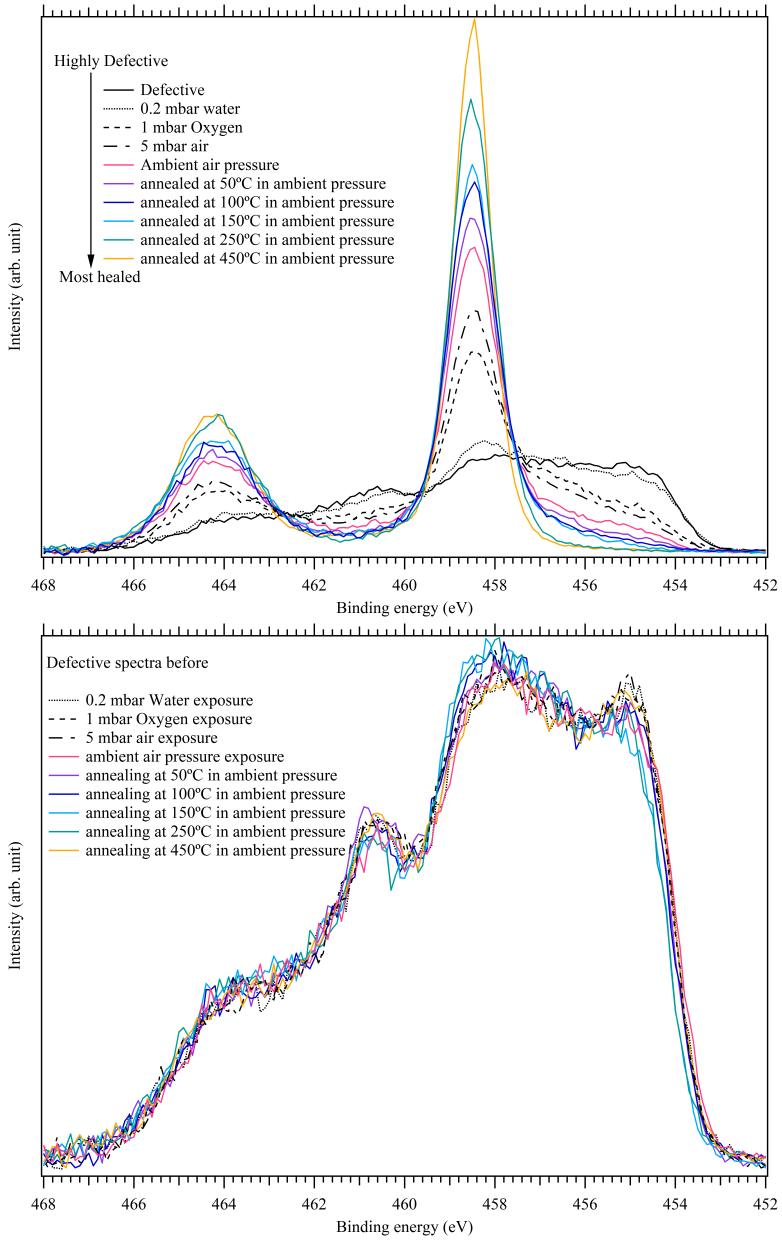



**Figure 4.3:** *Top: Ti 2p XPS measurements of 'defective' surface prepared by $Ar^+$ sputtering and 'water exposed', 'oxygen exposed', 'air exposed' and surfaces taken after heating the defective surfaces at five different temperatures (323 ,373 ,423 ,523 and 723 K) in ambient pressure respectively. Bottom: Ti 2p XPS measurements of defective state of surfaces created by $Ar^+$ sputtering, before healing the surface defect using, water, oxygen, controlled air and heating in ambient pressure. All surfaces measured at normal emission (NE).*

surfaces in ambient pressure at 323 , 373 , 423 , 523 and 723 K for one hour of rutile $TiO_2$(110) respectively. Before being exposed to different molecules or heat treatment in ambient pressure, the sample was sputtered and annealed to restore a clean surface and then the defective surface was prepared by $Ar^+$ ion sputtering at 2 keV for 10 minutes.

To investigate the changes in defects intensity after exposure to water, oxygen, air and annealed surfaces at various temperatures in ambient pressure, an almost identical defective surface was created before each exposure. Figure 4.3 (bottom) shows Ti 2*p* spectra of the sputtered sample before each exposure to different molecules and ambient pressure at different temperatures, which confirms the near identical defective state of the sample.

The XPS measurements were taken after exposing the sample to the molecules and ambient pressure in two different experimental setups. The first set of XPS measurements was carried out in the NAP-cell without breaking any vacuum where the sputtered sample was exposed to 0.2 mbar water (which is 4 % of 5 mbar air) and 1 mbar oxygen (which is 20.95 % of 5 mbar air) and 5 mbar air respectively for one hour. XPS measurements of the second set were performed after the sputtered sample was removed from the UHV and subjected to the ambient pressure at room temperature, 323 ,373 ,423 ,523 and 723 K respectively for one hour.

Ti 2*p* XPS spectra shown in Figure 4.3 are peak fitted and presented in Figure 4.4 to determine the spectral contribution of the different Ti oxidation states. As shown in figure 4.4, the intensity of the lower Ti oxidation states has decreased and continues to decrease in order of the exposure to water, oxygen, air, ambient pressure and annealing in ambient pressure. The $Ti^+$ shoulder in the Ti 2*p* peak is readily quenched at and above 423 K, whereas the $Ti^{2+}$ shoulder diminished after annealing at 523 K in ambient pressure. A small trace of $Ti^{3+}$ oxidation state was still observed after annealing at 723 K temperature in ambient pressure.

Figure 4.5 quantitatively shows how the relative concentration of the

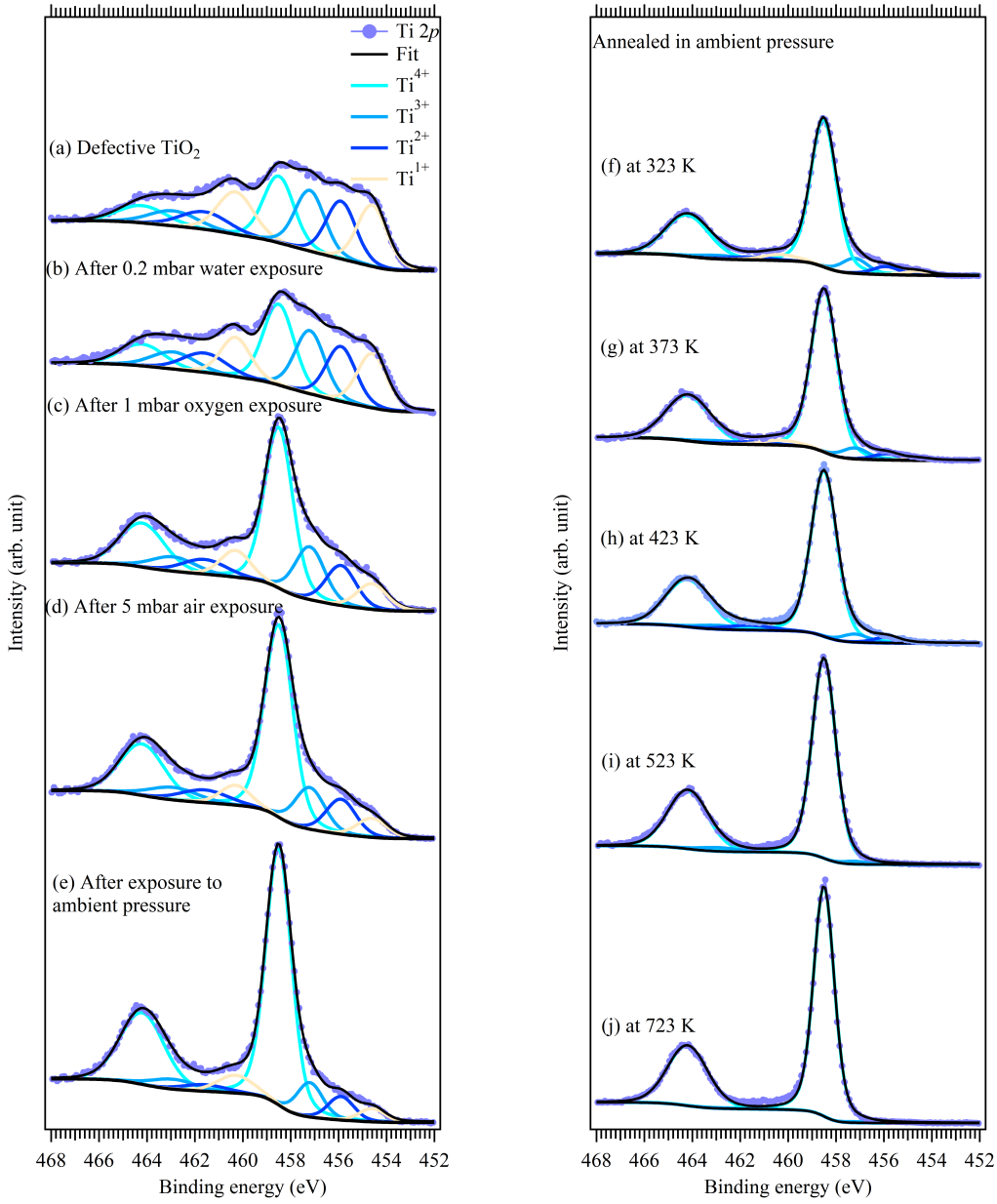



**Figure 4.4:** *Ti 2p XPS spectra consisting peak fitting to demonstrates the change of intensity of the Ti oxidation states. The first spectrum corresponds to (a) defective surface created by $Ar^+$ sputtering and rest of the spectrum corresponds to (b)* 0.2 mbar *water exposed (c)* 1 mbar *oxygen exposed (d)* 5 mbar *air exposed (e) ambient pressure exposed at room temperature (f) at* 323 , *(g)* 373 , *(h)* 423 , *(i)* 523 and *(j)* 723 K *respectively. All surfaces measured at normal emission (NE).*

different titanium oxidation states changes during exposure to different molecules in UHV and heating at five different temperatures in ambient pressure. Upon exposure to water $Ti^{2+}$ and $Ti^{1+}$ decreases whereas $Ti^{4+}$ increases. The $Ti^{3+}$ remains constant. This could be due to the filling of the oxygen vacancy site and the neighbouring bridging oxygen site by two identical OH produced from water dissociation. The oxygen exposed surfaces shows further decrease of $Ti^{3+}$, $Ti^{2+}$ and $Ti^{1+}$ at similar rate while $Ti^{4+}$ increases proportionally. This might be due to the oxygen dissociation at oxygen vacancy which results in progressive progression of $Ti^{1+} \rightarrow Ti^{2+} \rightarrow Ti^{3+} \rightarrow Ti^{4+}$ conversions. Further diminution of lower Ti oxidation state and increase of $Ti^{4+}$ upon exposure to 5 mbar air and ambient pressure is the combined effect of oxygen and water dissociation near the oxygen vacancy site. The intermediate Ti oxidation states continue to decrease with increasing annealing temperature in ambient pressure where the concentration of $Ti^{1+}$ and $Ti^{2+}$ reached 0% after annealing at 723 K. This depletion of the intermediate Ti oxidation state during annealing is more likely due to the bulk assisted oxidation through titanium interstitial and oxygen vacancy diffusion mechanism.

The O $1s$ spectra presented in Figure 4.6 are peak fitted to investigate the spectral contribution of the fit component after exposure to the water, oxygen, air molecules and ambient pressure at different temperatures. 'Defective' and 'water exposed' spectrum fitted with three and five peaks respectively. The 'oxygen exposed' and '5 mbar air exposed' O $1s$ spectra fitted with four peaks. 'Ambient pressure exposed' O $1s$ spectra at room temperature, 323 , 373 , 423 , and 523 temperatures are fitted with three peak. As discussed before (shown in Figure 4.2), The O $1s$ spectra are peak fitted considering that the lattice oxygen moves to higher binding energy following the creation of defect and moves to the lower binding energy as the defect concentration decreases. The movement of lattice oxygen is induced by the charge imbalance caused by the removal of a neutral oxygen atom. When a neutral oxygen atom is removed, two electrons are left behind, and both the neighbouring five-fold and six-fold

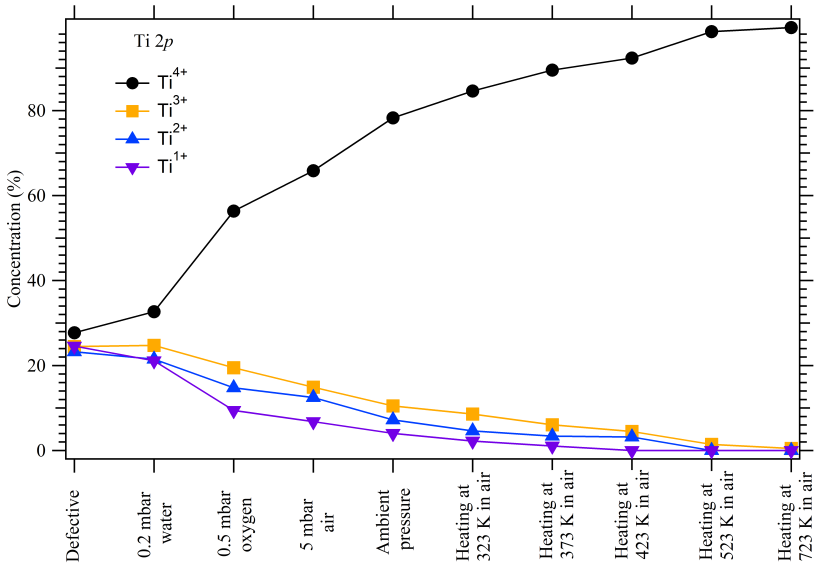



**Figure 4.5:** *Defect concentration of the different titanium oxidation states, extracted from peak fitting of Ti 2p XPS data (example in Figure 4.3) changes from defective surface during exposure to water, oxygen, air and heating at five different temperature in ambient pressure.*

titanium atoms receive an unpaired electron. So, the effective charge of oxygen vacancy became positive and due to electrostatic attraction, the $O^{-2}$ ions on the vertical plane moved toward the peak associated with oxygen near oxygen vacancies. After absorption of oxygen, this electrostatic charge diminishes and the lattice oxygen moves to the lower binding energy [115]. In a highly defective surface, the lattice oxygen located at 530.25 eV binding energy and the position of the lattice oxygen peak is found at 530.05 eV after annealing at 723 K temperature in ambient pressure.

In the O 1*s* spectrum for a highly defective surface, the features located at 531 and 532.6 eV correspond to oxygen vacancies. The feature located at 531.55 eV in the higher binding energy in the O 1*s* spectra corresponds to the adsorbed hydroxide. Absorbed water feature solely observed for the water exposed surface located at 533.2 eV. The relative positions of these features are consistent with previous study rutile $TiO_2$(110), where the hydroxyl peak located at 1.1 −1.6 eV and adsorbed water peak located at 2.4 −3.4 eV in the higher binding energy relative to the lattice oxygen [43, 81]. The immediate

loss of the intensity of the oxygen vacancies was observed after water exposure, which remains comparable with 'oxygen exposed', '5 mbar air exposed' and 'ambient pressure exposed' surface at room temperature. Then a slight increase of intensity is observed after heating at 323 K in ambient pressure after that the intensity of peak associated with oxygen near oxygen vacancies remains almost constant for the surfaces heated at 373 , 423 , 523 and 723 K. The O $1s$ spectrum after 0.2 mbar water exposure results in immediate loss of the intensity of the peak associated with oxygen near oxygen vacancies and the presence of hydroxyl group (OH), and adsorbed water. After exposure to oxygen molecules the defects intensity decreases significantly. Highly reactive oxygen vacancy sites of $TiO_2$ surfaces are expected to react with oxygen to decrease oxygen vacancy defects. The effect of 5 mbar exposure to defective surface results in similar healing of surface compared to exposure to oxygen. In theory 5 mbar air contains 0.2 mbar water (which is 4 % of 5 mbar air) and 1 mbar oxygen (which is 20.95 % of 5 mbar air). Defect peak 2 diminishes after exposure to ambient pressure and defect peak 1 continues to decrease as a function of increasing annealing temperature in ambient temperature.

The highest intensity of the OH peak is observed for water exposed O $1s$ XPS and decreases for exposure to oxygen and 5 mbar respectively. The intensity of OH remains almost constant during annealing in ambient pressure up to 523 K. After annealing at 723 K temperature in ambient pressure, the OH is started to desorb.

The immediate loss of the intensity of the peak associated with oxygen near oxygen vacancies can be explained according to the previous study showing that oxygen vacancies work as water nucleation sites and heal the defects.

Oxygen exposure to defective $TiO_2$ surface leads to the filling of an oxygen vacancy and an oxygen adatom. According to the TPD study of water and oxygen exposure to $TiO_2$, oxygen dissociation on the vacancy site leads to the formation of a weak hydrogen-bonding interaction between oxygen adatom at a five-coordinated $Ti^{4+}$ site and water adsorption at neighbouring $Ti^{4+}$ site

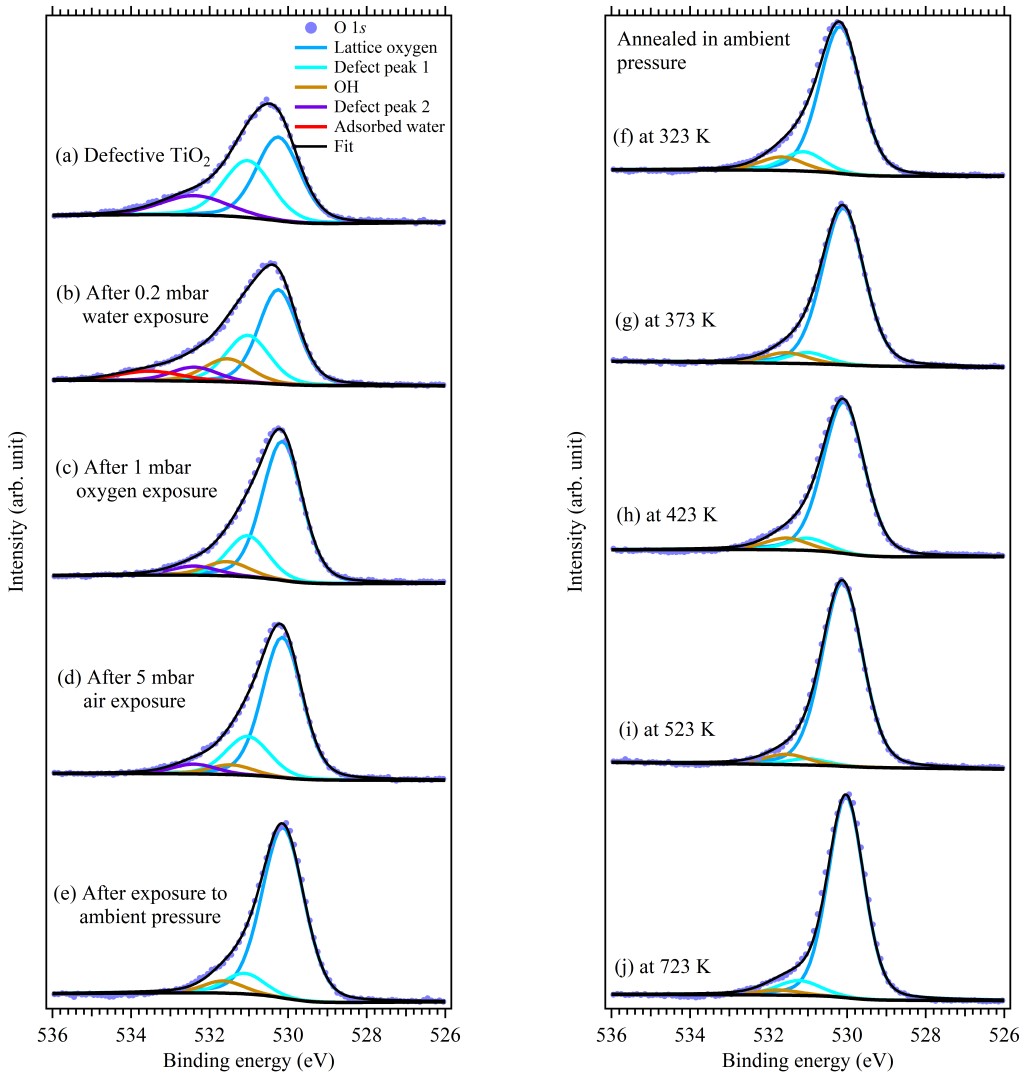



**Figure 4.6:** *O 1s XPS spectra consisting peak fitting to demonstrates the change of intensity of the lattice oxygen, oxygen vacancy, hydroxyl group, carboxyl group and adsorbed water. The first spectrum corresponds to (a) defective surface created by* $Ar^+$ *sputtering and rest of the spectrum corresponds to (b)* 0.2 mbar *water exposed (c)* 1 mbar *oxygen exposed (d)* 5 mbar *air exposed (e) ambient pressure exposed at room temperature (f) at* 323 , *(g)* 373 , *(h)* 423 , *(i)* 523 a*nd (j)* 723 K *respectively. All surfaces measured at normal emission (NE).*

due to very short distance (less than 3 Å). Then as a result of a proton transfer from the water molecule to the oxygen adatom leads to the formation of two identical hydroxyl groups [116, 117]. Hence, under ambient pressure defective surface has an abundant proportion of oxygen and water to dissociate in the catalytically active sites and resulting in the healing of the oxygen vacancies of the defective surfaces.

## 4.4 Summary and Conclusions

Defective rutile $TiO_2$(110) surfaces were exposed to 0.2 mbar water, 1 mbar oxygen, 5 mbar air, ambient pressure at room temperature, 323 , 373 , 423 , 573 , and 723 K respectively. Defective surfaces were prepared using $Ar^+$ sputtering before each exposure to investigate the effect of the corresponding exposed molecules. Before exposure to ambient pressure, at first 0.2 mbar water, 1 mbar oxygen and 5 mbar were exposed to the defective surface. For consistency, 4 % water and 20.95 % oxygen of 5 mbar air were exposed. The intensity of the oxygen vacancy gradually decreased upon exposure to water, oxygen, air and ambient pressure. During water exposure defects heal by water dissociation whereas during oxygen exposure oxygen dissociates into an oxygen atom and oxygen adatom, where the oxygen atom fills the vacancy and the oxygen adatom dissociates further water and produces two identical OH groups. Upon exposure to ambient pressure, further depletion of the defect was observed. A rapid depletion of the Ti intermediate oxidation state was observed during annealing as a function of increasing temperature in ambient pressure. This is more likely due to the progressive conversion of $Ti^{1+}$ defects to $Ti^{4+}$ via intermediate oxidation states by bulk assistance oxidation mechanism through titanium interstitial and oxygen vacancy diffusion mechanism. The interaction of air molecules with oxygen vacancies is considered extremely important for technological application. The presence of oxygen vacancies after exposure to ambient pressure at higher temperatures in rutile $TiO_2$(110) could lead to a

valuable candidate for the application as an ambient pressure catalyst.

# Chapter 5

# Ultra fast charge transfer dynamics of bi-isonicotinic acid on rutile, anatase and mesoporous $TiO_2$

## 5.1 Introduction

The search for a combination of suitable dye molecules and semiconductor substrates to achieve high efficiency dye sensitized solar cells is still an ongoing process. Recent advancement in the charge transfer time estimation technique in femto second (fs) time scale from dye molecules to the substrate has created a more accurate way of investigating charge transfer dynamics [21]. So far the charge transfer dynamics for N3 (cis-bis(isothiocyanato)bis(2,2'-bipyridyl-4,4'-dicarboxylato)-ruthenium(II)), isonicotinic acid, Bi-isonicotinic acid, WSC  CISC, two ruthenium based dye complexes containing dipyrrin and multicenter water splitting dye adsorbed on rutile $TiO_2$(110) has been investigated [11, 18, 21, 23, 26, 32, 118–120]. Charge transfer dynamics also implemented on bi-isonicotinic acid on anatase $TiO_2$ nanoparticle [15]. The charge transfer dynamics also depend on the structure and bonding geometry

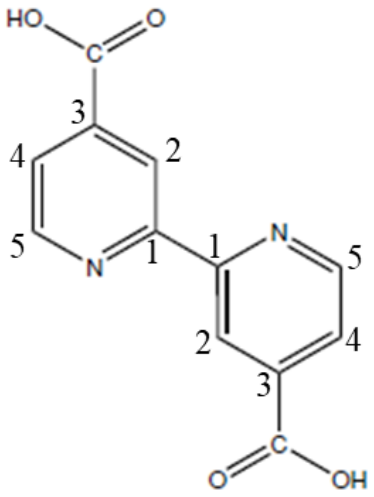



**Figure 5.1:** *The chemical structure of bi-isonicotinic acid. To point out two different types of carbon binding energy, the carbon atoms in the pyridine ring which are the direct neighbour of the nitrogen atom are numbered as pyridine carbon (1, 5) and the remaining carbon atoms in the pyridine rings are numbered as pyridine carbon (2, 3, 4).*

of the dye molecules with the substrate. Hence, the structure and bonding geometry of chemisorbed bi-isonicotinic acid on rutile and anatase $TiO_2$ has been investigated in depth [12, 13, 22]. To our knowledge, implementation of charge transfer dynamics has not yet been performed on chemisorbed bi-isonicotinic acid on anatase $TiO_2$(101) single crystal and mesoporous $TiO_2$.

In this experiment, X-ray photoelectron spectroscopy (XPS), X-ray absorption spectroscopy (XAS) and resonant photoemission spectroscopy (RPES) data have been measured for the bi-isonicotinic acid on rutile, anatase and mesoporous $TiO_2$ systems. Then the charge transfer time was obtained by core-hole clock implementation using RPES and XAS data for these systems. we are repeating charge transfer (CT) time calculation for rutile. The reason is to compare the CT directly using the same beamline to keep everything as consistent as possible and to observe any differences between the different substrates.

## 5.2 Methods

The experiments were performed at the surface and material science end station at the FlexPES beamline situated on the 1 GeV storage ring at the MAX IV synchrotron facility in Sweden. The experimental station is equipped with a planar undulator and collimated plane grating monochromator and a Scienta SES-2002 hemispherical analyzer for photoelectron spectroscopy (PES), positioned at an angle of 40 ° from the incident photon beam. The monochromator can be focused to a $65 \times 10\,\mu m$. Measurements were taken at normal emission.

The rutile $TiO_2(110)$ and anatase $TiO_2(101)$ single crystal (obtained from PI-Kem, UK) surfaces were prepared by cycles of sputtering using 2 KeV and 1 KeV $Ar^+$ ions and annealing in UHV to ∼600 °C. Bi-isonicotinic acid (obtained from Sigma-Aldrich, UK) was outgassed thoroughly in a thermal sublimation stage, which was equipped with a separate turbomolecular pump and pressure and temperature monitors. The sublimation stage was connected to the main chamber via a manual valve and the sublimation stage could be brought closure to the sample for sublimation. For monolayer preparation on rutile and anatase $TiO_2$, the bi-isonicotinic acid powder was evaporated at 290 °C temperature and the sample temperature was held on 220 °C, allowing the physisorbed multilayer to desorb and leaving only the chemisorbed monolayer. For multilayer preparation, the sample was kept at room temperature. The mesoporous $TiO_2$ on fluoride-doped tin oxide (FTO) coated glass was obtained from Solaronix, Switzerland. For monolayer coverage of bi-isonicotinic acid on mesoporous $TiO_2$ preparation (schematic diagram of the ex-situ preparation technique is presented in Figure 2.1), the sample was left in a small beaker of iso-propanol in a large beaker of iso-propanol together with another small beaker containing a small amount of bi-isonicotinic acid powder. Over the course of a week, the bi-isonicotinic acid adsorbs onto the mesoporous $TiO_2$. The bi-isonicotinic acid beaker is then removed and the iso-propanol is replaced in the large beaker with clean iso-propanol, and then a fresh meso-

porous $TiO_2$ sample is added to scavenge any excess bi-isonicotinic acid. This process is repeated several times to ensure that all physisorbed bi-isonicotinic acid is removed from the sample.

The binding energy scales were calibrated by setting the lattice oxygen peak in O 1$s$ to 530.05 eV using X-ray photoelectron spectroscopy (XPS) [27]. XPS spectra and the valance band spectra were measured at h$\nu$ = 600 eV and h$\nu$ = 350 eV respectively. XPS data were peak fitted using a pseudo-Voigt function allowing a fixed Lorentzian width (0.3 eV) and variable Gaussian width following the subtractions of a Shirley background.

## 5.3 Results and Discussion

### 5.3.1 Bi-isonicotinic acid / rutile $TiO_2$(110)

#### XPS

Figure 5.2 shows the O 1$s$ XPS spectra of the monolayer and multilayer coverage of bi-isonicotinic acid on $TiO_2$(110) surface. The adsorption mechanism of bi-isonicotinic acid to the $TiO_2$ surface can be understood by comparing the monolayer film with the multilayer film. In monolayer film, molecules can interact with the surface by adopting a 2M-bidentate bonding geometry [12], whereas multilayer film consists of many layers of physisorbed bi-isonicotinic acid effectively isolated from the surface of the substrate. This is evident by the near absence of the oxide peak in the spectrum of the multilayer. The monolayer data as shown in Figure 5.2(a) presents three peaks at 530.05 , 531.7 and 533.5 eV. These peaks are attributed to the lattice oxygen of the substrate, the deprotonated carboxylate and hydroxyl (OH) groups respectively. As shown in Figure 5.2(b), multilayer XPS fitted with two overlapping peak at 532.4 and 533.6 eV. These peaks correspond to the oxygen atoms in the carbonyl (C=O) and hydroxyl (OH) groups from the carboxylic acid group of the molecule respectively. In multilayers, molecules are isolated from the

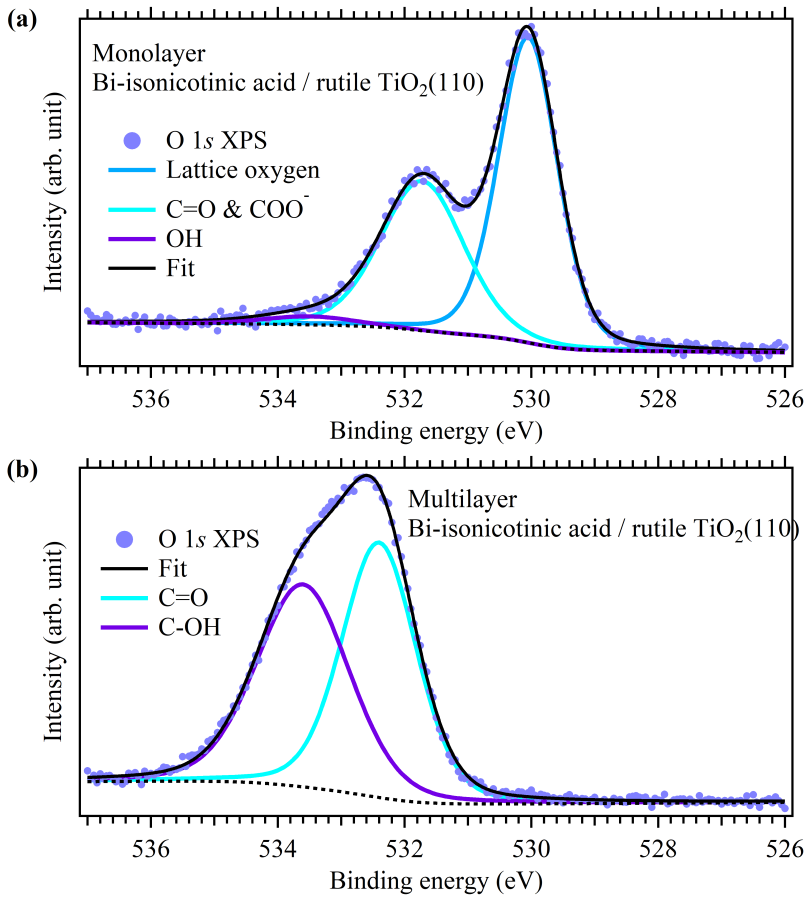



**Figure 5.2:** *O 1s XPS spectra of (a) monolayer and (b) multilayer coverage of bi-isonicotinic acid on rutile $TiO_2$(110). Black dotted line corresponds to Shirley background. Both spectra were measured at normal emission (NE) using a photon energy of* 600 eV.

surface, so two equally intense peaks of hydroxyl (C-OH) and carbonyl (C=O) are expected to be consistent with the stoichiometry of the molecule. The ratio of the area of these two peaks is found to be 1:1 as expected.

The presence of a non-deprotonated carboxylic acid derived peak is too weak to indicate the formation of any second layer of molecules. However the strong presence of deprotonated carboxyl groups is evidence of both chemically equivalent oxygen atoms of each carboxyl group are involved in bonding to the surface. Although it is expected to see two peaks in the O 1*s* XPS, attributed to C=O and C-O$^-$ when all the carboxylic acid are deprotonated but in reality, we observe only one peak at the C=O peak position because these two chemical groups are indistinguishable in O 1*s* XPS [24, 28, 121]. A clear shift of the deprotonated carboxylate acid feature in the lower binding energy by 0.7 eV is

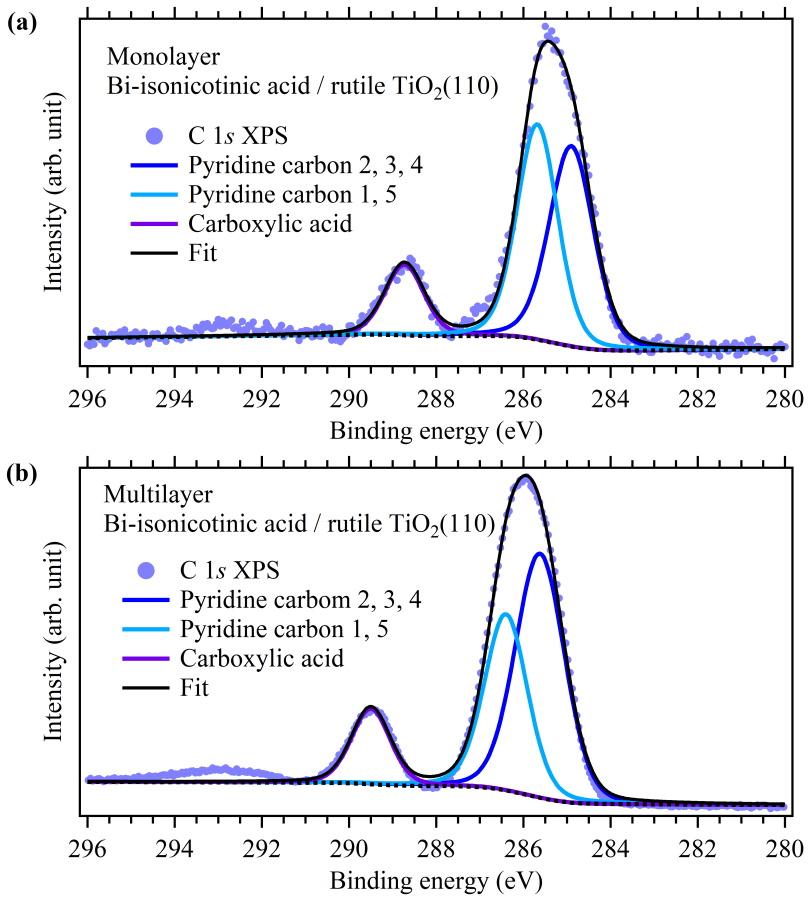



**Figure 5.3:** *C 1s XPS spectra for (a) monolayer and (b) multilayer film of bi-isocotinic acid on rutile $TiO_2$(110). Black dotted line corresponds to Shirley background. Both spectra were measured at normal emission (NE) using a photon energy of* 600 eV.

observed for monolayer film.

Figure 5.3 shows the C 1*s* XPS spectra of monolayer and multilayer coverage of bi-isonicotinic acid on $TiO_2$(110). In the monolayer spectrum, the lower binding energy peak is attributed to the carbon atoms in the pyridine ring, and the higher binding energy peak is located at 288.8 eV to the carboxylic group. A low intensity peak is also visible at 293 eV attributed to the shake-up feature. The shape of the pyridine ring peak is due to the emission from two different types of carbon binding energy. The higher binding energy side of the peak is due to the emission from the carbon atoms which are the direct neighbour of the nitrogen atom (Pyridine carbon (1, 5) peak located at 285.7 eV and the lower binding energy side is attributed to the remaining carbon atoms of the pyridine ring (Pyridine carbon (2, 3, 4) peak located at

284.9 eV). The multilayer spectrum also consists of a pyridine carbon peak in the lower binding energy side and the pyridine carbon (2, 3, 4) and pyridine carbon (1, 5) peaks are located at 284.6 eV and 285.4 eV, respectively. The peaks located at 289.5 eV and 293 eV are corresponding to the carboxylic acid group and shake-up features. The position of the peaks is consistent with previous studies of bi-isonicotinic acid on rutile $TiO_2$ [27]. From peak fitting, The obtained ratio of the pyridine carbon (2, 3, 4) : pyridine carbon (1, 5) : carboxylic acid is found to be 3 : 2: 1, which is consistent with the chemical structure of bi-isonicotinic acid molecules. The intense intensity of the peak associated with the pyridine carbon (1, 5) compares to the peak associated with the pyridine carbon (2, 3, 4) in monolayer coverage, perhaps because bi-isonicotinic acid molecules are bonded to the substrate through a deprotonated carboxylic group and stood upright on the surface. Therefore, we preferentially see the less intense feature of the pyridine carbon (2,3,4), which is shadowed by the rest of the molecules. In multilayer coverage, the molecules are isolated from the substrate, and the orientation of the molecules is random. So, for multilayer coverage, the ratio of pyridine carbon (2, 3, 4) to pyridine carbon (1, 5) is expected to be 3 : 2.

From the C 1$s$ XPS of monolayer coverage, a shift of 0.7 eV is observed for carboxylic acid, which is consistent with the 0.7 eV shift of carboxylic acid in O 1$s$. Whilst, 0.55 eV shift in the lower binding energy is observed for the pyridine carbon. This kind of shift towards the lower binding energy for monolayer is generally observed in comparison to multilayer coverage. The most probable reason is the screening of the core-hole by the highly polarisable substrate. This can also change the separation of the peaks because the carboxyl groups are attached to the surface by two highly oriented substrate bonds while the ring might not as it is not attached [27]. In the multilayer, there also have the possibility of steady state charging due to the insulating nature of the molecules and this can both broaden the peaks and shift them to the higher binding energy.

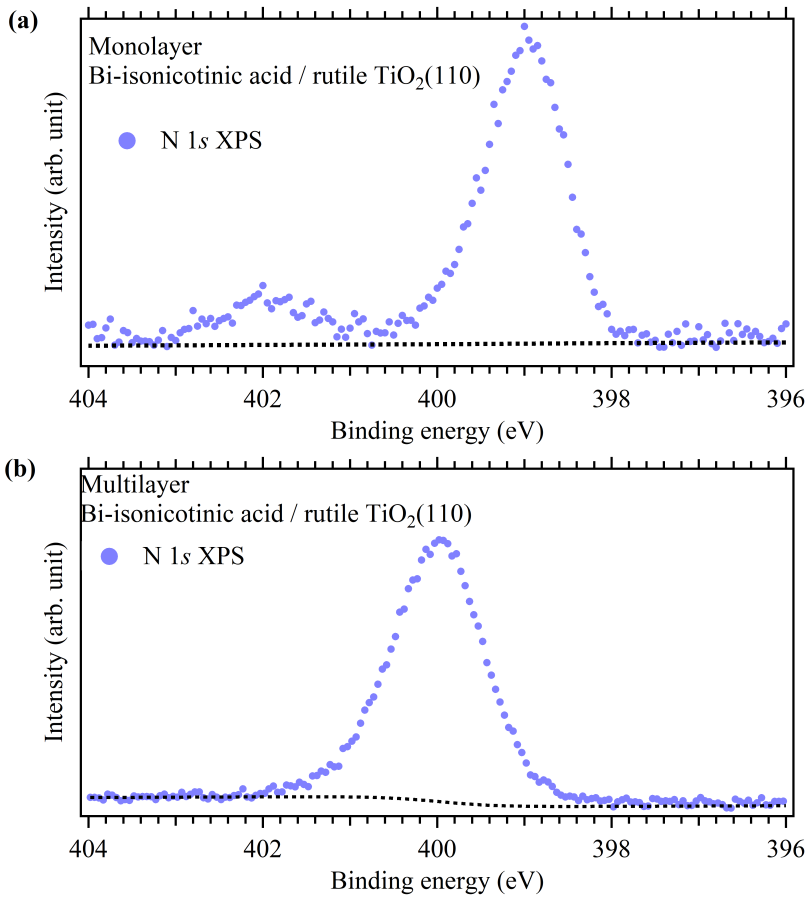



**Figure 5.4:** *N 1s XPS spectra(a) monolayer and (b) multilayer film of bi-isocotinic acid on rutile $TiO_2$(110). Black dotted line corresponds to Shirley background. Both spectra were measured at normal emission (NE) using a photon energy of* 600 eV.

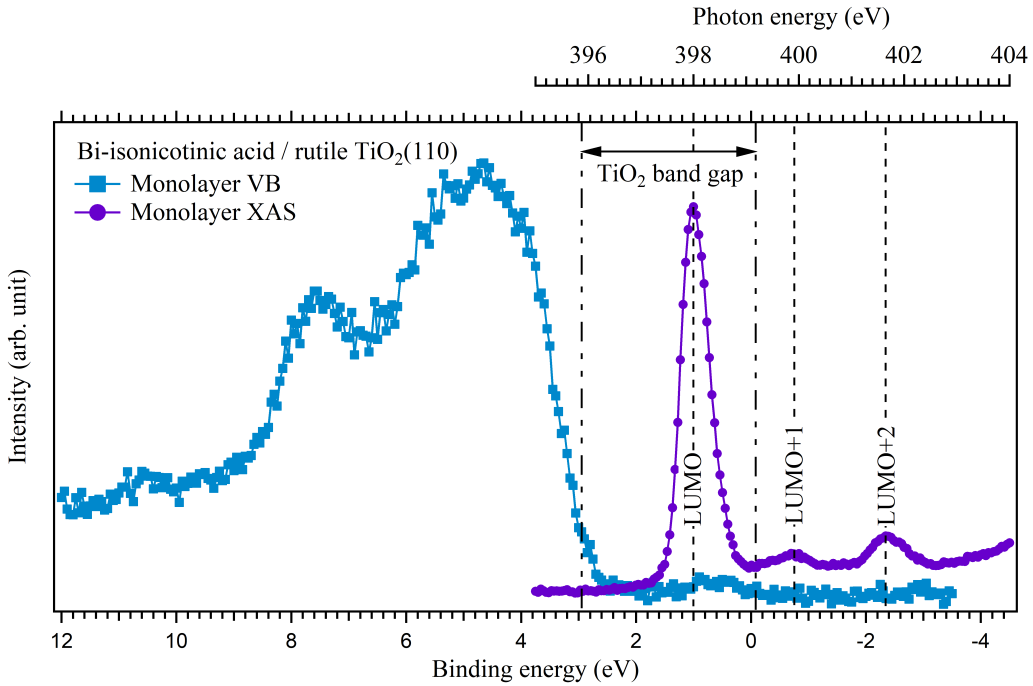



**Figure 5.5:** *Density of states plot of monolayer of bi-isonicotinic acid on rutile $TiO_2$(110). The purple line shows an X-ray absorption spectrum (measured over the N 1s absorption edge) showing unoccupied states placed on a common binding energy scale with the blue line shows the valance spectrum of the monolayer measured by photoemission spectroscopy with a photon energy of* 350 eV. *All spectra were measured at normal emission.*

N 1*s* XPS spectra are shown in Figure 5.4 for the monolayer and multilayer. Nitrogen peak for monolayer and multilayer located at 399 and 400 eV respectively. A shake-up feature is observed at ∼402 eV in the higher binding energy of monolayer film. According to the previous study, this is related to the chemisorption on the $TiO_2$ surfaces, since it is not found for the multilayer [27]. One plausible explanation is that this peak is related to a shake-up that involves the carboxylic group and that effectively results in a final state in which the additional positive charge from the photoionisation process has been moved to the carboxylic group/substrate complex in the shake-up process [27]. A shift of 1 eV is observed for N 1*s* peak in monolayer, which is higher than the shift observed for O 1*s* and C 1*s* in monolayer. N 1*s* peak might be more affected by steady state charge due to the insulating nature of the molecules in the multilayer.

### Density of states

To understand the charge transfer dynamics in either direction, it is important to have knowledge of the energetics of the lowest unoccupied molecular orbitals of the molecules with respect to the substrate density of states. The charge transfer is only possible if the substrate density of states matches that of the adsorbate. Figure 5.5 shows a combination of valance photoemission spectra and an X-ray absorption spectrum (XAS) for a monolayer of bi-isonicotinic acid on $TiO_2$(110). The spectra have been presented on a common binding energy scale. The peaks in the XAS at Binding energy, BE≈1 eV, BE≈−0.1 eV and BE≈ −2.5 eV are attributed to the LUMO, LUMO+1 and LUMO+2 states of the core-excited molecules, respectively. It is clear from the Figure 5.5 that the LUMO (BE≈1 eV), lies entirely within the substrate's band gap (Band gap of rutile $TiO_2$ is 3 eV [122]). In theory, This would not allow the transfer of electrons from the valence band of $TiO_2$ for excitation to the LUMO. Whereas, the core excited LUMO+1 and LUMO+2 overlap with unoccupied states in the substrate. So, charge transfer to these higher resonances from the substrate is possible.

### Resonant photoemission

The N 1*s* resonant photoemission (RPES) data for monolayer and multilayer coverage of bi-isonicotinic acid on rutile $TiO_2$(110) surface are shown in Figure 5.6. The two dimensional plots represent the intensity of emitted valance photoelectrons as a function of incident photon energy and their measured binding energy. A number of interesting features identified for the monolayer film as shown in Figure 5.6(a) and a schematic diagram presenting possible decay mechanism for these features of interest are also presented in Figure 5.6(c). The horizontal dashed lines represent the regions of intensity attributed to excitation into the lowest unoccupied molecular orbital (LUMO) states, which appear at constant excitation energy. The intensity features for LUMO+1

are too weak and indistinguishable from the photon energy tail of LUMO. Hence, The LUMO+1 level is not marked. The monolayer RPES spectrum also shows constant kinetic energy features marked by diagonal dashed lines, disperse linearly through the RPES binding energy window as the photon energy is increased. These diagonal lines are attributed to the spectator and Auger decay channels.

The intense peak situated on LUMO (398.5 eV photon energy) located at 5 eV binding energy is due to the participator decay (marked as I). In this mechanism, the originally photo-excited electron participates in the core-hole decay process and another electron from the highest occupied molecular orbital (HOMO) is emitted. On the other hand for spectator decay, the photoexcited electron does not participate in the relaxation of the system into its final state within the lifetime of the core-hole. Electrons from occupied molecular orbitals participate in the Auger-like decay process where one electron recombines with the core-hole and another is emitted into the vacuum (marked as II and III respectively). The kinetic energy of these electrons is constant and lower than the participator electrons by at least the HOMO-LUMO gap. The schematic of the charge transfer mechanism and subsequent Auger decay is also presented in Figure 5.6(c), where a photoexcited electron in an unoccupied LUMO+1 or LUMO+2 state can charge transfer into the conduction band of the $TiO_2$ followed by Auger-like decay process where one electron recombines with the core-hole and another is emitted into the vacuum. As the LUMO lies within the substrate band gap, the charge transfer from LUMO to the substrate is not possible.

The measurement of the charge transfer dynamics from the molecule to the rutile titanium dioxide surface can be obtained by using the core-hole clock implementation of RPES data. We can estimate the timescale of the charge transfer dynamics by comparing the relative intensities of the participator channel to the XAS for both the monolayer and multilayer. XAS represents the full intensity of the unoccupied levels, whereas in RPES the unoccupied

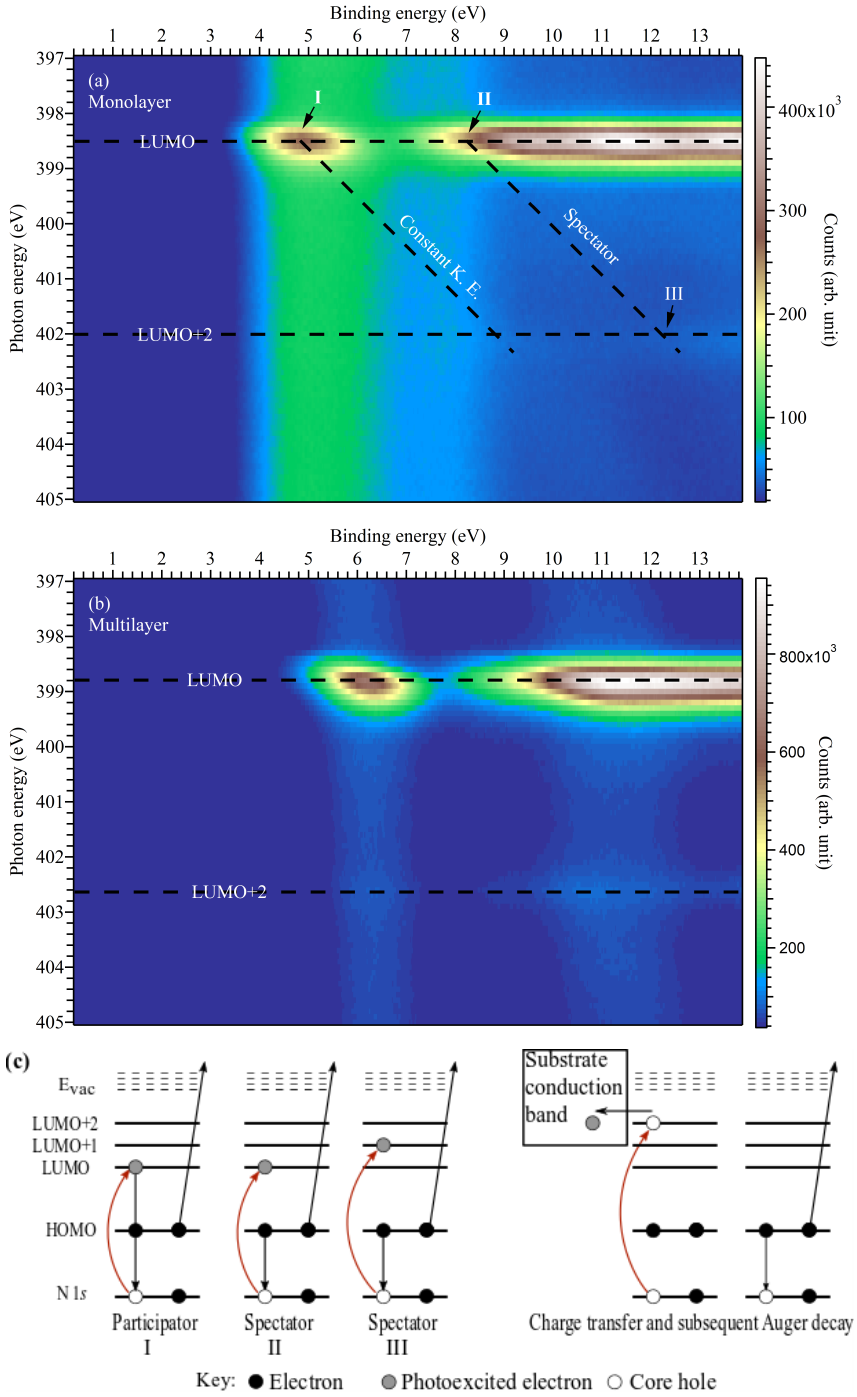



**Figure 5.6:** *Resonant photoemission spectra for (a) monolayer and (b) multilayer of bi-isonicotinic acid on rutile $TiO_2(110)$. The LUMO energy levels are indicated with horizontal dashed lines and diagonal lines highlight constant kinetic energy features. Figure (c) shows schematics of proposed decay mechanisms after excitation of an N 1s core electron. Both surfaces measured at normal emission (NE).*

states may be depleted by charge transfer from the molecule into the substrate. Charge transfer competes with the core-hole decay so to have an observable effect on the intensity of the participator channel it would need to be on the same timescale as the N 1$s$ core-hole lifetime. The participator channels of multilayer are entirely populated because the molecules are effectively isolated from the substrate and no charge transfer can take place. The depletion of the participator channel in the monolayer is therefore indicative of ultra-fast charge transfer to the surface on the time scale of the core-hole lifetime.

Integration of the participator electron intensity over the relevant binding energy window as a function of photon energy is shown for both the monolayer and multilayer in Figure 5.7 and compared to the associated X-ray absorption spectrum. Where the resonant photoemission spectra are normalised to the LUMO of the associated X-ray absorption spectrum. The LUMO lies entirely within the band gap, which in theory does not allow charge transfer from LUMO to the substrate. For multilayer, The LUMO+1 feature results from the orbital situated in the higher binding energy than the LUMO+2 orbital. Whereas for the monolayer, the LUMO+1 orbital is drawn down to a location between LUMO and LUMO+2 due to the strong interaction with the surface. It has been discussed thoroughly in a study for bi-isonicotinic acid on rutile titanium oxide [25]. So, the LUMO+2 of the multilayer serves as the benchmark for determining the charge transfer time for the LUMO+2 in the monolayer after the XAS and RPES have been normalised to the LUMO.

The charge transfer time for electron transfer out of a particular unoccupied molecular orbital can be calculated using

$$\tau_{El} = \tau_{CH} \frac{I^{mono}_{RPES}/I^{mono}_{XAS}}{I^{multi}_{RPES}/I^{multi}_{XAS} - I^{mono}_{RPES}/I^{mono}_{XAS}} \tag{5.1}$$

where the $I^{mono}_{RPES}/I^{mono}_{XAS}$ terms represent the relative intensities of the participator channel in the RPES as a fraction of the total X-ray absorption for the relevant molecular orbital given by XAS. $I^{multi}_{RPES}/I^{multi}_{XAS}$ term represents

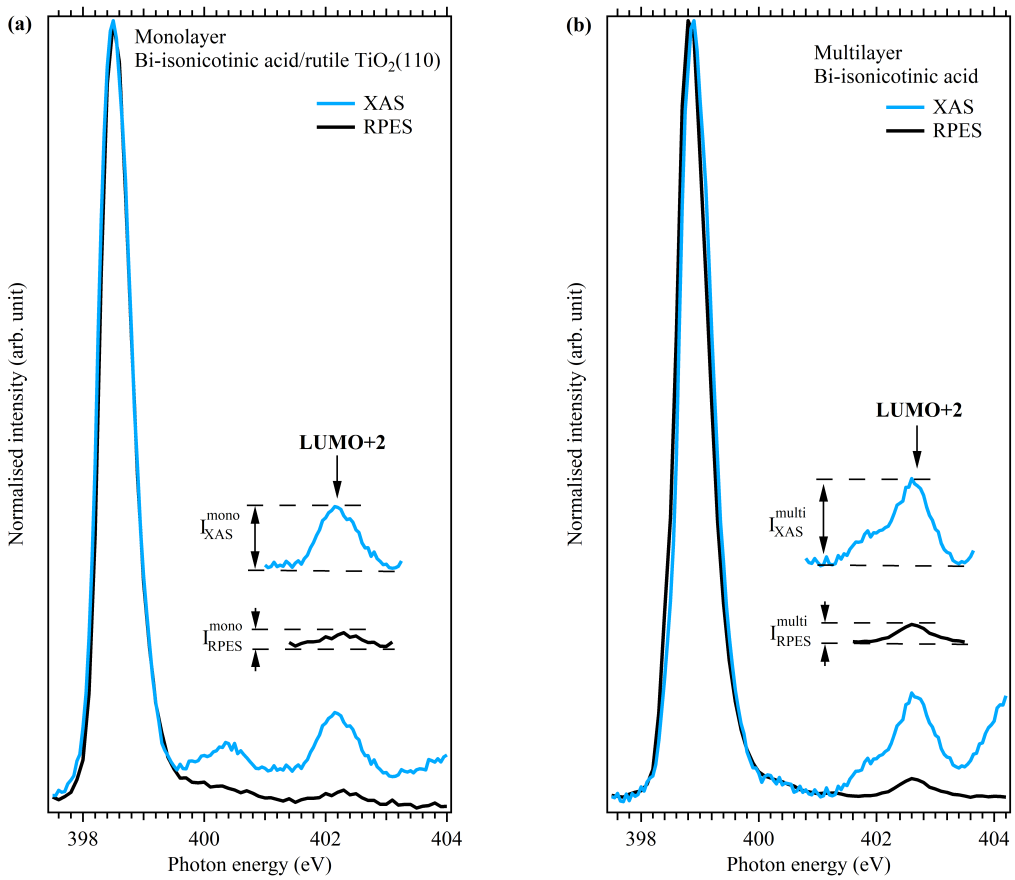



**Figure 5.7:** *N 1s RPES and N 1s XAS spectra of (a) monolayer and (b) multilayer bi-isonicotinic acid on rutile $TiO_2$(110). The RPES spectrum obtained by integrating participator (RPES) region of Figure 5.6.*

the fraction of participator electrons from decoupled molecules in the multilayer coverage. A derivation of the equation and complete core-hole clock implementation is discussed by Brühwiler et al. $\tau_{CH}$ is the average lifetime of an N 1$s$ core-hole that has been measured to be 6 fs. The $I^{mono}_{RPES}/I^{mono}_{XAS}$ and $I^{multi}_{RPES}/I^{multi}_{XAS}$ for the LUMO+2 is found to be 0.07 and 0.2 respectively. The charge transfer time from LUMO+2 to the conduction band of rutile $TiO_2$ is found to be $(3.2 \pm 0.2)$ fs. This is consistent with the charge transfer time estimated by others for bi-isonicotinic acid on rutile $TiO_2$(110) [21].

### 5.3.2 Bi-isonicotinic acid / anatase $TiO_2$(101)

#### XPS

O 1*s* XPS spectrum for the monolayer coverage of bi-isonicotinic acid on anatase $TiO_2$(101) surface is shown in Figure 5.8, measured using h$\nu$ = 600 eV. The dominating peak arising from the substrate located at 530.05 eV is attributed due to lattice oxygen. The peak located at higher binding energy at 531.5 eV is due to the carboxylic acid group. The presence of a single carboxylic acid peak indicates strong evidence for the formation of one layer of bi-isonicotinic acid contribution and adsorption of bi-isonicotinic acid on the surface via deprotonated carboxylic group where all four oxygen atoms in the molecules participate equivalently. A similar but moderately deformed surface binding ligand with two 2M-bidentate bonding geometry has been found in the previous study for anatase $TiO_2$ surface [13–15]. The deprotonated carboxylic group for monolayer coverage on anatase moved to the lower binding energy by 0.2 eV with compare to the monolayer on rutile. This arises due to the slightly deformed surface structure on anatase (101) compared to rutile, where the separation between two neighbouring fivefold coordinated Ti atoms is significantly smaller and Ti atoms in the two neighbouring rows are not placed directly opposite, instead shifted by half the Ti-Ti distance relative to each other. So, two deprotonated carboxylic acid groups bind diagonally with the 1.5 shifted Ti atoms on the two neighbouring fivefold coordinated Ti atom rows on the anatase surface [13].

Figure 5.9 shows C 1*s* XPS for the monolayer coverage of bi-isonicotinic acid on anatase $TiO_2$(101) surface. The pyridine carbon (2, 3, 4), pyridine carbon (1, 5) and carboxylic acid peak are located at 284.9 , 285.7 and 288.8 eV respectively. A shake-up feature is also found at the binding energy 293 eV. The observed intense intensity at the higher binding side of the pyridine ring is similar compared to the monolayer coverage on rutile. The carboxylic acid group and pyridine rings are shifted by 0.7 eV and 0.55 eV respectively com-

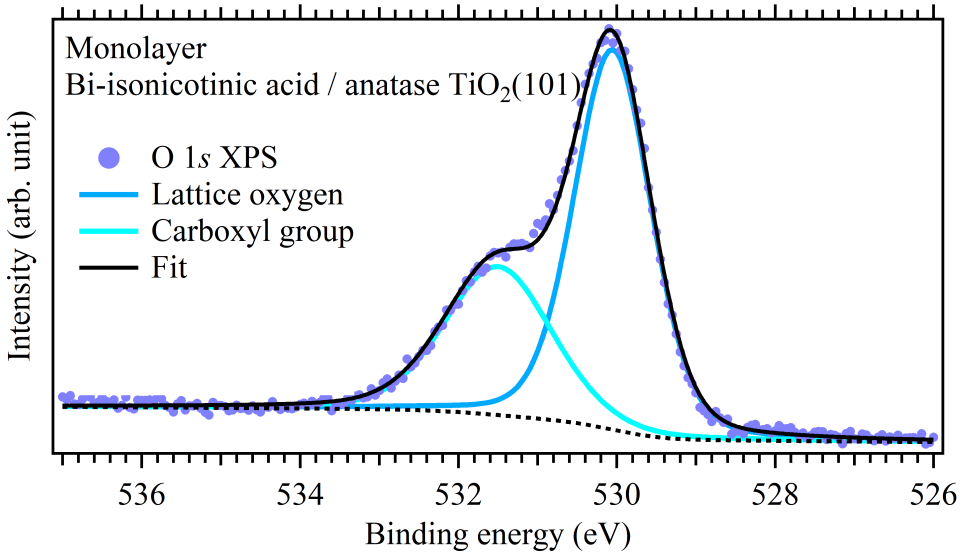



**Figure 5.8:** *O 1s XPS spectrum of monolayer coverage of bi-isonicotinic acid on anatase $TiO_2$(101). Black dotted line corresponds to Shirley background. XPS spectrum was measured at normal emission (NE) using a photon energy of* 600 eV.

pared to the multilayer coverage of bi-isonicotinic acid, which is consistent with the shift observed in monolayer coverage on rutile. This shift is the combined effect of the screening of core-hole by the highly polarisable substrate in monolayer and steady state charging effect in multilayer coverage.

Figure 5.10 shows N 1*s* XPS for the monolayer coverage of bi-isonicotinic acid on anatase $TiO_2$(101) surface. Nitrogen peak located at 399 eV and a shake-up feature are detected in the higher binding energy at ∼402 eV. The shape and position of the shake-up feature are almost identical to The shake-up feature observed for the monolayer on rutile titanium oxide. As discussed previously for the monolayer on rutile, the shake-up process rises in the final state when the additional charge from the photoionisation process to the carboxylic group/substrate complex in the shake-up process.

### Density of states

A combination of valance photoemission spectra and an X-ray absorption spectrum (XAS) for a monolayer of bi-isonicotinic acid on anatase $TiO_2$(101) presented in common binding energy, as shown in Figure 5.11. In the XAS, the peaks located at the BE≈0.7 eV, BE≈−0.1 eV and BE≈ −2.6 eV are cor-

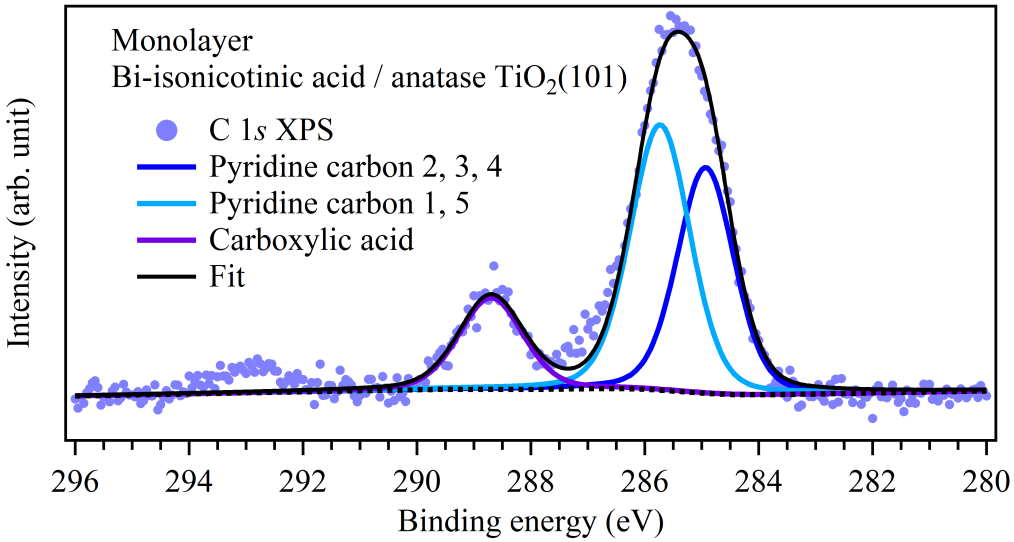



**Figure 5.9:** *C 1s XPS spectrum of monolayer coverage of bi-isonicotinic acid on anatase $TiO_2(101)$. Black dotted line corresponds to Shirley background. XPS spectrum was measured at normal emission (NE) using a photon energy of* 600 eV.

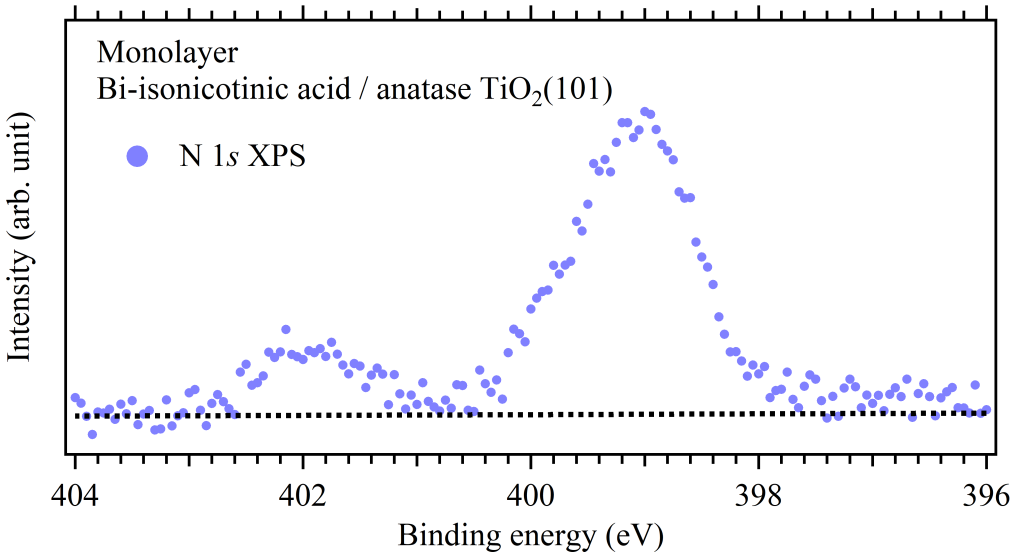



**Figure 5.10:** *N 1s XPS spectrum of monolayer coverage of bi-isonicotinic acid on anatase $TiO_2(101)$. Black dotted line corresponds to Shirley background. XPS spectrum was measured at normal emission (NE) using a photon energy of* 600 eV.

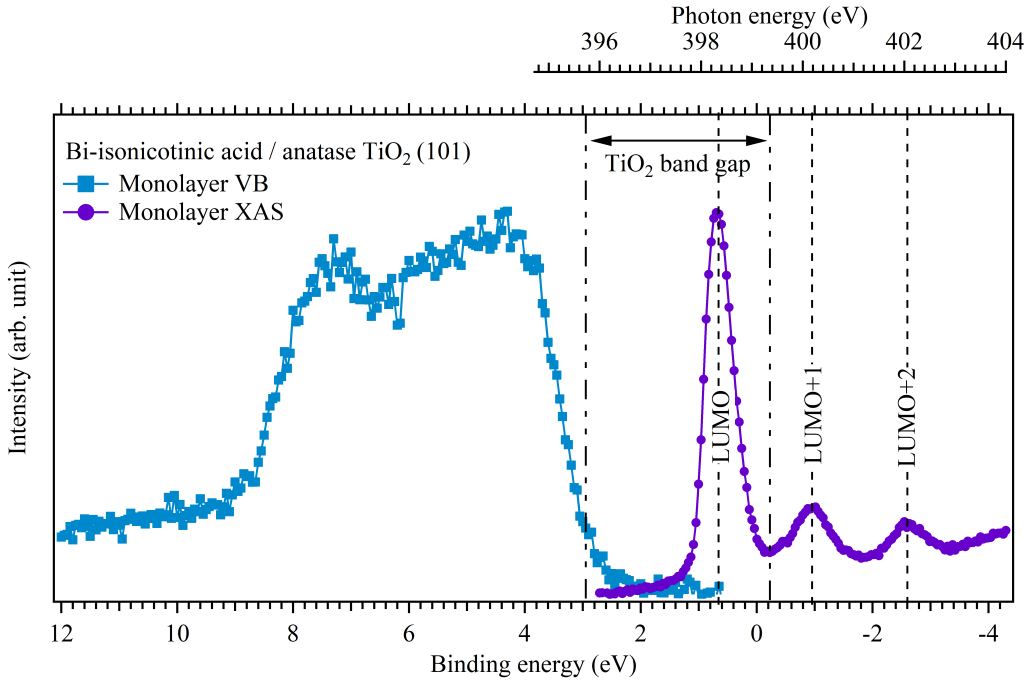



**Figure 5.11:** *Density of states plot of monolayer of bi-isonicotinic acid on anatase $TiO_2(101)$. The purple line shows an X-ray absorption spectrum (measured over the N 1s absorption edge) showing unoccupied states placed on a common binding energy scale with the blue line shows the valance spectrum of the monolayer measured by photoemission spectroscopy with a photon energy of* 350 eV. *All spectra were measured at normal emission.*

responds to LUMO, LUMO+1 and LUMO+2 states of the core-excited molecules, respectively. The LUMO lies entirely within the band gap of the substrate (Band gap of anatase $TiO_2$ is 3.2 eV [122]). So, the transfer of an electron from the valance band of the substrate to the LUMO for excitation is electronically forbidden. But the core excited LUMO+1 and LUMO+2 states overlap with the unoccupied states of the substrate. So, charge transfer from the substrate to these higher core-excited states is feasible.

### Resonant photoemission

The two dimensional plots of N 1*s* resonant photoemission data for monolayer coverage of bi-isonicotinic acid on anatase $TiO_2(101)$ is presented in Figure 5.12(a). RPES map represents the intensity of emitted valance photoelectrons as a function of incident photon energy and their measured binding energy. The horizontal black dash lines represent the regions of intensity at-

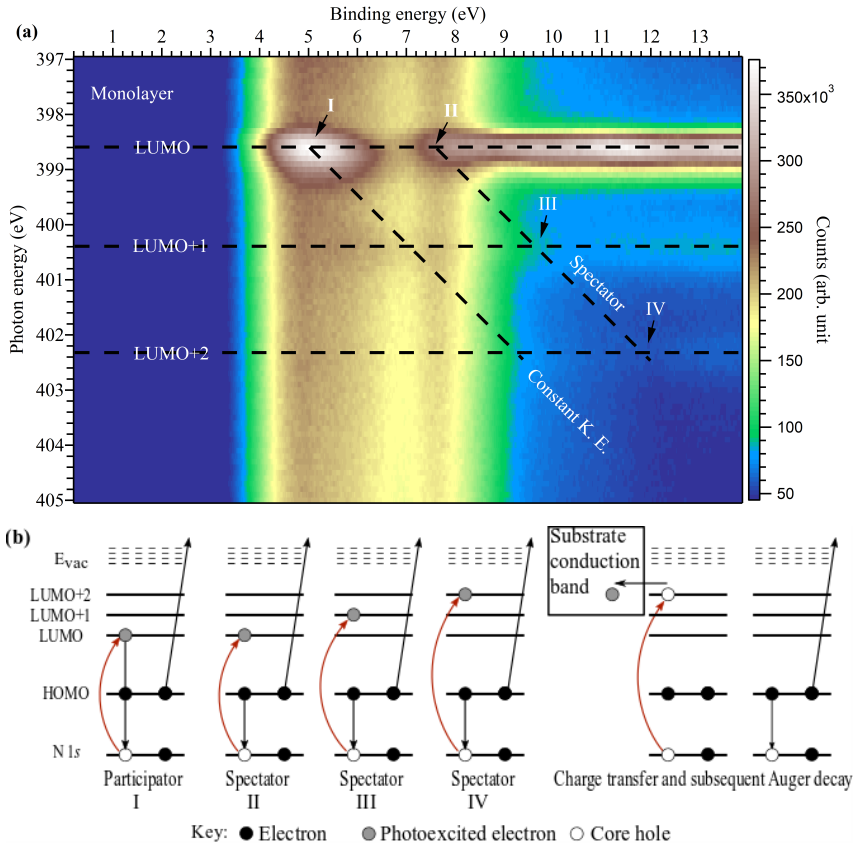



**Figure 5.12:** *(a) Resonant photoemission spectra for monolayer of bi-isonicotinic acid on anatase $TiO_2$(101). The LUMO energy levels are indicated with horizontal dashed lines and diagonal lines highlight constant kinetic energy features. (b) Schematics of proposed decay mechanisms after excitation of an N 1s core electron. The RPES spectra measured at normal emission (NE).*

tributed to excitation into the lowest unoccupied molecular orbital (LUMO) states, which appear at constant excitation energy. Unlike monolayer coverage on rutile, LUMO+1 core excited state is strong and distinguishable, located at 400.4 eV photon energy. The LUMO and LUMO+2 are situated at 398.6 eV and 402.3 eV in the photon energy scale respectively. The diagonal dashed lines are attributed to the spectator and Auger decay channels, which disperse linearly as the photon energy increased. The intense feature marked as I is due to the participator decay, where the photoexcited electron participates in the core-hole decay process while an electron from HOMO is emitted. The feature marked as II represents the spectator decay process. In this process the originally photoexcited electron does not participate in the core-hole decay process, instead, an electron from HOMO participates in the Auger like decay process and another electron from HOMO is emitted into the vacuum. The region marked III and IV, are attributed to the spectator decay process while an electron from the core level photoexcited to the LUMO+1 and LUMO+2 state respectively, whilst an electron from HOMO participate in Auger like decay process and another electron from HOMO emitted into the vacuum. The charge transfer mechanism from molecule to the substrate is also presented in Figure 5.12(b), where the originally excited electron from LUMO+2 is transferred to the conduction band of the substrate and subsequently followed by Auger decay to fill the core-hole and another electron from HOMO emitted to the vacuum.

The charge transfer time for electron transfer out of a particular unoccupied molecular orbital to the substrate's conduction band is calculated using Equation 5.1. For the core-hole clock implementation, integration of the participator electron intensity over the relevant binding energy window as a function of photon energy is conducted and compared to the associated X-ray absorption spectrum. Figure 5.13 represents the resonant photoemission spectra normalised to the LUMO of the associated X-ray absorption spectrum. Since the Lumo lies entirely within the band gap, any electron transfer

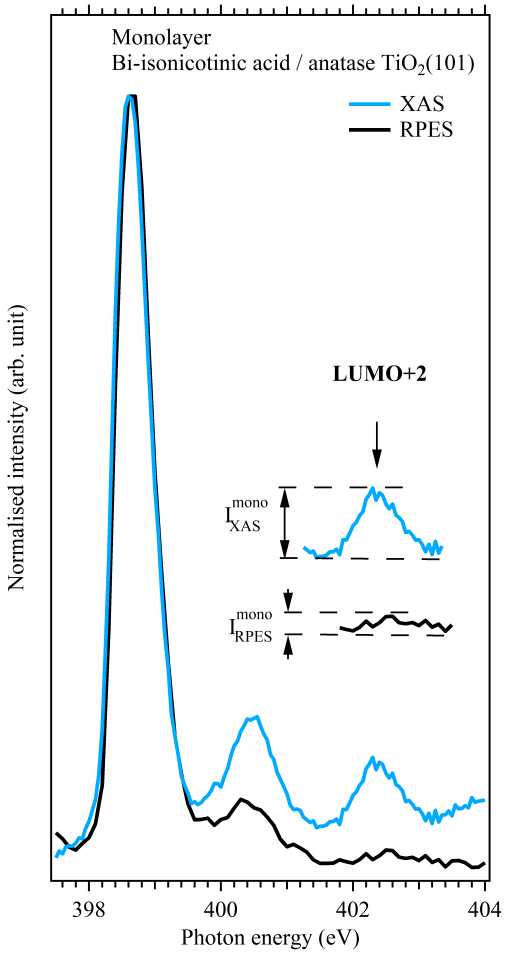



**Figure 5.13:** *N 1s RPES and N 1s XAS spectra of monolayer bi-isonicotinic acid on anatase $TiO_2$(101). The RPES spectrum obtained by integrating participator (RPES) region of Figure 5.12(a).*

to and from LUMO is electronically forbidden. So, the charge transfer time from LUMO+2 to the substrate's conduction band is calculated using the core hole clock implementation. The calculated relative intensities of the participator channel in the RPES as a fraction of the total X-ray absorption for the LUMO+2 is $I^{mono}_{RPES}/I^{mono}_{XAS} = 0.072$, whereas the corresponding value for multilayer, is $I^{multi}_{RPES}/I^{multi}_{XAS} = 0.2$. The charge transfer time from LUMO+2 to the conduction band of anatase $TiO_2$ is found to be $(3.4 \pm 0.2)$ fs.

### 5.3.3 Bi-isonicotinic acid / mesoporous $TiO_2$

#### XPS

Figure 5.14 shows O 1*s* XPS spectrum for the monolayer film deposited on mesoporous $TiO_2$ surface. The strongest peak located at 530.05 eV binding energy is attributed to the $TiO_2$ surface and two peaks located in the higher binding energy side of lattice oxygen feature derived from carboxylic groups of the molecule. The features located at 531.5 eV and 533 eV are corresponds to C=O and C-OH from the carboxylic acid groups. The presence of C-OH indicates evidence for the formation of physisorbed molecules remaining in the sample due to insufficient washing during sample preparation. Alternatively, It might be possible that the presence of C-OH indicates the formation of two different bonding geometry. For the anatase (101) surface, the calculation shows that the bidentate bridging through deprotonated carboxylic acid is energetically favorable. Whereas, for the anatase (001) surface, monodentate bonding through protonated C-OH is the most stable bonding geometry [13]. It is possible that the mesoporous titania is a mixture of 101 and 001 structures and the presence of the C-OH feature is due to the different bonding geometry which favour bonding through protonated C-OH. Another possibility could be contamination giving rise to the C-OH since the sample was prepared ex-situ. The presence of the C-OH feature in O 1*s* XPS was also found in the recent study of triphenylamine dye adsorbed mesoporous titania [31].

The C 1*s* spectrum is presented in Figure 5.15. At this spectrum, the peak at 285.25 and 288.8 eV are assigned to pyridine carbon atoms and carboxylic acid carbon atoms respectively. The pyridine carbon peak is attributed due to the contribution of two types of carbon atoms: emission from two carbon atoms which are the direct neighbour of nitrogen, located at 285.7 eV and the rest of the carbon atoms in the pyridine ring, located at 284.9 eV. The peak located at 286.8 eV, might be attributed to atmospheric contamination. The separation between pyridine and carboxylic acid peaks is found

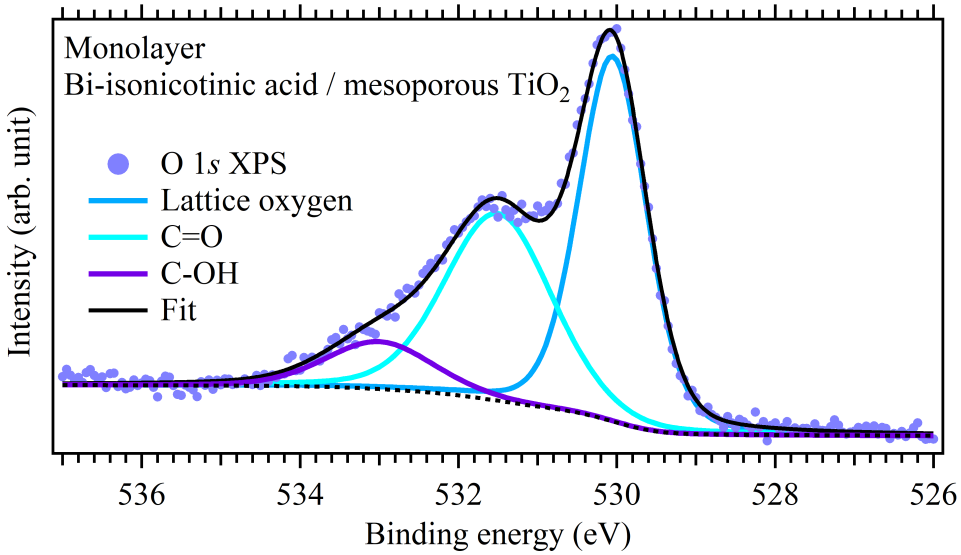



**Figure 5.14:** *O 1s XPS spectrum of monolayer coverage of bi-isonicotinic acid on mesoporous $TiO_2$. Black dotted line corresponds to Shirley background. XPS spectrum were measured at normal emission (NE) using a photon energy of* 600 eV.

to be 3.55 eV, which is 0.2 eV higher compared to the rutile and anatase.The intensity between ∼292 and ∼294 eV is attributed to shake-up processes.

Figure 5.16 shows the N 1*s* spectrum fitted with two peak. The peak assigned at 399 eV is attributed to the nitrogen atoms in the pyridine rings. The peak fitted in the higher binding energy at 400.1 eV may be attributed to the H-bonding due to the physisorbed molecules remaining in the sample due to insufficient washing. an interaction between the nitrogen with its lone-pair orbital and a hydrogen atom on a neighbouring molecule is responsible for the coulombic interaction and this N$\cdots$H interaction modifies the geometry of the neighbouring molecules from that induced by the van der Waals interaction alone. Which likely generates two distinguishable binding energies. But no evidence of Hydrogen bonding in bi-isonicotinic acid has been found in the previous study but traces of hydrogen bonding have been found in isonicotinic acid [29]. Alternatively, The second peak in the higher binding energy of N *s* might be because of the higher surface to bulk ratio in the mesoporous surface, so more molecules could adsorb and more O 1*s* signal from these. It could be that the higher binding energy peak is due to the nitrogen atoms interacting with the oxide due to the 3D nature of the surface.

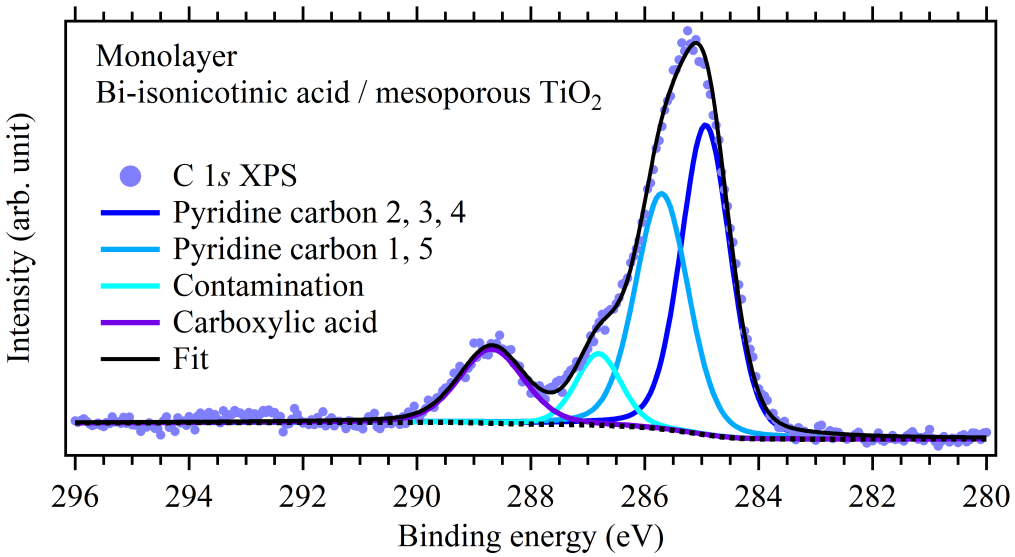



**Figure 5.15:** *C 1s XPS spectrum of monolayer coverage of bi-isonicotinic acid on mesoporous $TiO_2$. Black dotted line corresponds to Shirley background. XPS spectrum were measured at normal emission (NE) using a photon energy of* 600 eV.

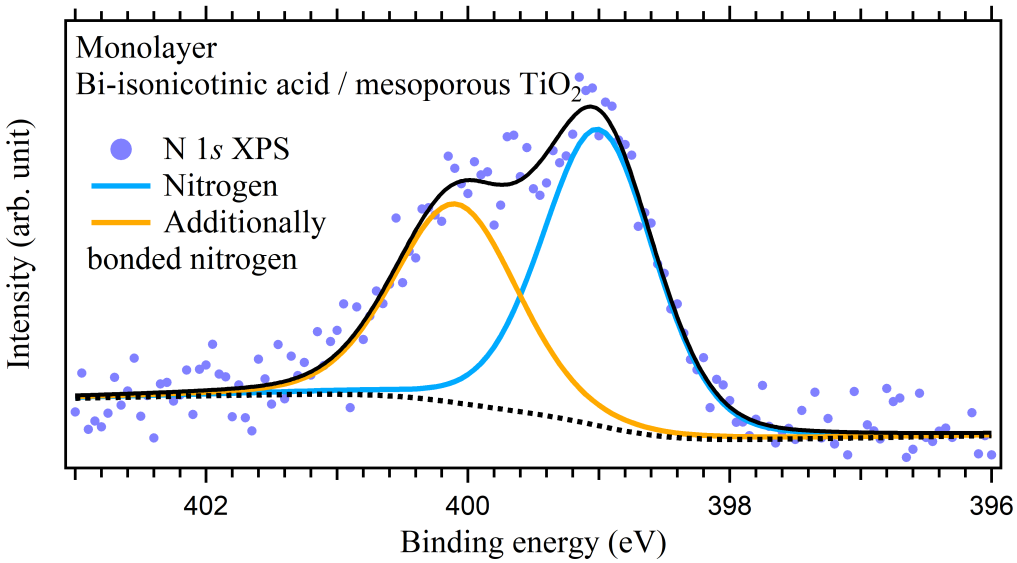



**Figure 5.16:** *N 1s XPS spectrum of monolayer coverage of bi-isonicotinic acid on mesoporous $TiO_2$. Black dotted line corresponds to Shirley background. XPS spectrum were measured at normal emission (NE) using a photon energy of* 600 eV.

### Density of states

Figure 5.17 shows a combination of valance photoemission spectrum and an X-ray absorption spectrum (XAS) for a monolayer of bi-isonicotinic acid on mesoporous $TiO_2$ presented in common binding energy. In the XAS, the peaks located at the BE≈0.6 eV, BE≈−0.1 eV and BE≈ −2.6 eV are corresponds to LUMO, LUMO+1 and LUMO+2 states of the core-excited molecules, respectively. According to the recently published valance band XPS of bare mesoporous titania, the binding energy position of the valence band maximum is found at 2.9 eV which places the corresponding conduction band edge at $-0.2 \pm 0.1$ binding energy [31]. As a consequence, The LUMO lies entirely within the band gap of the substrate but the core excited LUMO+1 and LUMO+2 states overlap with the unoccupied states of the substrate. So, the transfer of an electron from the valance band of the substrate to the LUMO for excitation is electronically forbidden. Whereas, charge transfer from the substrate to these higher core-excited states is possible.

### Resonant photoemission

Figure 5.17(a) presents a 2D plot of RPES measurement of monolayer coverage of bi-isonicotinic acid on mesoporous $TiO_2$, where the horizontal dashed lines correspond to LUMO and LUMO+2 respectively. The constant kinetic energy features are represented by diagonal dashed lines, which are attributed to the spectator and Auger decay channel. Three regions of interest have been marked on the map and explained through the schematic diagram presented in Figure 5.17(b). Figure 5.17(b) presents a schematic for the participator decay mechanism (Marked I) and spectator decay mechanism for core electron excitation to LUMO (marked II) and LUMO+2 (Marked II) states respectively. The charge transfer mechanism is also illustrated in the schematics, where the electron excited to LUMO+2 is transferred to the substrate's conduction band and subsequently followed by Auger decay to fill the core-hole and whilst

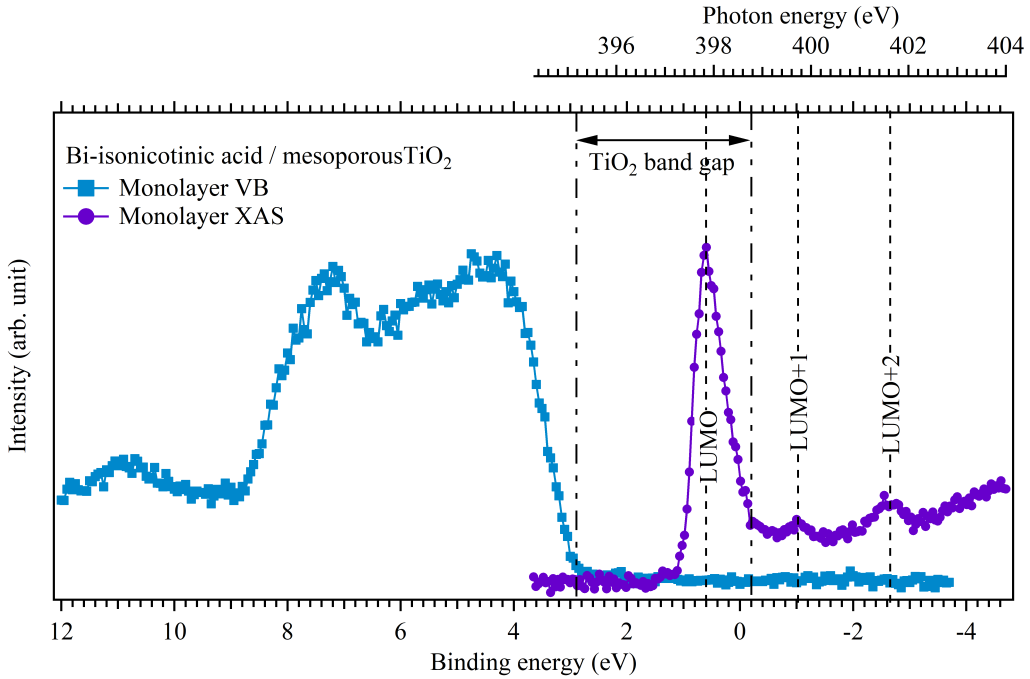



**Figure 5.17:** *Density of states plot of monolayer of bi-isonicotinic acid on mesoporous $TiO_2$. The purple line shows an X-ray absorption spectrum (measured over the N 1s absorption edge) showing unoccupied states placed on a common binding energy scale with the blue line shows the valance spectrum of the monolayer measured by photoemission spectroscopy with a photon energy of* 350 eV*. All spectra were measured at normal emission.*

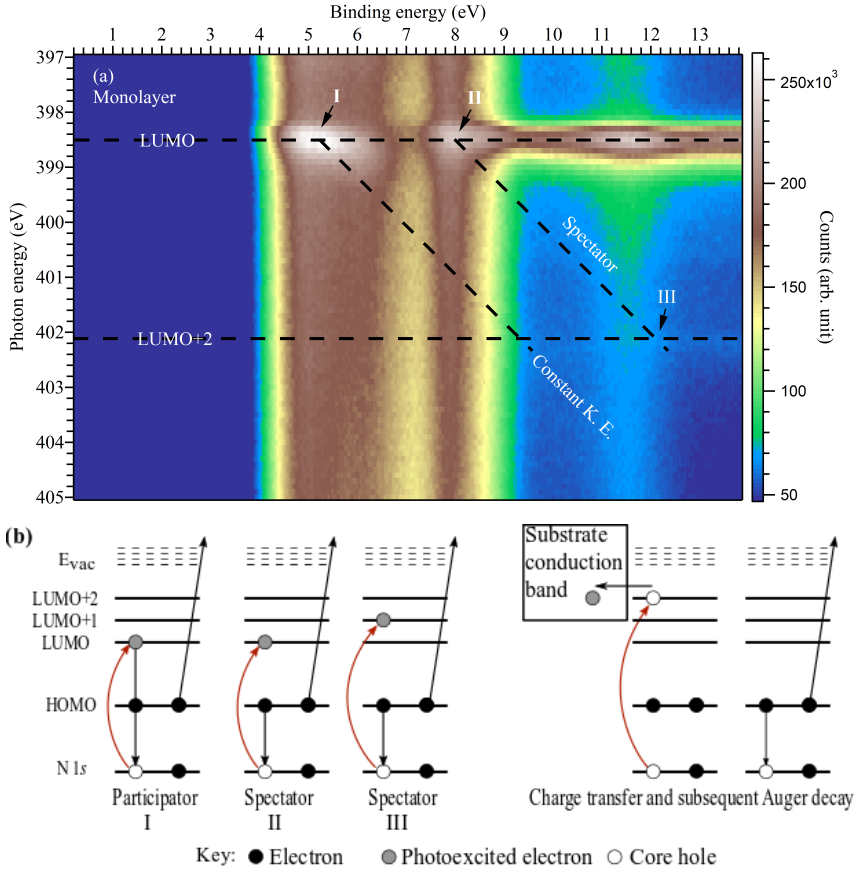



**Figure 5.18:** *(a) Resonant photoemission spectra for monolayer of bi-isonicotinic acid on mesoporous $TiO_2$. The LUMO energy levels are indicated with horizontal dashed lines and diagonal lines highlight constant kinetic energy features. Figure (b) shows schematics of proposed decay mechanisms after excitation of an N 1s core electron. The RPES spectra measured at normal emission (NE).*

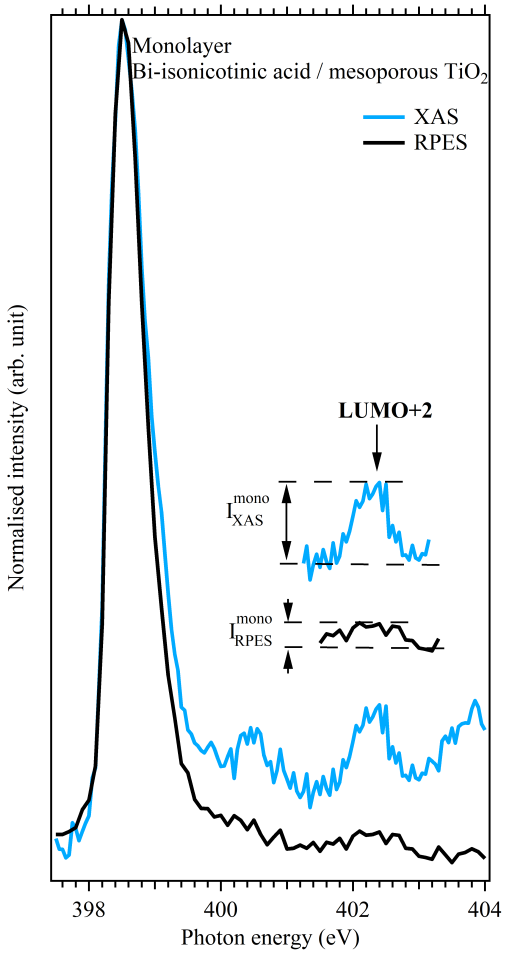



**Figure 5.19:** *N 1s RPES and N 1s XAS spectra of monolayer bi-isonicotinic acid on mesoporous $TiO_2$. The RPES spectrum obtained by integrating participator (RPES) region of Figure 5.18(a).*

another electron from HOMO is emitted to the vacuum. The charge transfer time for chemisorbed bi-isonicotinic acid is also determined using the core-hole clock implementation of RPES data. Integration of the participator channel intensity from RPES data has been normalised to the corresponding XAS data and presented in Figure 5.18. The charge transfer time from molecules to mesoporous titania was calculated by comparing the participator channels of monolayer and multilayer of RPES data using Equation 5.1.

The calculated relative intensities of the participator channel in the RPES as a fraction of the total X-ray absorption for the LUMO+2 is $I^{mono}_{RPES}/I^{mono}_{XAS}$ = 0.088, whereas the corresponding value for multilayer is $I^{multi}_{RPES}/I^{multi}_{XAS}$ = 0.2. The calculated charge transfer time from LUMO+2 to the conduction band of mesoporous $TiO_2$ is $(4.7 \pm 0.4)$ fs. The charge transfer time is higher

compared to rutile and anatase titanium dioxide and the possible reason might be because some of the molecules probed are physisorbed and therefore can not participate in fast charge transfer.

## 5.4 Summary and Conclusions

The chemisorbed bi-isonicotinic acid on rutile, anatase and mesoporous $TiO_2$ have been investigated using X-ray photoemission, resonant photoemission and X-ray absorption spectroscopy. XPS suggests an interaction between bi-isonicotinic acid and substrates through carboxylic acid groups. Whereas carboxylic acid groups are bonded to the rutile and anatase surfaces through bidentate bonding geometry but on a mesoporous substrate molecules are bonded through a mixture of bidentate and monodentate bonding geometry. The N $1s$ XAS shows that the LUMO lies entirely within the band gap of rutile, anatase and mesoporous $TiO_2$ respectively. As a consequence, the electron transfer between LUMO and substrates is electronically forbidden. However, LUMO+1 and LUMO+2 states of the core excited molecules overlap with the unoccupied states in the substrate. The depletion of intensity in the participator channel of the LUMO+1 and LUMO+2 states observed in RPES indicates the ultra-fast charge transfer to the surface in the core-hole lifetime. We have estimated the timescale of the charge transfer dynamics by comparing the relative intensities of the participator channel to the XAS for both monolayer and multilayer. The estimated charge transfer time from the LUMO+2 state to the conduction band of the substrate for chemisorbed bi-isonicotinic acid on rutile, anatase and mesoporous titanium dioxide is $(3.2 \pm 0.2)$, $(3.4 \pm 0.2)$ and $(4.7 \pm 0.4)$ fs respectively. The reason that the charge transfer time for bi-isonicotinic acid on mesoporous titanium oxide is higher might be due to the combination of fast charge transfer by chemisorbed molecules and the physisorbed molecules that do not participate in fast charge transfer.

# Chapter 6

# N3 on mesoporous $TiO_2$

## 6.1 Introduction

The dye complex, N3 (cis-bis(isothiocyanato)bis(2,2′-bipyridyl-4,4′-dicarboxylato)-ruthenium(II)) is one of the most studied dye found for dye-sensitized solar cells (DSSCs) [123]. A monolayer of N3 dye molecule adsorbed onto the rutile titanium dioxide surface showed visible light sensitivity for application in dye sensitised solar cell [124]. Previously, N3 dye has been studied on gold [16, 38, 125], aluminium oxides [17], rutile titanium oxide [11] surfaces. The N3 dye (the chemical structure shown in Fig. 6.1), has been shown to bond to rutile $TiO_2$(110) via deprotonation of two carboxylic acid groups of its bi-isonicotinic acid ligands forming a 2M-bidentate bond [11, 126, 127] to the five-fold coordinated Ti of the surface and one thiocyanate group form bond to the bridging oxygen of the surface. Rutile $TiO_2$(110) surface has an equal number of the six-fold and five-fold coordinated Ti, i.e. covered with O and five-fold coordinated Ti. A similar but moderately deformed surface binding ligand with two 2M-bidentate bonding geometry has been found in the previous study for anatase $TiO_2$ surface [13–15, 128].

Resonant inelastic X-ray scattering (RIXS) and Resonant photoemission (RPES) is found to be very effective to provide information about the occupied and unoccupied valance orbitals of a molecule and the coupling between them.

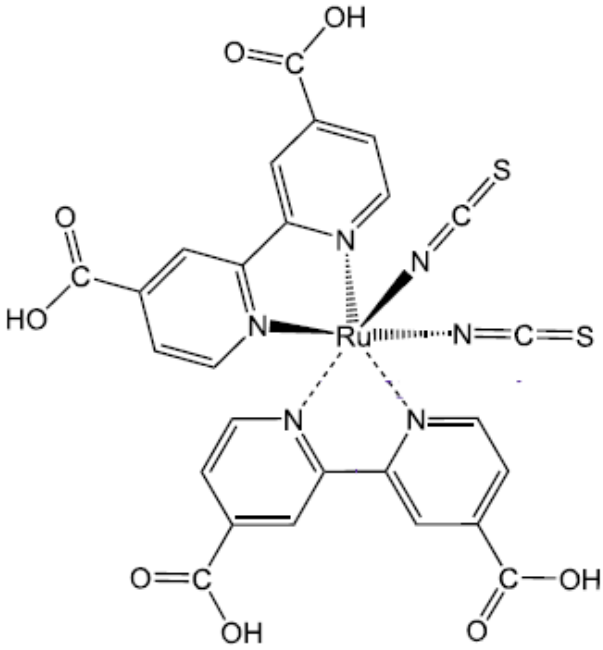



**Figure 6.1:** *Chemical structure of the N3 molecule.*

Recently, the detail electronic structure of N3 on rutile titanium oxide single crystal has been investigated using RIXS and RPES[125].

In this study, We have created model system by depositing monolayer and multilayer of N3 dye on mesoporous $TiO_2$ electrode, which is constructed on fluoride-doped tin oxide (FTO) coated glass. Then we investigated vibronic losses and the electronic structure of this model system. The electronic structure of N3 molecules is obtained from density functional theory (DFT) calculation and compared with the experimental data obtained by resonant inelastic X-ray scattering (RIXS) and resonant photoemission spectroscopy (RPES) of both monolayer and multilayer coverage of N3 dye.

## 6.2 Methods

Preparation and coverage calibrations of the N3/$TiO_2$ were done in our laboratory at the University of Nottingham. Coverage calibrations were performed using X-ray photoelectron spectroscopy (XPS). The N3 monolayer was deposited on mesoporous $TiO_2$ by soaking the $TiO_2$ in a solution of $\sim$ 5 mg of N3 in 200 ml of methanol for a week. After that, the sample was washed with

methanol until all the physisorbed molecules were removed to leave a single chemisorbed layer and blow-dried with $N_2$ gas. The multilayer N3 dye for RIXS measurement was prepared using the same method used for monolayer preparation but kept the sample in the solution for 10 days. The preparation takes place in an inert gas glove box. The physisorbed N3 dye for RPES measurements was deposited using spin coating from solution on a silicon wafer. The samples were packed for transportation to the beamline and one sample was transferred to the XPS for characterization.

Resonant inelastic X-ray scattering (RIXS) measurements were conducted at the SEXTANTS beamline located at the national French synchrotron facility SOLEIL in Paris by using a high-resolution grating X-ray spectrometer AERHA. The beamline was operated over a $50 - 700\,\mathrm{eV}$ photon energy range. The radiation has a high degree of elliptical polarization and may be considered as linearly polarized for the purpose of this study. The pressure recorded during the experiments in the analysis chamber was in the low $10^{-10}$ mbar range. During measurements at the SEXTANTS beamlines, to avoid beam damage the sample was repeatedly moved up and down within the sample's length. After taking RIXS spectra, a new line on the sample was taken to measure. The RIXS spectra were measured between photon energy of 397 eV and 405 eV.

Resonant photoemission spectroscopy (RPES) was performed at the surface and material science end station at the FlexPES beamline situated on the 1 GeV storage ring at the MAX IV synchrotron facility in Sweden. The experimental station is equipped with a planar undulator and collimated plane grating monochromator and a Scienta SES-2002 hemispherical analyzer for photoelectron spectroscopy (PES), positioned at an angle of 40 ° from the incident photon beam. The monochromator can be focused to a $65 \times 10\,\mu m$. Measurements were taken at normal emission.

The binding energy scales were calibrated by setting the lattice oxygen peak in O $1s$ to 530.05 eV [27]. XPS spectra and the valance band spectra were measured at $h\nu = 600\,\mathrm{eV}$ and $h\nu = 350\,\mathrm{eV}$ respectively. XPS data were

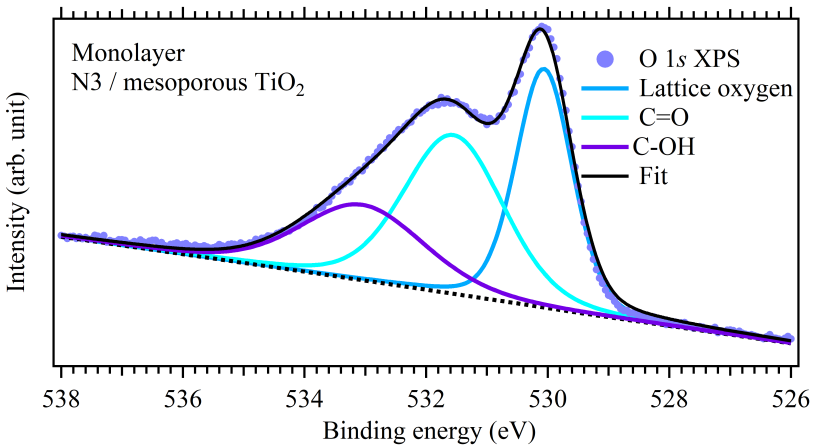



**Figure 6.2:** *O 1s XPS spectrum of N3 monolayer on a mesoporous $TiO_2$. Black dotted line corresponds to Shirley background. Both spectra were measured at normal emission (NE) using a photon energy of* 600 eV.

peak fitted using a pseudo-Voigt function allowing a fixed Lorentzian width (0.3 eV) and variable Gaussian width following the subtractions of a Shirley background [97].

## 6.3 Results and Discussion

Figure 6.2 shows the O 1*s* XPS spectrum of the N3 monolayer on mesoporous $TiO_2$. The dominating peak is attributed to $TiO_2$ substrate and the other two small peaks are due to the carboxyl oxygen C=O, $COO^-$, and C-OH in the bi-isonicotinic acid. These peaks are situated at 530.05 , 531.5 , and 533.05 eV respectively. Bi-isonicotinic usually bonded to the $TiO_2$ through deprotonation of the carboxyl groups[11, 126, 127] , where two oxygen atoms are chemically equivalent and share an electron. If all the molecules are equivalently bonded to the surface, then the ratio between $COO^-$, C=O, and C-OH is expected to be 3:1 [11]. But in our case, the calculated ratio of the intensity of $COO^-$, C=O, and C-OH from experimental data is 2:1. This can happen only if all molecules are not bonded equivalently or a higher number of the carboxyl groups in the bi-isonicotinic acid bonded to the mesoporous $TiO_2$ through deprotonation. The presence of C-OH suggests that physisorbed molecules remained in the sample due to inadequate washing during sample preparation. Alternatively, It

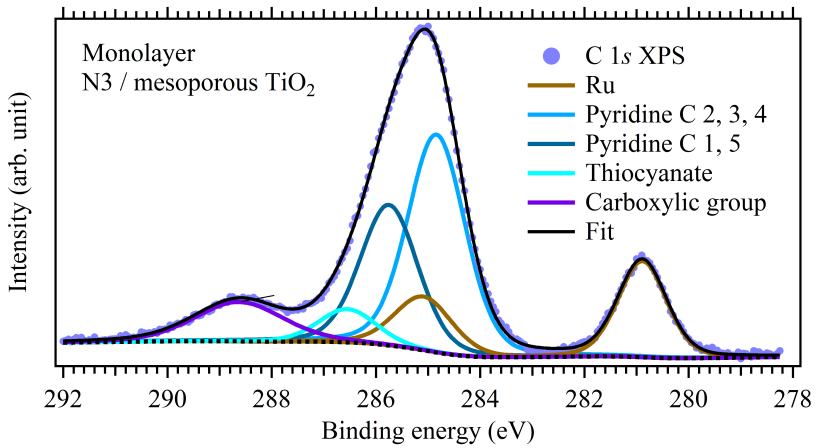



**Figure 6.3:** *C 1s XPS spectrum of N3 monolayer on a mesoporous $TiO_2$. Black dotted line corresponds to Shirley background. Both spectra were measured at normal emission (NE) using a photon energy of* 600 eV.

is also possible that the creation of two distinct bonding geometries is indicated by the presence of C-OH. Calculations indicate that the bidentate bridging via deprotonated carboxylic acid is energetically advantageous for the anatase (101) surface. Contrarily, monodentate bonding through protonated C-OH is the most stable bonding geometry for anatase (001) surface [13]. The existence of the C-OH feature may be a result of the altered bonding geometry, which favours bonding through protonated C-OH, in the mesoporous titania, which may be a blend of the 101 and 001 structure. Given that the sample was created ex-situ, contamination that results in C-OH might also be a possibility. In a recent investigation of triphenylamine dye-adsorbed mesoporous titania, the C-OH feature in O 1*s* XPS is also observed [31].

C 1*s* spectrum measured using XPS is presented in Figure 6.3. The peak located at 280.9 eV is attributed to the Ru $3d_{5/2}$ with corresponding spin-orbit splitting doublet Ru $3d_{3/2}$ is located in 4.2 eV higher binding energy [129]. The contribution of measured carbon intensity is due to the pyridine carbon (2, 3, 4), pyridine carbon (1, 5), thiocyanate, and carboxyl group, which are located at 284.8 , 285.7 , 286.5 and 288.6 eV respectively. The pyridine ring peaks located at 284.8 , 285.7 eV are due to the emission from two different types of carbon binding energy. This is consistent with the previous study on the adsorption of N3 dye on gold [16, 38]. The higher binding energy

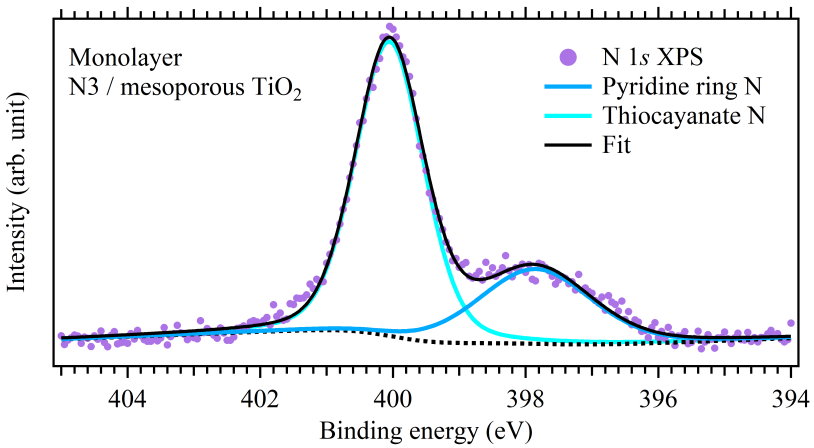



**Figure 6.4:** *N 1s XPS spectrum of N3 monolayer on a mesoporous $TiO_2$. Black dotted line corresponds to Shirley background. Both spectra were measured at normal emission (NE) using a photon energy of* 600 eV.

side of the peak is due to the emission from the carbon atoms which are direct neighbours of the nitrogen atom and the lower binding energy side is attributed to the remaining carbon atoms of the pyridine ring. The calculated ratio of carbon atoms from fitted pyridine ring (2, 3, 4), pyridine ring (1, 5), carboxyl group and thiocyanate peak is 10:2:1 [11, 26, 130]. This is consistent with the chemical structure of the N3 monolayer on $TiO_2$ as shown in Figure 6.1.

Figure 6.4 shows the N 1*s* XPS spectrum. The fitted peak at 400.05 and 397.8 eV correspond to the pyridine and thiocyanate N atoms.

### 6.3.1 Density of states

Figure 6.5 shows a combination of valance photoemission spectrum and an X-ray absorption spectrum (XAS) for a monolayer of N3 on mesoporous $TiO_2$ presented in common binding energy. This is achieved by subtracting the N 1*s* core level binding energy from the photon energy scale of the N 1*s* XAS. The detailed process of combining valance photoemission spectrum and X-ray adsorption spectrum is discussed elsewhere [130]. In the XAS, the peaks located at the BE≈1.3 eV, BE≈−1.4 eV and BE≈ −2.5 eV are corresponds to LUMO, LUMO+1 and LUMO+2 states of the core-excited molecules, respectively. According to the recently published valance band XPS of bare mesoporous

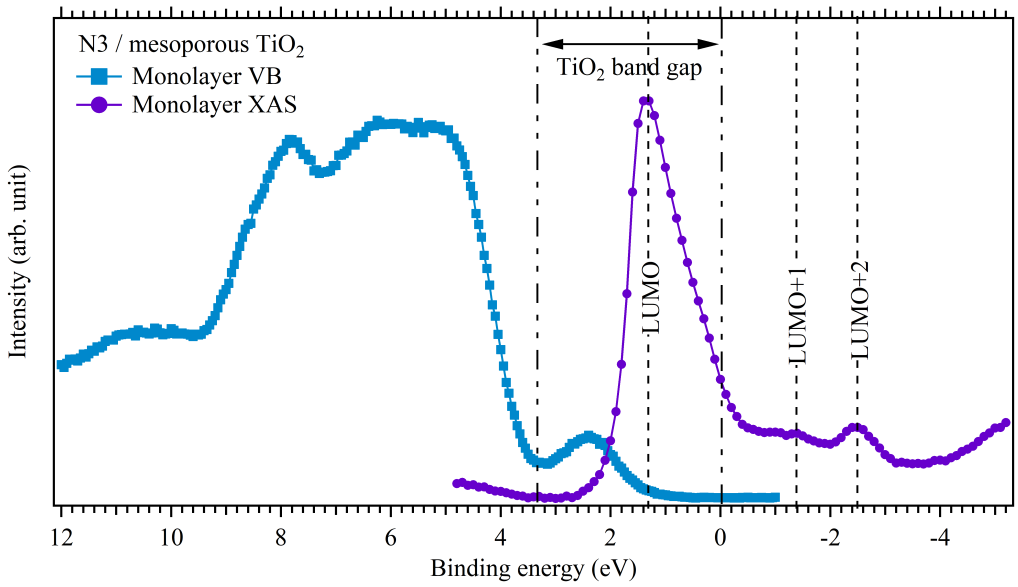



**Figure 6.5:** *Density of states plot of monolayer of N3 on mesoporous $TiO_2$. The purple line shows an X-ray absorption spectrum (measured over the N 1s absorption edge) showing unoccupied states placed on a common binding energy scale with the blue line shows the valance spectrum of the monolayer measured by photoemission spectroscopy with a photon energy of* 220 eV*. All spectra were measured at normal emission.*

titania, the band gap is found to be $3.1 \pm 0.1$ eV [31]. As a consequence, The LUMO lies entirely within the band gap of the substrate but the core excited LUMO+1 and LUMO+2 states overlap with the unoccupied states of the substrate. So, the transfer of an electron from the valance band of the substrate to the LUMO for excitation is electronically forbidden. The charge transfer from the substrate to these higher core-excited states is possible.

### 6.3.2 Resonant inelastic X-ray scattering (RIXS)

The N 1*s* RIXS map measured for the monolayer N3 dye on mesoporous $TiO_2$ is shown in Figure 6.6. The diagonal feature above 397 eV that disperses linearly in emission energy as the absorption energy increases is attributed to the elastic (Rayleigh) scattering. The small inelastic losses indicated in the Figure 6.6 by the downward arrow are due to vibronic coupling. The features observed below 397 eV emission energy are attributed to inelastic scattering, resulting from the N 1*s* core-hole being filled by valence electrons from the occupied molecular orbitals.

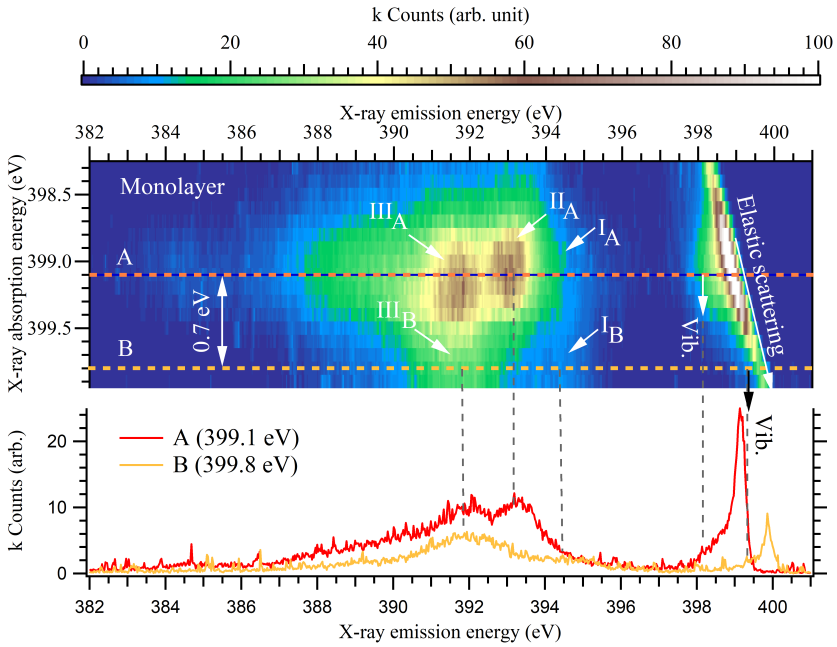



**Figure 6.6:** *N 1s RIXS of the N3 monolayer on mesoporous $TiO_2$. Line profiles A (red) and B (yellow) have been extracted from the map and represent excitation of the nitrogen atoms in the bi-isonicotinic acid and thiocyanate ligands, respectively. Intensity attributed to vibronic coupling from the two ligands is indicted with the downward arrows.*

The first resonance (A) representing excitation into the LUMO is observed at absorption energy centered around 399.1 eV. The inelastic scattering at this resonance exhibits a weak feature at 394.5 eV ($I_A$) emission energy and an intense feature at 393.2 eV ($II_A$), followed by a series of decreasing intensity peaks at 391.9 ($III_A$), 389 , and 384.5 eV. A second resonance (B) is observed to be 0.7 eV higher at 399.8 eV absorption energy. Here, we observe features at 394.5 eV ($I_B$) and 391.9 eV ($III_B$) in the inelastic scattering, but effectively no intensity at the emission energy of feature $II_A$.

The N 1*s* RIXS map measured for the multilayer N3 dye on mesoporous $TiO_2$ is shown in Figure 6.7. The RIXS signal from the multilayer is much stronger than that from the monolayer due to the presence of many layers of physisorbed N3, effectively isolated from the substrate. The diagonal feature that disperses linearly is observed above 397 eV and the vibronic losses are indicated by the downward arrow. The features observed below 397 eV emission energy are attributed to inelastic scattering. The first resonance (A) represent-

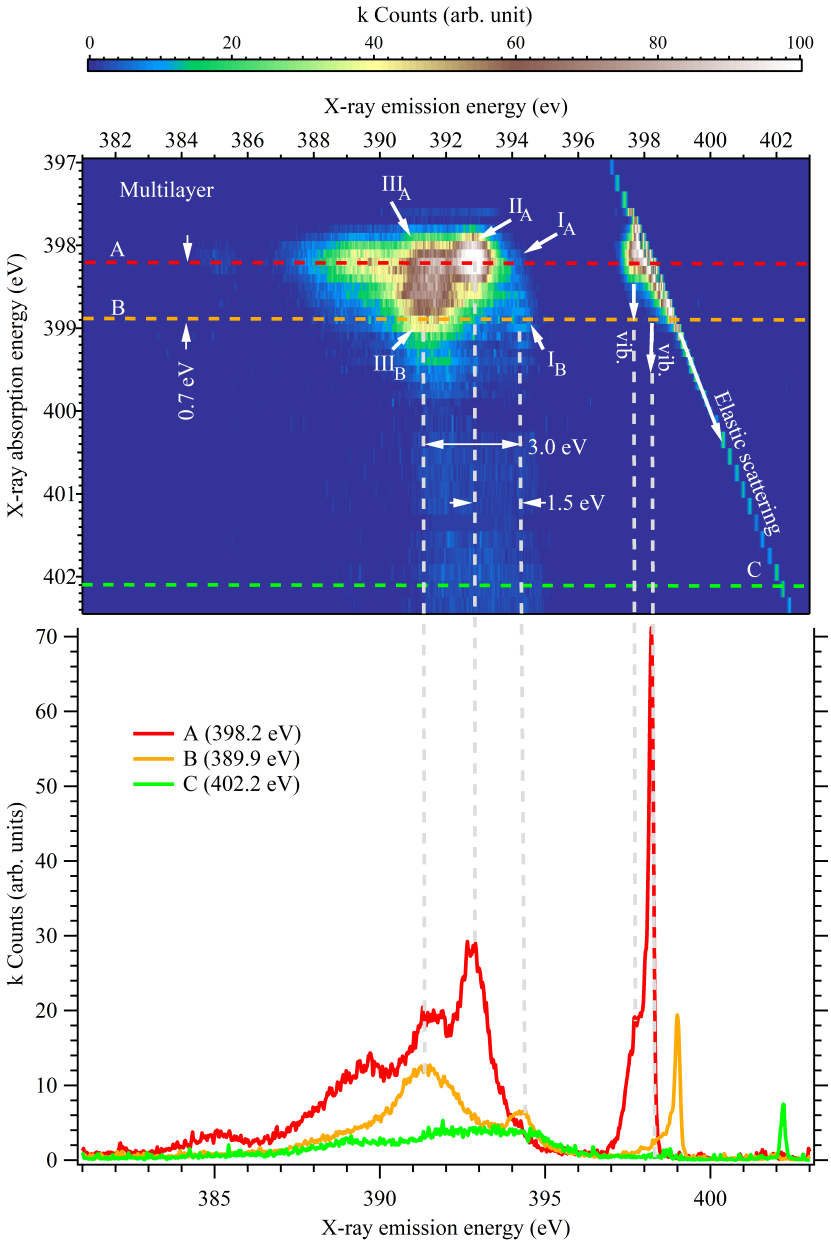



**Figure 6.7:** *N 1s RIXS of the N3 monolayer on mesoporous $TiO_2$. Line profiles A (red) and B (yellow) have been extracted from the map and represent excitation of the nitrogen atoms in the bi-isonicotinic acid and thiocyanate ligands, respectively. Intensity attributed to vibronic coupling from the two ligands is indicted with the downward arrows. Line profile C (green) has also been extracted, where the vibronic feature associated with the resonance A (bi-isonicotinic acid) LUMO reappears as a weak feature.*

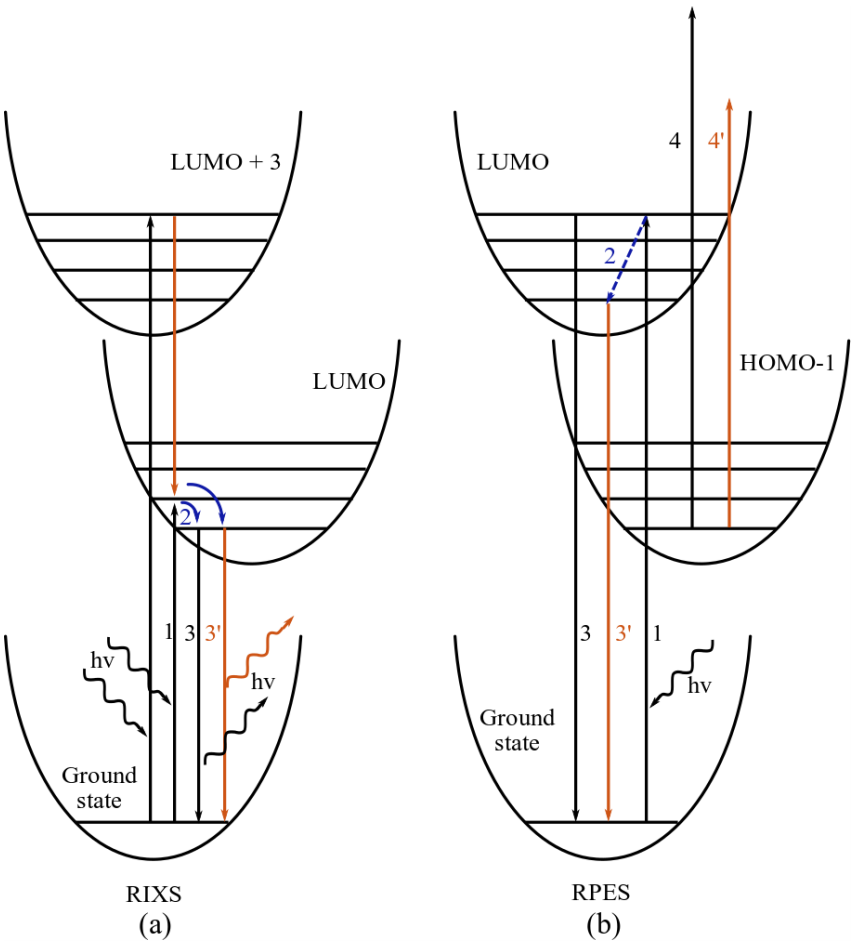



**Figure 6.8:** *Schematic diagram of the electronic transitions in the presence of vibronic coupling features in a simplified Franck-Condon scheme of RIXS and RPES experiment. Here, transition 1 represents X-ray absorption events for core level electron excitation to one of the lowest unoccupied molecular orbitals. Transition 2 illustrates the dissipation of vibrational energy within the core-hole lifetime leading to the inelastic participator decay shown by transition 3 and the emission of an electron (transition 4′) in RPES. In RIXS this leads to the emission of a photon of lower energy (inelastic scattering).*

ing excitation into the LUMO is observed at absorption energy centered around 398.2 eV. The inelastic scattering at this resonance exhibits a weak feature at 394.4 eV ($I_A$) emission energy and an intense feature at 393 eV ($II_A$), followed by a series of decreasing intensity peaks at 391.6 ($III_A$), 389.7 , and 385 eV. A second resonance (B) is observed to be 0.7 eV higher at 389.9 eV absorption energy. Here, we observe a feature at 394.4 eV ($I_B$) and 391.6 eV ($III_B$) in the inelastic scattering, but effectively no intensity at the emission energy of feature $II_A$.

The elastic peak is contributed due to the participator core-hole decay

and the vibronic coupling feature is explained in a Frank Condon scheme where the excited electron rapidly couples to the lowest vibrational level of the LUMO-derived resonance. The electron then decays to fill the core-hole, with the emission of a photon energy corresponding to the difference between this lowest vibrational state and the N $1s$ ground state [19, 20]. In the case of vibronic coupling, the photon emission generates from a transition of core excited electron. So, these photons must be considered as the part of participator core-hole decay channel. Schematic diagram of the vibronic coupling features in RIXS illustrated in Figure 6.8(a).

At resonance A in the RIXS map, the vibronic coupling feature is detected for monolayer and multilayer at almost constant emission energy of ∼398.0 and ∼397.5 eV respectively. The intensity of this feature is much decreased and is almost absent in the line profile by the time resonance B is reached. However, looking at the elastic peak in line profile B, we see a shoulder for monolayer and multilayer coverage on the lower emission energy side at ∼399.3 and ∼398.5 eV respectively. These two observations imply that resonance B is exciting into a molecular orbital that is completely distinct from resonance A. So, the low intensity at $I_A$ region is attributed to the weak coupling to the HOMO at the LUMO resonance (A) and the intense intensity $I_B$ region is attributed to the strong coupling to the HOMO at the resonance B. Recently, a detailed and systematic study on isonicotinic acid, bi-isonicotinic acid, and N3 dye powder using RIXS, resonant photoemission spectroscopy and DFT calculation established that resonance A attributed largely to the bi-isonicotinic acid ligands. Resonance B, on the other hand, is therefore attributed to excitation into higher unoccupied molecular orbitals localized largely on the thiocyanate ligands[125]. It is also observed for multilayer coverage that characteristics of both resonance A and B return after X-ray absorbed energy 400.4 eV (indicated by line profile C (green) located at 402.1 X-ray absorbed energy). It is possible only if decay occurs in two steps where the photoexcited electron first decays from these higher unoccupied orbitals to the LUMO

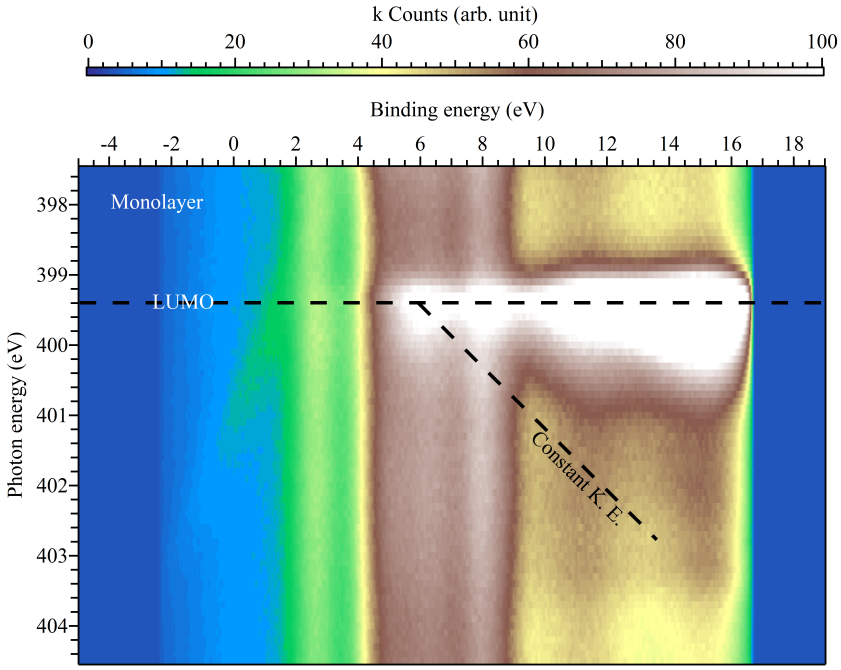



**Figure 6.9:** *Resonant photoemission spectra for monolayer of N3 dye on mesoporous $TiO_2$. The LUMO energy level is indicated with horizontal dashed line and diagonal line highlight constant kinetic energy features. Both surfaces measured at normal emission (NE).*

before filling the N 1s core-hole, as shown in Figure 6.8(a).

### 6.3.3 Resonant photoemission (RPES)

The N 1*s* resonant photoemission (RPES) data for monolayer and multilayer coverage of N3 on mesoporous $TiO_2$ surface is shown in Figure 6.9 and Figure 6.10, respectively. The two dimensional plots represent the intensity of emitted valance photoelectrons as a function of incident photon energy and their measured binding energy. The features observed in RPES are the same that we have observed in RIXS. The resonant enhancement of photoemission from the occupied valence state involved in core hole decay is the participator channel in RPES. In this instance, a core-excited LUMO electron fills the core hole while an Auger-like process emits an electron from the highest occupied molecular orbital (HOMO). Whereas, in RIXS the elastic participator event leads to an emission of a photon (hv). Figure 6.8 provides a schematic illustration of this. It is anticipated that the twisted elliptical features attributed

to the vibronic coupling will be visible in the participator channel centered around 2 eV binding energy because this feature was previously seen in the RIXS and RPES maps of bi-isonicotinic acid on rutile $TiO_2$ [19]. But the feature centered around 2 eV binding energy is too weak to observe vibronic coupling. The vibronic coupling features are already discussed using a simplified Franck-Condon scheme for RIXS. It is expected that in the absence of vibronic coupling, the binding energy of the participator channel will remain constant as the absorption energy rises. In the absence of vibronic coupling, the participator decay from the higher vibrational energy of the LUMO will emit an electron of higher kinetic energy. As shown in Figure 6.8(b), core-hole decay in participator decay channel from a higher state of LUMO derive resonance (transition 1) will emit an electron of higher kinetic energy (transition 4). Whereas, core-hole decay from the lower state of LUMO derive resonance (transition 3′) will emit an electron of kinetic energy (transition 4′) equivalent to the energy difference between the excited energy state of LUMO derive resonance and the core-hole energy. So, the kinetic energy of the emitted electron will increase linearly with increasing photon energy resulting in constant binding energy. On the other hand, if the transition occurs through vibronic coupling (transition 2), the participator decay proceeds from (almost) the same vibrational state of the LUMO-derived resonance(transition 3′) then the kinetic energy of the emitted electron will be correspondingly reduced (transition 4′). It is possible that core-hole decay involving three energy level with or without through vibronic coupling will emit an Auger electron of constant kinetic energy. The RPES spectrum of both monolayer and multilayer coverage shows constant kinetic energy features marked by diagonal dashed lines, disperse linearly as the photon energy is increased.

The RPES spectra for multilayer coverage of N3 is shown in Figure 6.10, resonance A and B are presented by red and yellow dashed lines. Resonance A is located at 399.4 eV and resonance B is located 0.7 eV higher absorption energy relative to resonance A at 400.1 eV. Where resonance A is attributed

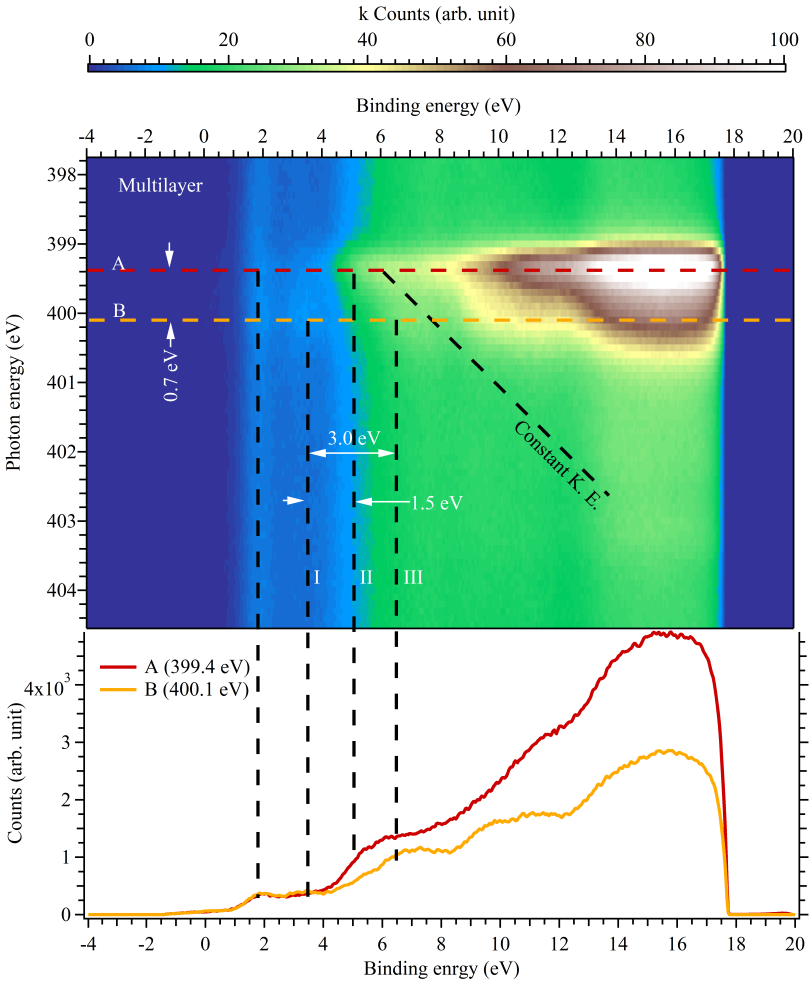



**Figure 6.10:** *Resonant photoemission spectra for multilayer of N3 dye on mesoporous $TiO_2$. The LUMO energy level is indicated with horizontal dashed line and diagonal line highlight constant kinetic energy features. Line profiles A (red) and B (yellow) have been extracted from the map and represent excitation of the nitrogen atoms in the bi-isonicotinic acid and thiocyanate ligands, respectively. Both surfaces measured at normal emission (NE).*

to the bi-isonicotinic acid ligands and B resonance corresponds to the thiocyanate ligand. Here we observe a weak resonant feature of HOMO located at 2 eV binding energy. A participator enhancement (I) is observed at 3.5 eV and an intense feature located at the 5 eV (II) is attributed due to the next experimentally distinct occupied molecular orbital. This feature is not observed at resonance B, suggesting that this orbital is localised on the bi-isonicotinic acid ligands. At resonance B, the participator resonant enhancement (I) is observed at 3.5 eVand the next enhancement (III) is observed at a binding energy of 6.5 eV. The separation between these two intense features is 3 eV, which is identical to the corresponding value observed in RIXS (3 eV).

### 6.3.4 Calculated molecular orbitals

Figure 6.11 shows the intensity of emission energy of N3 molecule as a function of incident energy that was created using DFT calculations. This two dimensional plot is the combination of all calculated distinct molecular orbital. The energy produced from the computational analysis result does not coincide with the experimental data but gave an insight into the orbital localization. The thorough computational analysis for DFT calculation was described in a study by Monat *et al.* [131].

Figure 6.12 provides a general picture of five relevant largely de-localized frontier orbitals. The orbital 157 shows that some intensity shifted to the bi-isonicotinic acid ligand. The orbital 164 (LUMO) is primarily localized on the bi-isonicotinic acid, whereas the orbital 163 (HOMO) is primarily localised on the thiocyanate ligands and Ru atom. When we get to orbital 175, the density is dispersed across the entire molecule. Once we get to orbital 188, we can observe that it is totally localized on the thiocyanate ligands.

The calculated DFT demonstrates that the HOMO is mostly situated on the thiocyanate ligands, whereas the LUMO is primarily located on the bi-isonicotinic acid ligand. In accordance with the RIXS and RPES maps, we

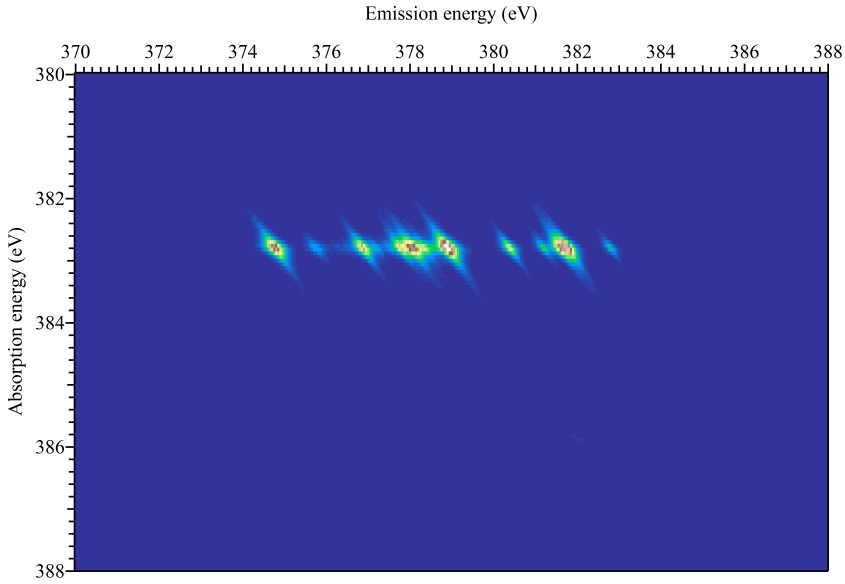



**Figure 6.11:** *The two dimensional plots represent the intensity of emission energy of N3 molecule as a function of incident energy determined by DFT calculation.*

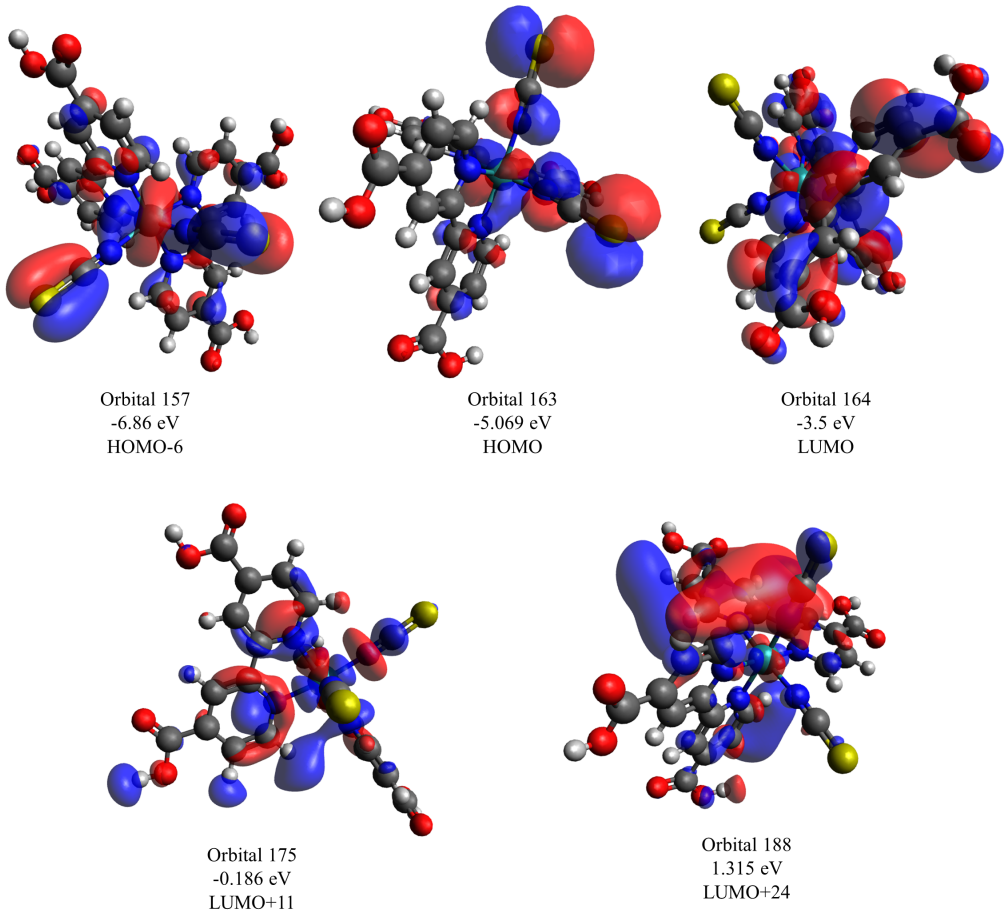



**Figure 6.12:** *From a DFT calculation, five important ground state molecular orbitals are identified and reported here. A and B resonances are predominately caused by the LUMO and LUMO+24, respectively.*

would then expect a weak coupling to the HOMO at the LUMO-resonance (A). Resonance B, on the other hand, is explained by excitation into higher unoccupied molecular orbitals that are mostly centred on the thiocyanate ligands.

## 6.4 Summary and Conclusions

The monolayer and multilayer coverage of the N3 dye complex (cis-bis(isothiocyanato) bis(2,2′-bipyridyl-4,4′-dicarboxylato)-ruthenium(II)) on mesoporous $TiO_2$ have been investigated using resonant inelastic X-ray scattering (RIXS) and resonant photoemission spectroscopy (RPES). X-ray photoemission spectroscopy (XPS) spectra reveal the presence of the protonated carboxylic group, which might be evidence of the absorption of N3 on mesoporous substrate bonded through a mixture of bidentate and monodentate bonding geometry. The intense features and vibronic coupling observed in RIXS and RPES have been discussed thoroughly. The RIXS, RPES and DFT calculations have been combined to provide an understanding of the electronic structure of complex molecules. The orbital contributions of the bi-isonicotinic acid and thiocyanate ligands were used to interpret the obtained RIXS and RPES data.

# Chapter 7

# Conclusions and future work

The aim of this thesis is to investigate model systems that are made up of molecules on a surface and are relevant to dye sensitised solar cells. It begins with an investigation into defect migration in single crystal rutile titanium dioxide, followed by an investigation into the interaction of defects with oxygen, water, and air molecules. The investigation of the bonding and charge transfer interactions of bi-isonicotinic acid on rutile, anatase, and mesoporous titanium dioxide follows. This is accomplished using a variety of soft X-ray synchrotron-based spectroscopies, such as X-ray photoelectron spectroscopy (XPS), X-ray absorption spectroscopy (XAS), and resonant photoemission spectroscopy (RPES). Finally, The bonding and vibronic coupling of N3 dye on mesoporous titania have been investigated using similar experimental techniques, as well as resonant inelastic X-ray scattering (RIXS) and DFT calculations.

Chapter 3 shows the experimental evidence of defects migration to the surface from the subsurface of rutile at low annealing temperatures. Defective rutile $TiO_2$(110) prepared by $Ar^+$ sputtering was subjected to liquid water exposure, to create a sample with a substantially defective subsurface coexisting with a defect free surface, offering a platform for studies of annealing-induced migration of titanium defects using XPS. At low annealing temperatures, we observed an increase in $Ti^{3+}$ concentration, which we attribute to $Ti^{3+}$ migra-

tion to the previously defect-free surface. At higher annealing temperature, a fast and distinct depletion of $Ti^{1+}$ is seen, with a corresponding increase in $Ti^{3+}$ shortly followed by $Ti^{4+}$, which is possibly explained by the gradual conversion of $Ti^{1+}$ defects to $Ti^{4+}$ through intermediate oxidation states. We observe a steady fall of the remaining defect concentration at higher annealing temperatures, most likely through known titanium interstitial and oxygen vacancy diffusion mechanisms. A potential follow up future experiment would be a comparable study on anatase, where defects are more likely to remain subsurface, which would be an intriguing comparison.

Chapter 4 demonstrates the interaction of water, oxygen and air molecules with the defects of the rutile $TiO_2(110)$ surfaces. Defective surfaces were prepared using $Ar^+$ sputtering before each exposure to investigate the effect of the corresponding exposed molecules. The intensity of the oxygen vacancy gradually decreased upon exposure to water, oxygen, air and ambient pressure. During water exposure defects heal by water dissociation whereas during oxygen exposure oxygen dissociates into an oxygen atom and an oxygen adatom, where the oxygen atom fills the vacancy and the oxygen adatom dissociates further water and produces two identical OH. Upon exposure to ambient pressure, further depletion of the defect was observed. A rapid depletion of the Ti intermediate oxidation state was observed during annealing as a function of increasing temperature in ambient pressure. This is more likely due to the progressive conversion of $Ti^{1+}$ defects to $Ti^{4+}$ via intermediate oxidation states by bulk assistance oxidation mechanism through titanium interstitial and oxygen vacancy diffusion mechanism.

In chapter 5, the chemisorbed bi-isonicotinic acid on rutile, anatase and mesoporous $TiO_2$ have been investigated using X-ray photoemission, resonant photoemission and X-ray absorption spectroscopy. XPS suggests the interaction between bi-isonicotinic acid and substrates through carboxylic acid groups. Where, carboxylic acid groups bonded to the rutile and anatase surfaces through bidentate bonding geometry but mesoporous substrate bonded

through a mixture of bidentate and monodentate bonding geometry. The N $1s$ XAS shows that the LUMO lies entirely within the band gap of rutile, anatase and mesoporous $TiO_2$ respectively. As a consequence, the electron transfer between LUMO and substrates is electronically forbidden. Whereas, LUMO+1 and LUMO+2 states of the core excited molecules overlap with the unoccupied states in the substrate. The depletion of intensity in the participator channel of the LUMO+1 and LUMO+2 states observed in RPES indicates the ultra fast charge transfer to the surface in the core-hole life time. We have estimated the timescale of the charge transfer dynamics by comparing the relative intensities of the participator channel to the XAS for both monolayer and multilayer. The estimated charge transfer time from the LUMO+2 state to the conduction band of the substrate for chemisorbed bi-isonicotinic acid on rutile, anatase and mesoporous titanium dioxide is $(3.2 \pm 0.2)$, $(3.4 \pm 0.2)$ and $(4.7 \pm 0.4)$ fs respectively.

In chapter 6, the monolayer and multilayer coverage of N3 dye complex on mesoporous $TiO_2$ have been investigated using X-ray absorption spectroscopy (XAS), resonant inelastic X-ray scattering (RIXS) and resonant photoemission spectroscopy (RPES). X-ray photoemission spectroscopy (XPS) spectra reveal the presence of the protonated carboxylic group, which might be evidence of the absorption of N3 on mesoporous substrate bonded through mixture of bidentate and monodentate bonding geometry. The features that we have seen in RIXS also present in RPES. These observed intense features and vibronic coupling mechanisms have been discussed thoroughly. The orbital contributions of the bi-isonicotinic acid and thiocyanate ligands were used to interpret the RIXS. A comparison with resonant photoemission spectroscopy (RPES) and density functional theory (DFT) calculations provides additional interpretation. Over all, these three complementary approaches have been combined to provide an understanding of the electronic structure of complex molecules. The aim in the near future would be the core-hole clock implementation to investigate the charge transfer time between N3 molecules and mesoporous

$TiO_2$. Perhaps we could use RIXS to probe the charge transfer interface that is buried in a real device because the X-rays can escape from deeper within the crystal. The efforts to correlate the charge transfer time from RIXS and RPES have failed, either because of something fundamental in the processes or because of signal strength and uncertainty in the results. But a potential follow-up investigation would be to attempt to probe the charge transfer time in solar cells like perovskites using RIXS and RPES.

# Bibliography


[1] J. Conti, P. Holtberg, J. Diefenderfer, A. LaRose, J. T. Turnure, and L. Westfall, "International energy outlook 2016 with projections to 2040," USDOE Energy Information Administration (EIA), Washington DC, United States , Tech. Rep., 2016.

[2] A. Mei, X. Li, L. Liu, Z. Ku, T. Liu, Y. Rong, M. Xu, M. Hu, J. Chen, Y. Yang *et al.*, "A hole-conductor–free, fully printable mesoscopic perovskite solar cell with high stability," *Science*, vol. 345, no. 6194, pp. 295–298, 2014.

[3] S. Mathew, A. Yella, P. Gao, R. Humphry-Baker, B. F. Curchod, N. Ashari-Astani, I. Tavernelli, U. Rothlisberger, M. Nazeeruddin, M. Grätzel *et al.*, "Dye-sensitized solar cells with 13% efficiency achieved through the molecular engineering of porphyrin sensitizers," *Nature chemistry*, vol. 6, no. 3, pp. 242–247, 2014.

[4] T. Hisatomi, J. Kubota, and K. Domen, "Recent advances in semiconductors for photocatalytic and photoelectrochemical water splitting," *Chemical society reviews*, vol. 43, no. 22, pp. 7520–7535, 2014.

[5] D. Bao, Q. Zhang, F.-L. Meng, H.-X. Zhong, M.-M. Shi, Y. Zhang, J.-M. Yan, Q. Jiang, and X.-B. Zhang, "Electrochemical reduction of $n_2$ under ambient conditions for artificial $n_2$ fixation and renewable energy storage using n2/nh3 cycle," *Advanced materials*, vol. 29, no. 3, p. 1604799, 2017.

[6] B. O'regan and M. Grätzel, "A low-cost, high-efficiency solar cell based on dye-sensitized colloidal $tio_2$ films," *Nature*, vol. 353, no. 6346, pp. 737–740, 1991.

[7] J. W. Ager, M. R. Shaner, K. A. Walczak, I. D. Sharp, and S. Ardo, "Experimental demonstrations of spontaneous, solar-driven photoelectrochemical water splitting," *Energy & environmental science*, vol. 8, no. 10, pp. 2811–2824, 2015.

[8] W. West, "First hundred years of spectral sensitization," *Photographic science and engineering*, vol. 18, no. 1, pp. 35–48, 1974.

[9] M. Grätzel, "Dye-sensitized solar cells," *Journal of photochemistry and photobiology C: photochemistry reviews*, vol. 4, no. 2, pp. 145–153, 2003.

[10] M. K. Nazeeruddin, A. Kay, I. Rodicio, R. Humphry-Baker, E. Müller, P. Liska, N. Vlachopoulos, and M. Grätzel, "Conversion of light to electricity by cis-x2bis (2, 2'-bipyridyl-4, 4'-dicarboxylate) ruthenium (ii)

charge-transfer sensitizers (x= cl-, br-, i-, cn-, and scn-) on nanocrystalline titanium dioxide electrodes," *Journal of the American chemical society*, vol. 115, no. 14, pp. 6382–6390, 1993.

[11] L. C. Mayor, J. Ben Taylor, G. Magnano, A. Rienzo, C. J. Satterley, J. N. O'Shea, and J. Schnadt, "Photoemission, resonant photoemission, and x-ray absorption of a ru (ii) complex adsorbed on rutile ti o 2 (110) prepared by in situ electrospray deposition," *The Journal of chemical physics*, vol. 129, no. 11, p. 114701, 2008.

[12] P. Persson, A. Stashans, R. Bergström, and S. Lunell, "Periodic indo calculations of organic adsorbates on a $tio_2$ surface," *International journal of quantum chemistry*, vol. 70, no. 4-5, pp. 1055–1066, 1998.

[13] P. Persson and S. Lunell, "Binding of bi-isonicotinic acid to anatase tio2 (1 0 1)," *Solar energy materials and solar cells*, vol. 63, no. 2, pp. 139–148, 2000.

[14] A. Thomas, W. Flavell, C. Chatwin, S. Rayner, D. Tsoutsou, A. Kumarasinghe, D. Brete, T. Johal, S. Patel, and J. Purton, "Adsorption of bi-isonicotinic acid on anatase $tio_2$ (1 0 1) and (0 0 1) studied by photoemission and nexafs spectroscopy," *Surface science*, vol. 592, no. 1-3, pp. 159–168, 2005.

[15] J. Schnadt, A. Henningsson, M. P. Andersson, P. G. Karlsson, P. Uvdal, H. Siegbahn, P. A. Brühwiler, and A. Sandell, "Adsorption and charge-transfer study of bi-isonicotinic acid on in situ-grown anatase $tio_2$ nanoparticles," *The Journal of physical chemistry B*, vol. 108, no. 10, pp. 3114–3122, 2004.

[16] L. C. Mayor, A. Saywell, G. Magnano, C. J. Satterley, J. Schnadt, and J. N. O'Shea, "Adsorption of a ru (ii) dye complex on the au (111) surface: Photoemission and scanning tunneling microscopy," *The Journal of chemical physics*, vol. 130, no. 16, p. 164704, 2009.

[17] A. J. Gibson, R. H. Temperton, K. Handrup, M. Weston, L. C. Mayor, and J. N. O'Shea, "Charge transfer from an adsorbed ruthenium-based photosensitizer through an ultra-thin aluminium oxide layer and into a metallic substrate," *The Journal of chemical physics*, vol. 140, no. 23, p. 234708, 2014.

[18] J. Schnadt, J. O'shea, L. Patthey, L. Kjeldgaard, J. Åhlund, K. Nilson, J. Schiessling, J. Krempaskỳ, M. Shi, O. Karis *et al.*, "Excited-state charge transfer dynamics in systems of aromatic adsorbates on $tio_2$ studied with resonant core techniques," *The Journal of chemical physics*, vol. 119, no. 23, pp. 12 462–12 472, 2003.

[19] J. N. O'Shea, K. Handrup, R. H. Temperton, A. J. Gibson, A. Nicolaou, N. Jaouen, J. B. Taylor, L. C. Mayor, J. C. Swarbrick, and J. Schnadt, "Ultra-fast intramolecular vibronic coupling revealed by rixs and rpes maps of an aromatic adsorbate on $tio_2$ (110)," *The Journal of chemical physics*, vol. 148, no. 20, p. 204705, 2018.

[20] J. N. O'Shea, K. Handrup, R. H. Temperton, A. J. Gibson, A. Nicolaou, and N. Jaouen, "Exploring ultra-fast charge transfer and vibronic coupling with n 1s rixs maps of an aromatic molecule coupled to a semiconductor," *The Journal of chemical physics*, vol. 147, no. 13, p. 134705, 2017.

[21] J. Schnadt, P. A. Brühwiler, L. Patthey, J. N. O'shea, S. Södergren, M. Odelius, R. Ahuja, O. Karis, M. Bässler, P. Persson *et al.*, "Experimental evidence for sub-3-fs charge transfer from an aromatic adsorbate to a semiconductor," *Nature*, vol. 418, no. 6898, pp. 620–623, 2002.

[22] M. Odelius, P. Persson, and S. Lunell, "Bi-isonicotinic acid on rutile (1 1 0): calculated molecular and electronic structure," *Surface science*, vol. 529, no. 1-2, pp. 47–58, 2003.

[23] A. J. Britton, M. Weston, and J. N. O'Shea, "Charge transfer from an aromatic adsorbate to a semiconductor $tio_2$ surface probed on the femtosecond time scale with resonant inelastic x-ray scattering," *Physical review letters*, vol. 109, no. 1, p. 017401, 2012.

[24] L. Patthey, H. Rensmo, P. Persson, K. Westermark, L. Vayssieres, A. Stashans, Å. Petersson, P. Brühwiler, H. Siegbahn, S. Lunell *et al.*, "Adsorption of bi-isonicotinic acid on rutile $tio_2$ (110)," *The Journal of chemical physics*, vol. 110, no. 12, pp. 5913–5918, 1999.

[25] P. Persson, S. Lunell, P. A. Brühwiler, J. Schnadt, S. Södergren, J. N. O'Shea, O. Karis, H. Siegbahn, N. Mårtensson, M. Bässler *et al.*, "N 1s x-ray absorption study of the bonding interaction of bi-isonicotinic acid adsorbed on rutile $tio_2$ (110)," *The Journal of chemical physics*, vol. 112, no. 9, pp. 3945–3948, 2000.

[26] J. N. O'Shea, J. B. Taylor, L. C. Mayor, J. C. Swarbrick, and J. Schnadt, "Molecular damage in bi-isonicotinic acid adsorbed on rutile $tio_2$ (1 1 0)," *Surface science*, vol. 602, no. 9, pp. 1693–1698, 2008.

[27] J. Schnadt, J. O'shea, L. Patthey, J. Schiessling, y. J. Krempaskỳ, M. Shi, N. Mårtensson, and P. Brühwiler, "Structural study of adsorption of isonicotinic acid and related molecules on rutile $TiO_2$(110) ii: XPS," *Surface science*, vol. 544, no. 1, pp. 74–86, 2003.

[28] J. B. Taylor, L. C. Mayor, J. C. Swarbrick, J. N. O'Shea, and J. Schnadt, "Charge-transfer dynamics at model metal- organic solar cell surfaces," *The Journal of physical chemistry C*, vol. 111, no. 44, pp. 16 646–16 655, 2007.

[29] J. O'Shea, Y. Luo, J. Schnadt, L. Patthey, H. Hillesheimer, J. Krempasky, D. Nordlund, M. Nagasono, P. Brühwiler, and N. Mårtensson, "Hydrogen-bond induced surface core-level shift in pyridine carboxylic acids," *Surface science*, vol. 486, no. 3, pp. 157–166, 2001.

[30] F. Labat and C. Adamo, "Bi-isonicotinic acid on anatase (101): insights from theory," *The Journal of physical chemistry C*, vol. 111, no. 41, pp. 15 034–15 042, 2007.

[31] R. H. Temperton, J. Hart, N. Verykokkos, E. Gibson, and J. N. O'Shea, "A soft x-ray probe of a titania photoelectrode sensitized with a triphenylamine dye," *The Journal of chemical physics*, vol. 154, no. 23, p. 234707, 2021.

[32] M. Weston, T. J. Reade, A. J. Britton, K. Handrup, N. R. Champness, and J. N. O'Shea, "A single centre water splitting dye complex adsorbed on rutile $TiO_2$(110): Photoemission, x-ray absorption, and optical spectroscopy," *The Journal of chemical physics*, vol. 135, no. 11, p. 114703, 2011.

[33] C. E. McCusker and F. N. Castellano, "Design of a long-lifetime, earth-abundant, aqueous compatible cu (i) photosensitizer using cooperative steric effects," *Inorganic chemistry*, vol. 52, no. 14, pp. 8114–8120, 2013.

[34] Y. Liu, P. Persson, V. Sundstrom, and K. Warnmark, "Fe n-heterocyclic carbene complexes as promising photosensitizers," *Accounts of chemical research*, vol. 49, no. 8, pp. 1477–1485, 2016.

[35] P. Chábera, Y. Liu, O. Prakash, E. Thyrhaug, A. E. Nahhas, A. Honarfar, S. Essén, L. A. Fredin, T. C. Harlang, K. S. Kjær *et al.*, "A low-spin fe (iii) complex with 100-ps ligand-to-metal charge transfer photoluminescence," *Nature*, vol. 543, no. 7647, pp. 695–699, 2017.

[36] K. Zweibel, "Terawatt challenge for thin-film pv," National Renewable Energy Lab.(NREL), Golden, CO (United States), Tech. Rep., 2005.

[37] P. Brühwiler, O. Karis, and N. Mårtensson, "Charge-transfer dynamics studied using resonant core spectroscopies," *Reviews of modern physics*, vol. 74, no. 3, p. 703, 2002.

[38] A. J. Britton, M. Weston, J. B. Taylor, A. Rienzo, L. C. Mayor, and J. N. O'Shea, "Charge transfer interactions of a ru (ii) dye complex and related ligand molecules adsorbed on au (111)," *The Journal of chemical physics*, vol. 135, no. 16, p. 164702, 2011.

[39] A. J. Gibson, R. H. Temperton, K. Handrup, and J. N. O'Shea, "Resonant core spectroscopies of the charge transfer interactions between c60 and the surfaces of au (111), ag (111), cu (111) and pt (111)," *Surface science*, vol. 657, pp. 69–78, 2017.

[40] U. Diebold, "The surface science of titanium dioxide," *Surface science reports*, vol. 48, no. 5-8, pp. 53–229, 2003.

[41] H. Huntington and G. Sullivan, "Interstitial diffusion mechanism in rutile," *Physical review letters*, vol. 14, no. 6, p. 177, 1965.

[42] M. A. Henderson, "A surface perspective on self-diffusion in rutile $TiO_2$," *Surface science*, vol. 419, no. 2-3, pp. 174–187, 1999.

[43] M. H. M. Ahmed, R. H. Temperton, and J. N. O'Shea, "An in situ exploration of subsurface defect migration to a liquid water-exposed rutile $tio_2$ (110) surface by xps," *Surface and interface analysis*, vol. 53, no. 12, pp. 1013–1019, 2021.

[44] A. Einstein, "On a heuristic point of view concerning the production and transformation of light," *Annalen der physik*, pp. 1–18, 1905.

[45] S. Kevan, "Design of a high-resolution angle-resolving electron energy analyzer," *Review of scientific instruments*, vol. 54, no. 11, pp. 1441–1445, 1983.

[46] M. Dogan, M. Ulu, G. Gennarakis, and T. Zouros, "Experimental energy resolution of a paracentric hemispherical deflector analyzer for different entry positions and bias," *Review of scientific instruments*, vol. 84, no. 4, p. 043105, 2013.

[47] F. Elder, A. Gurewitsch, R. Langmuir, and H. Pollock, "Radiation from electrons in a synchrotron," *Physical review*, vol. 71, no. 11, p. 829, 1947.

[48] R. H. Temperton, "Complex molecules on surfaces: in-situ electrospray deposition and photoelectron spectroscopy," Ph.D. dissertation, University of Nottingham, 2017.

[49] K.-J. Kim, "Characteristics of synchrotron radiation," in *AIP conference proceedings*, vol. 184, no. 1. American Institute of Physics, 1989, pp. 565–632.

[50] P. Guttmann and C. Bittencourt, "Overview of nanoscale nexafs performed with soft x-ray microscopes," *Beilstein journal of nanotechnology*, vol. 6, no. 1, pp. 595–604, 2015.

[51] M. P. Seah and W. Dench, "Quantitative electron spectroscopy of surfaces: A standard data base for electron inelastic mean free paths in solids," *Surface and interface analysis*, vol. 1, no. 1, pp. 2–11, 1979.

[52] J. N. O'Shea, "Photoelectron spectroscopy of alkali-doped ni(110)-o surfaces," Ph.D. dissertation, University of Cardiff, 1998.

[53] M. Ruiz-Osés, D. G. de Oteyza, I. Fernández-Torrente, N. Gonzalez-Lakunza, P. M. Schmidt-Weber, T. Kampen, K. Horn, A. Gourdon, A. Arnau, and J. E. Ortega, "Non-covalent interactions in supramolecular assemblies investigated with electron spectroscopies," *ChemPhysChem*, vol. 10, no. 6, pp. 896–900, 2009.

[54] D. A. Shirley, "High-resolution x-ray photoemission spectrum of the valence bands of gold," *Physical review B*, vol. 5, no. 12, p. 4709, 1972.

[55] S. Tougaard, "Quantitative analysis of the inelastic background in surface electron spectroscopy," *Surface and interface analysis*, vol. 11, no. 9, pp. 453–472, 1988.

[56] M. Schmid, H.-P. Steinrück, and J. M. Gottfried, "A new asymmetric pseudo-voigt function for more efficient fitting of xps lines," *Surface and interface analysis*, vol. 46, no. 8, pp. 505–511, 2014.

[57] J. M. Hollas, *Modern spectroscopy*. John Wiley & Sons, 2004.

[58] J. C. Riviere and S. Myhra, *Handbook of surface and interface analysis: methods for problem-solving*. CRC press, 2009.

[59] G. Henderson, D. Neuville, and R. Downs, *Spectroscopic methods in mineralogy and material sciences*. Walter de Gruyter GmbH & Co KG, 2014, vol. 78.

[60] L. Li, J. Yan, T. Wang, Z.-J. Zhao, J. Zhang, J. Gong, and N. Guan, "Sub-10 nm rutile titanium dioxide nanoparticles for efficient visible-light-driven photocatalytic hydrogen production," *Nature communications*, vol. 6, p. 5881, 2015.

[61] S. Wu, W. Wang, W. Tu, S. Yin, Y. Sheng, M. Y. Manuputty, M. Kraft, and R. Xu, "Premixed stagnation flame synthesized $TiO_2$ nanoparticles with mixed phases for efficient photocatalytic hydrogen generation," *ACS sustainable chemistry & engineering*, vol. 6, no. 11, pp. 14 470–14 479, 2018.

[62] A. B. Djurišić, Y. He, and A. M. Ng, "Visible-light photocatalysts: Prospects and challenges," *APL materials*, vol. 8, no. 3, p. 030903, 2020.

[63] H. Luo, Z. Zeng, G. Zeng, C. Zhang, R. Xiao, D. Huang, C. Lai, M. Cheng, W. Wang, W. Xiong *et al.*, "Recent progress on metal-organic frameworks based-and derived-photocatalysts for water splitting," *Chemical engineering journal*, vol. 383, p. 123196, 2020.

[64] S. Chen, D. Huang, P. Xu, W. Xue, L. Lei, M. Cheng, R. Wang, X. Liu, and R. Deng, "Semiconductor-based photocatalysts for photocatalytic and photoelectrochemical water splitting: will we stop with photocorrosion?" *Journal of materials chemistry A*, vol. 8, no. 5, pp. 2286–2322, 2020.

[65] C. Dai and B. Liu, "Conjugated polymers for visible-light-driven photocatalysis," *Energy & environmental science*, vol. 13, p. 24, 2020.

[66] J. Nowotny, T. Bak, M. Nowotny, and L. Sheppard, "Titanium dioxide for solar-hydrogen i. functional properties," *International journal of hydrogen energy*, vol. 32, no. 14, pp. 2609–2629, 2007.

[67] S. K. Loeb, P. J. Alvarez, J. A. Brame, E. L. Cates, W. Choi, J. Crittenden, D. D. Dionysiou, Q. Li, G. Li-Puma, X. Quan *et al.*, "The technology horizon for photocatalytic water treatment: sunrise or sunset?" *Environmental science & technology*, vol. 53, no. 6, pp. 2937–2947, 2019.

[68] S.-Y. Lee and S.-J. Park, "$TiO_2$ photocatalyst for water treatment applications," *Journal of industrial and engineering chemistry*, vol. 19, no. 6, pp. 1761–1769, 2013.

[69] A. Fujishima, T. N. Rao, and D. A. Tryk, "Titanium dioxide photocatalysis," *Journal of photochemistry and photobiology C: photochemistry reviews*, vol. 1, no. 1, pp. 1–21, 2000.

[70] S. G. Kumar and L. G. Devi, "Review on modified $TiO_2$ photocatalysis under uv/visible light: selected results and related mechanisms on interfacial charge carrier transfer dynamics," *The Journal of physical chemistry A*, vol. 115, no. 46, pp. 13 211–13 241, 2011.

[71] L. Ruan, X. Wang, T. Wang, Z. Ren, Y. Chen, R. Zhao, D. Zhou, G. Fu, S. Li, L. Gao *et al.*, "Surface defect-controlled growth and high photocatalytic $H_2$ production efficiency of anatase $TiO_2$ nanosheets," *ACS applied materials & interfaces*, vol. 11, no. 40, pp. 37 256–37 262, 2019.

[72] S. G. Kumar and K. K. Rao, "Comparison of modification strategies towards enhanced charge carrier separation and photocatalytic degradation activity of metal oxide semiconductors ($TiO_2$, $WO_3$ and ZnO)," *Applied surface science*, vol. 391, pp. 124–148, 2017.

[73] R. Li, Y. Weng, X. Zhou, X. Wang, Y. Mi, R. Chong, H. Han, and C. Li, "Achieving overall water splitting using titanium dioxide-based photocatalysts of different phases," *Energy and environmental science*, vol. 8, no. 8, pp. 2377–2382, 2015.

[74] S. Yamamoto, H. Bluhm, K. Andersson, G. Ketteler, H. Ogasawara, M. Salmeron, and A. Nilsson, "In situ x-ray photoelectron spectroscopy studies of water on metals and oxides at ambient conditions," *Journal of physics: condensed matter*, vol. 20, no. 18, p. 184025, 2008.

[75] C. E. Patrick and F. Giustino, "Structure of a water monolayer on the anatase $TiO_2(101)$ surface," *Physical review applied*, vol. 2, no. 1, p. 014001, 2014.

[76] C. W. Wang, S. Yang, W. Q. Fang, P. Liu, H. Zhao, and H. G. Yang, "Engineered hematite mesoporous single crystals drive drastic enhancement in solar water splitting," *Nano letters*, vol. 16, no. 1, pp. 427–433, 2016.

[77] S. Yu, B. Han, Y. Lou, G. Qian, and Z. Wang, "One-step fabrication of highly self-hydroxylated $TiO_2$ mesocrystals and photocatalytic behavior towards water splitting," *International journal of hydrogen energy*, 2020.

[78] G. Teobaldi, W. Hofer, O. Bikondoa, C. Pang, G. Cabailh, and G. Thornton, "Modelling stm images of $TiO_2(110)$ from first-principles: Defects, water adsorption and dissociation products," *Chemical physics letters*, vol. 437, no. 1-3, pp. 73–78, 2007.

[79] M. A. Henderson, "The interaction of water with solid surfaces: fundamental aspects revisited," *Surface science reports*, vol. 46, no. 1-8, pp. 1–308, 2002.

[80] U. Diebold, "Structure and properties of $TiO_2$ surfaces: a brief review," *Applied physics A*, vol. 76, no. 5, pp. 681–687, 2003.

[81] G. Ketteler, S. Yamamoto, H. Bluhm, K. Andersson, D. E. Starr, D. F. Ogletree, H. Ogasawara, A. Nilsson, and M. Salmeron, "The nature of water nucleation sites on $TiO_2$(110) surfaces revealed by ambient pressure x-ray photoelectron spectroscopy," *The Journal of physical chemistry C*, vol. 111, no. 23, pp. 8278–8282, 2007.

[82] J. Mayer, U. Diebold, T. Madey, and E. Garfunkel, "Titanium and reduced titania overlayers on titanium dioxide (110)," *Journal of electron spectroscopy and related phenomena*, vol. 73, no. 1, pp. 1–11, 1995.

[83] G. Serrano, B. Bonanni, M. Di Giovannantonio, T. Kosmala, M. Schmid, U. Diebold, A. Di Carlo, J. Cheng, J. VandeVondele, and K. Wandelt, "Molecular ordering at the interface between liquid water and rutile $TiO_2$(110)," *Advanced materials interfaces*, vol. 2, no. 17, p. 1500246, 2015.

[84] R. Schaub, P. Thostrup, N. Lopez, E. Lægsgaard, I. Stensgaard, J. K. Nørskov, and F. Besenbacher, "Oxygen vacancies as active sites for water dissociation on rutile $TiO_2$(110)," *Physical review letters*, vol. 87, no. 26, p. 266104, 2001.

[85] R. D. Shannon, "Phase transformation studies in $TiO_2$ supporting different defect mechanisms in vacuum-reduced and hydrogen-reduced rutile," *Journal of applied physics*, vol. 35, no. 11, pp. 3414–3416, 1964.

[86] A. Schaefer, V. Lanzilotto, U. B. Cappel, P. Uvdal, A. Borg, and A. Sandell, "Defect-induced water bilayer growth on anatase $TiO_2$(101)," *Langmuir*, vol. 34, no. 37, pp. 10 856–10 864, 2018.

[87] M. A. Henderson, "An hreels and tpd study of water on $TiO_2$(110): the extent of molecular versus dissociative adsorption," *Surface science*, vol. 355, no. 1-3, pp. 151–166, 1996.

[88] O. Bikondoa, C. L. Pang, R. Ithnin, C. A. Muryn, H. Onishi, and G. Thornton, "Direct visualization of defect-mediated dissociation of water on $TiO_2$(110)," *Nature materials*, vol. 5, no. 3, pp. 189–192, 2006.

[89] L.-M. Liu, C. Zhang, G. Thornton, and A. Michaelides, "Structure and dynamics of liquid water on rutile $TiO_2$(110)," *Physical review B*, vol. 82, no. 16, p. 161415, 2010.

[90] J.-M. Pan, B. Maschhoff, U. Diebold, and T. Madey, "Interaction of water, oxygen, and hydrogen with $TiO_2$(110) surfaces having different defect densities," *Journal of vacuum science & technology A: vacuum, surfaces, and films*, vol. 10, no. 4, pp. 2470–2476, 1992.

[91] Y. Li and Y. Gao, "Interplay between water and $TiO_2$ anatase (101) surface with subsurface oxygen vacancy," *Physical review letters*, vol. 112, no. 20, p. 206101, 2014.

[92] M. J. Jackman, A. G. Thomas, and C. Muryn, "Photoelectron spectroscopy study of stoichiometric and reduced anatase $TiO_2$(101) surfaces:

the effect of subsurface defects on water adsorption at near-ambient pressures," *The Journal of physical chemistry C*, vol. 119, no. 24, pp. 13 682–13 690, 2015.

[93] H. Li, Y. Guo, and J. Robertson, "Calculation of $TiO_2$ surface and subsurface oxygen vacancy by the screened exchange functional," *The Journal of physical chemistry C*, vol. 119, no. 32, pp. 18 160–18 166, 2015.

[94] I. Brookes, C. Muryn, and G. Thornton, "Imaging water dissociation on $TiO_2$(110)," *Physical review letters*, vol. 87, no. 26, p. 266103, 2001.

[95] H. Cheng and A. Selloni, "Surface and subsurface oxygen vacancies in anatase $TiO_2$ and differences with rutile," *Physical review B*, vol. 79, no. 9, p. 092101, 2009.

[96] J. Knudsen, J. N. Andersen, and J. Schnadt, "A versatile instrument for ambient pressure x-ray photoelectron spectroscopy: The lund cell approach," *Surface science*, vol. 646, pp. 160–169, 2016.

[97] C. E. McCusker and F. N. Castellano, "Design of a long-lifetime, earth-abundant, aqueous compatible Cu (i) photosensitizer using cooperative steric effects," *Inorganic chemistry*, vol. 52, no. 14, pp. 8114–8120, 2013.

[98] S. Hashimoto and A. Tanaka, "Alteration of Ti 2p xps spectrum for titanium oxide by low-energy ar ion bombardment," *Surface and interface analysis: an international journal devoted to the development and application of techniques for the analysis of surfaces, interfaces and thin films*, vol. 34, no. 1, pp. 262–265, 2002.

[99] C. S. Fadley, "Angle-resolved x-ray photoelectron spectroscopy," *Progress in surface science*, vol. 16, no. 3, pp. 275–388, 1984.

[100] M. P. Seah and W. Dench, "Quantitative electron spectroscopy of surfaces: A standard data base for electron inelastic mean free paths in solids," *Surface and interface analysis*, vol. 1, no. 1, pp. 2–11, 1979.

[101] L.-Q. Wang, D. R. Baer, M. H. Engelhard, and A. N. Shultz, "The adsorption of liquid and vapor water on $TiO_2$(110) surfaces: the role of defects," *Surface science*, vol. 344, no. 3, pp. 237–250, 1995.

[102] R. H. Temperton, A. Gibson, and J. N. O'Shea, "In situ xps analysis of the atomic layer deposition of aluminium oxide on titanium dioxide," *Physical chemistry chemical physics*, vol. 21, no. 3, pp. 1393–1398, 2019.

[103] H. Hussain, G. Tocci, T. Woolcot, X. Torrelles, C. Pang, D. Humphrey, C. Yim, D. Grinter, G. Cabailh, O. Bikondoa *et al.*, "Structure of a model $TiO_2$ photocatalytic interface," *Nature materials*, vol. 16, no. 4, pp. 461–466, 2017.

[104] A. Fujishima and K. Honda, "Electrochemical photolysis of water at a semiconductor electrode," *Nature*, vol. 238, no. 5358, pp. 37–38, 1972.

[105] A. L. Linsebigler, G. Lu, and J. T. Yates Jr, "Photocatalysis on $tio_2$ surfaces: principles, mechanisms, and selected results," *Chemical reviews*, vol. 95, no. 3, pp. 735–758, 1995.

[106] T. Nonami, H. Hase, and K. Funakoshi, "Apatite-coated titanium dioxide photocatalyst for air purification," *Catalysis today*, vol. 96, no. 3, pp. 113–118, 2004.

[107] D. Kanakaraju, B. D. Glass, and M. Oelgemöller, "Titanium dioxide photocatalysis for pharmaceutical wastewater treatment," *Environmental chemistry letters*, vol. 12, no. 1, pp. 27–47, 2014.

[108] R. Ratshiedana, A. T. Kuvarega, and A. K. Mishra, "Titanium dioxide and graphitic carbon nitride–based nanocomposites and nanofibres for the degradation of organic pollutants in water: a review," *Environmental science and pollution research*, vol. 28, no. 9, pp. 10 357–10 374, 2021.

[109] H. Park, H.-i. Kim, G.-h. Moon, and W. Choi, "Photoinduced charge transfer processes in solar photocatalysis based on modified $tio_2$," *Energy & environmental science*, vol. 9, no. 2, pp. 411–433, 2016.

[110] F. Ning, M. Shao, S. Xu, Y. Fu, R. Zhang, M. Wei, D. G. Evans, and X. Duan, "$Tio_2$/graphene/nife-layered double hydroxide nanorod array photoanodes for efficient photoelectrochemical water splitting," *Energy & environmental science*, vol. 9, no. 8, pp. 2633–2643, 2016.

[111] R. Tang, R. Yin, S. Zhou, T. Ge, Z. Yuan, L. Zhang, and L. Yin, "Layered mos 2 coupled mofs-derived dual-phase $tio_2$ for enhanced photoelectrochemical performance," *Journal of materials chemistry A*, vol. 5, no. 10, pp. 4962–4971, 2017.

[112] Q. Peng, B. Kalanyan, P. G. Hoertz, A. Miller, D. H. Kim, K. Hanson, L. Alibabaei, J. Liu, T. J. Meyer, G. N. Parsons *et al.*, "Solution-processed, antimony-doped tin oxide colloid films enable high-performance $tio_2$ photoanodes for water splitting," *Nano letters*, vol. 13, no. 4, pp. 1481–1488, 2013.

[113] M. Takeuchi, H. Yamashita, M. Matsuoka, M. Anpo, T. Hirao, N. Itoh, and N. Iwamoto, "Photocatalytic decomposition of no under visible light irradiation on the cr-ion-implanted $tio_2$ thin film photocatalyst," *Catalysis letters*, vol. 67, no. 2, pp. 135–137, 2000.

[114] V. E. Henrich and P. A. Cox, *The surface science of metal oxides*. Cambridge university press, 1996.

[115] L.-B. Xiong, J.-L. Li, B. Yang, and Y. Yu, "$Ti^{3+}$ in the surface of titanium dioxide: Generation, properties and photocatalytic application," *Journal of nanomaterials*, vol. 2012, 2012.

[116] P. Thiel and T. Madey, "Surf. & interface anal," *Rep*, vol. 7, p. 211, 1987.

[117] W. S. Epling, C. H. Peden, M. A. Henderson, and U. Diebold, "Evidence for oxygen adatoms on tio$_2$ (110) resulting from o$_2$ dissociation at vacancy sites," *Surface science*, vol. 412, pp. 333–343, 1998.

[118] M. Weston, T. J. Reade, K. Handrup, N. R. Champness, and J. N. O'Shea, "Adsorption of dipyrrin-based dye complexes on a rutile tio$_2$ (110) surface," *The Journal of physical chemistry C*, vol. 116, no. 34, pp. 18 184–18 192, 2012.

[119] M. Weston, K. Handrup, T. J. Reade, N. R. Champness, and J. N. O'Shea, "Experimental observation of sub-femtosecond charge transfer in a model water splitting dye-sensitized solar cell," *The Journal of chemical physics*, vol. 137, no. 22, p. 224706, 2012.

[120] M. Weston, A. J. Britton, and J. N. O'Shea, "Charge transfer dynamics of model charge transfer centers of a multicenter water splitting dye complex on rutile tio$_2$ (110)," *The Journal of chemical physics*, vol. 134, no. 5, p. 054705, 2011.

[121] R. H. Temperton, A. J. Gibson, K. Handrup, and J. N. O'Shea, "Adsorption and charge transfer interactions of bi-isonicotinic acid on ag (111)," *The Journal of chemical physics*, vol. 147, no. 5, p. 054703, 2017.

[122] D. O. Scanlon, C. W. Dunnill, J. Buckeridge, S. A. Shevlin, A. J. Logsdail, S. M. Woodley, C. R. A. Catlow, M. Powell, R. G. Palgrave, I. P. Parkin *et al.*, "Band alignment of rutile and anatase tio$_2$," *Nature materials*, vol. 12, no. 9, pp. 798–801, 2013.

[123] M. Grätzel, "Conversion of sunlight to electric power by nanocrystalline dye-sensitized solar cells," *Journal of photochemistry and photobiology A: chemistry*, vol. 164, no. 1-3, pp. 3–14, 2004.

[124] M. Grätzel, "Photoelectrochemical cells," *Nature*, vol. 414, no. 6861, pp. 338–344, 2001.

[125] R. H. Temperton, S. T. Skowron, K. Handrup, A. J. Gibson, A. Nicolaou, N. Jaouen, E. Besley, and J. N. O'Shea, "Resonant inelastic x-ray scattering of a ru photosensitizer: Insights from individual ligands to the electronic structure of the complete molecule," *The Journal of chemical physics*, vol. 151, no. 7, p. 074701, 2019.

[126] H. Rensmo, S. Södergren, L. Patthey, K. Westermark, L. Vayssieres, O. Kohle, P. Brühwiler, A. Hagfeldt, and H. Siegbahn, "The electronic structure of the cis-bis (4, 4-dicarboxy-2, 2-bipyridine)-bis (isothiocyanato) ruthenium (ii) complex and its ligand 2, 2-bipyridyl-4, 4-dicarboxylic acid studied with electron spectroscopy," *Chemical physics letters*, vol. 274, no. 1-3, pp. 51–57, 1997.

[127] E. M. Johansson, M. Hedlund, H. Siegbahn, and H. Rensmo, "Electronic and molecular surface structure of ru (tcterpy)(ncs) 3 and ru (dcbpy) 2 (ncs) 2 adsorbed from solution onto nanostructured tio2: a photoelectron spectroscopy study," *The Journal of physical chemistry B*, vol. 109, no. 47, pp. 22 256–22 263, 2005.

[128] C. E. Patrick and F. Giustino, "O 1 s core-level shifts at the anatase tio$_2$ (101)/n3 photovoltaic interface: Signature of h-bonded supramolecular assembly," *Physical review B*, vol. 84, no. 8, p. 085330, 2011.

[129] J. C. Fuggle and N. Mårtensson, "Core-level binding energies in metals," *Journal of electron spectroscopy and related phenomena*, vol. 21, no. 3, pp. 275–281, 1980.

[130] J. Schnadt, J. O'Shea, L. Patthey, J. Krempaskỳ, N. Mårtensson, and P. Brühwiler, "Alignment of valence photoemission, x-ray absorption, and substrate density of states for an adsorbate on a semiconductor surface," *Physical review B*, vol. 67, no. 23, p. 235420, 2003.

[131] J. E. Monat, J. H. Rodriguez, and J. K. McCusker, "Ground-and excited-state electronic structures of the solar cell sensitizer bis (4, 4 '-dicarboxylato-2, 2 '-bipyridine) bis (isothiocyanato) ruthenium (ii)," *The Journal of physical chemistry A*, vol. 106, no. 32, pp. 7399–7406, 2002.

# Appendix A

# List of Abbreviations

| | |
|---|---|
| UHV | Ultra-High Vacuum |
| KE | Kinetic Energy |
| BE | Binding Energy |
| DSSC | Dye Sensitised Solar Cell |
| HOMO | Highest Occupied Molecular Orbital |
| LUMO | Lowest Unoccupied Molecular Orbital |
| K-cell | Knudsen-cell |
| MCP | Microchannel plate |
| NEXAFS | Near Edge X-ray Absorption Spectroscopy |
| XPS | X-ray Photoelectron Spectroscopy |
| RPES | Resonant Photoelectron Spectroscopy |
| RIXS | Resonant inelastic X-ray scattering |
| XAS | X-ray Absorption Spectroscopy |